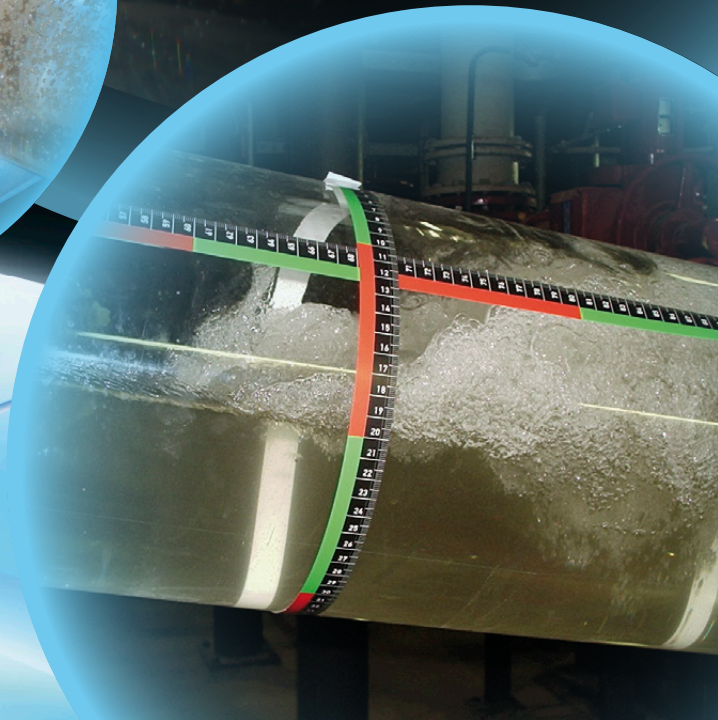
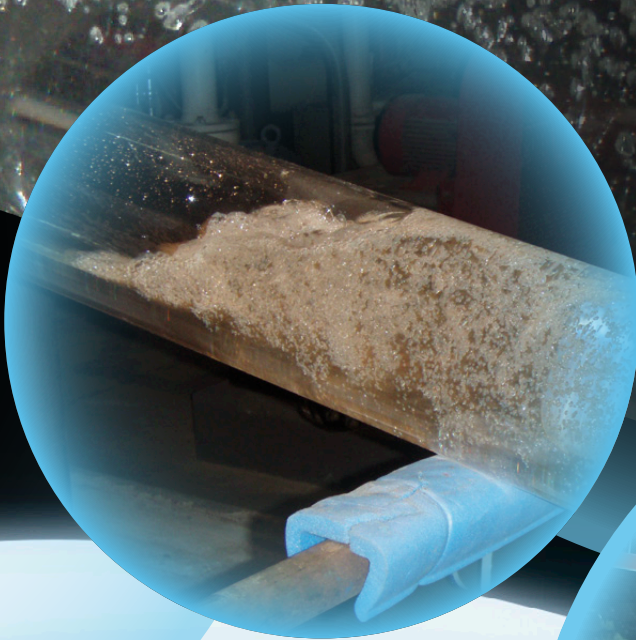




Ivo Pothof

Co-current  
**air-water flow**  
in downward  
sloping pipes



# Co-current air-water flow in downward sloping pipes

## Transport of capacity reducing gas pockets in wastewater mains

Proefschrift

ter verkrijging van de graad van doctor  
aan de Technische Universiteit Delft,  
op gezag van de Rector Magnificus prof. ir. K.C.A.M. Luyben,  
voorzitter van het College voor Promoties,  
in het openbaar te verdedigen op

vrijdag 4 februari 2011 om 12.30 uur

door  
Ignatius Wilhelmus Maria POTHOF

ingenieur toegepaste wiskunde  
geboren te Rhenen

Dit proefschrift is goedgekeurd door de promotor:

Prof. dr. ir. F.H.L.R. Clemens

Samenstelling promotiecommissie:

Rector Magnificus,	voorzitter
Prof. dr. ir. F.H.L.R. Clemens,	Technische Universiteit Delft, promotor
Prof. dr. ir. W.S.J. Uijttewaal,	Technische Universiteit Delft
Prof. dr. R.F. Mudde,	Technische Universiteit Delft
Prof. dr. W.H. Hager,	ETH Zürich, Zwitserland
Prof. P. Andreussi,	Università di Pisa, Italië
Prof. dr. ir. J. E. Berlamont,	Katholieke Universiteit Leuven, België
Prof. dr. B. W. Karney,	University of Toronto, Canada
Prof. ir. J.H.J.M. van der Graaf,	Technische Universiteit Delft, reservelid

This thesis is part of the CAPWAT joint industry project on capacity reduction in pressurized wastewater mains. The CAPWAT project was funded by Deltares, Delft University of Technology, water boards Delfland, Hollands Noorderkwartier, Brabantse Delta, Reest en Wieden, Rivierenland, Zuiderzeeland, Fryslân and Hollandse Delta, water companies Aquafin and Waternet, consultants Royal Haskoning, Grontmij Engineering Consultancy, Gemeentewerken Rotterdam, ITT Water & Wastewater, R&D foundations STOWA and RIONED and the Dutch Ministry of Economic Affairs.

Author	I.W.M. Pothof
Printed by	Gildeprint Drukkerijen BV, Enschede
Cover by	Martin van Schie, Deltares, Delft
Cover photos by	Christof Lubbers, Michiel Tukker, Ivo Pothof
ISBN	978-90-8957-018-5

Copyright © 2011 by I.W.M. Pothof

---

# Contents

<b>Summary</b> .....	<b>i</b>
<b>Samenvatting</b> .....	<b>v</b>
<b>List of Symbols</b> .....	<b>ix</b>
<b>1 Introduction</b> .....	<b>1</b>
1.1 Air-water flow in pipes .....	1
1.2 Context.....	2
1.3 Structure of thesis .....	5
<b>2 Literature review</b> .....	<b>7</b>
2.1 Gas pockets in wastewater mains .....	7
2.2 Air-water flow in downward sloping pipes .....	9
2.2.1 Discussion .....	17
2.3 Air transport by hydraulic jumps.....	20
2.3.1 Discussion on air transport by hydraulic jumps .....	22
2.4 Air transport by surface entrainment.....	24
2.4.1 Discussion on air transport by surface aeration.....	25
2.5 Air transport by dissolving into the water phase.....	26
2.6 Research questions.....	27
<b>3 Experiments</b> .....	<b>29</b>
3.1 Dimensional analysis .....	29
3.2 Experimental facilities and instrumentation .....	31
3.3 Test procedure .....	35
3.4 Uncertainty of results.....	38
3.5 Experimental results .....	42
3.5.1 Observed flow regimes and gas pocket head loss .....	42
3.5.2 Maximum air transport without air pocket accumulation .....	46
3.5.3 Influence of pipe diameter and sloping reach length .....	48
3.5.4 Influence of surface tension.....	49
3.5.5 Influence of absolute pressure.....	51
3.5.6 Influence of wastewater.....	51
3.6 Limitations of air transport models.....	54

---

<b>4</b>	<b>Theoretical considerations .....</b>	<b>57</b>
4.1	Introduction.....	57
4.2	Surface tension influence on clearing velocity.....	57
4.3	Flow regime transition 2a to 2b.....	58
4.4	Flow regime transition 2b to 3.....	60
4.5	Conclusions.....	64
<b>5</b>	<b>Air transport model .....</b>	<b>65</b>
5.1	Introduction.....	65
5.2	Air transport model in plug flow regime.....	66
5.3	Air transport model in blow-back flow regime.....	68
5.4	Air transport at $Eo < 5000$ .....	71
5.5	Discussion.....	74
5.6	Conclusions & recommendations.....	75
<b>6</b>	<b>Detection of gas pockets .....</b>	<b>77</b>
6.1	Introduction.....	77
6.2	Literature overview.....	77
6.3	Gas pocket detection by frequency analysis.....	78
6.4	Gas pocket volume and frequency drop.....	80
6.5	Extended detection method.....	84
	6.5.1 Detection procedure.....	84
	6.5.2 Parameters for gas pocket volume estimate.....	86
6.6	Feasibility of the extended detection method.....	87
	6.6.1 Reference transients and gas pocket transients.....	88
	6.6.2 Gas pocket transients.....	90
	6.6.3 Gas pocket predictions.....	91
6.7	Field measurement.....	93
	6.7.1 System description.....	93
	6.7.2 Preparations for transient measurements.....	96
	6.7.3 Data acquisition.....	96
	6.7.4 Analysis of transient pressure measurements.....	97
6.8	Conclusions and recommendations.....	99
	6.8.1 Recommendations.....	101
<b>7</b>	<b>Practical applications.....</b>	<b>103</b>
7.1	Priming of a gravity-driven transportation pipeline.....	103
7.2	Pipeline redesign – railroad inverted siphon.....	106
7.3	Conclusions.....	111

---

<b>8 Conclusions and recommendations.....</b>	<b>113</b>
8.1 Conclusions.....	113
8.2 Recommendations for practical applications.....	117
8.3 Recommendations for future research.....	118

<b>References .....</b>	<b>121</b>
-------------------------	------------

## **Appendices**

<b>A Free surface flows in downward sloping circular pipes.....</b>	<b>127</b>
A.1 Geometric relations.....	127
A.2 Free surface flow at normal depth .....	128

<b>B Experimental results.....</b>	<b>131</b>
------------------------------------	------------

<b>Dankwoord .....</b>	<b>139</b>
------------------------	------------

<b>Curriculum Vitae .....</b>	<b>141</b>
-------------------------------	------------



---

## Summary

Air-water flow is an undesired condition in many systems for the transportation of water or wastewater. Air in storm water tunnels may get trapped and negatively affect the system. Air pockets in hydropower tunnels or sewers may cause blow-back events and inadmissible pressure spikes. Water pipes and wastewater pressure mains in particular are subject to air pocket formation in downward-sloping reaches, such as inverted siphons or terrain slopes. Air pocket accumulation causes energy losses and an associated capacity reduction. Whereas in horizontal and in upward inclined pipes all entrained air is transported with the water flow, the air in downward sloping pipes can move in both directions. Knowledge on air pocket motion in downward sloping pipes is essential for the proper venting of pressurized pipes and for the prevention of severe blow-back events.

The motion of air pockets in downward sloping pipes, is closely related to liquid slugs in inclined pipes carrying gas with a small fraction of liquids (i.e. water, oil and gas condensate). The bubble-shaped interface and gas entrainment at the slug front are two features that are similar with air pockets in downward sloping pipes. Existing two-phase flow models have been validated mainly on data in horizontal and vertical pipes in which the gas phase drives the liquid phase. The performance of these models in inclined pipes, in which the liquid phase drives the gas phase, is not yet known.

Despite its practical relevance in a variety of engineering fields, the literature on air-water flows in downward sloping pipes is scarce. The fundamental momentum balance that predicts when an elongated air pocket becomes stagnant in a downward inclined pipe, is yet to be developed. Lubbers was the first to systematically investigate the co-current flow of air and water in downward sloping pipes over the complete range of possible air accumulations. Like this thesis, Lubbers' experimental research was part of the CAPWAT project on capacity losses in pressurised wastewater mains.

The main research question, addressed in this thesis, is the development and validation of a total air transport model by flowing water, including the influence of pipe angle, length of sloping section, pipe diameter, surface tension, absolute pressure, pipe friction factor and viscosity. Furthermore, the air discharge by flowing water and the gas pocket head loss in wastewater will be compared with those in clean water; a definition sketch of the gas pocket head loss is included in Figure S 1.



In order to quantify scale effects new measurements have been performed in laboratory facilities with internal pipe diameters of 0.08 m and 0.15 m and in a large-scale facility at a wastewater treatment plant with internal pipe diameter  $D = 0.192$  m, a downward sloping length of  $L = 40$  m ( $L/D = 209$ ) and a downward pipe angle of  $\theta = 10^\circ$ .

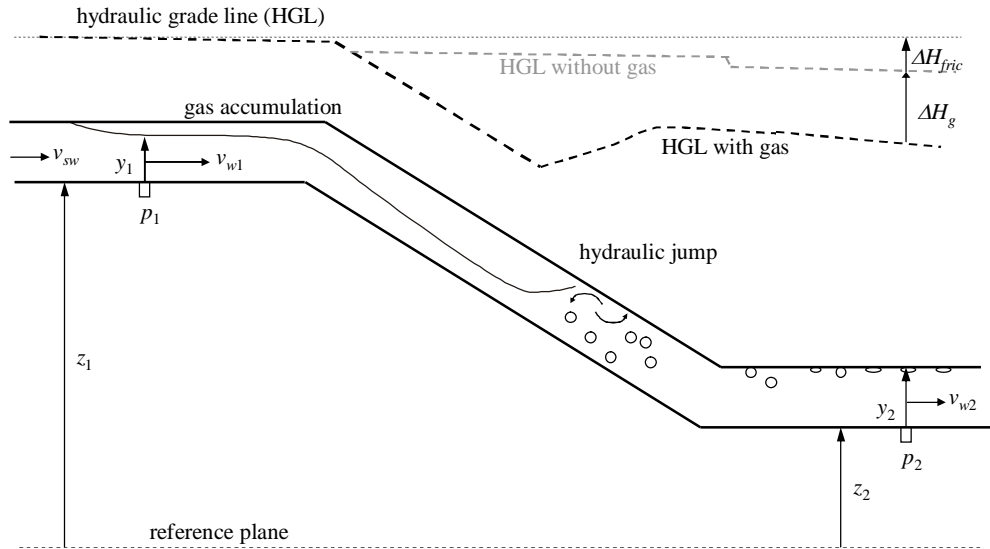


Figure S 1: Definition sketch for gas pocket head loss measurements in experimental facilities

Three series of experiments on co-current air-water flow have been conducted in this facility, each with its own specific objective in addition to the purpose of model validation:

- 1 Experiments with clean water, which provided quantitative information on the influence of the length of the downward sloping reach on the air pocket head loss and net air discharge.
- 2 Experiments with surfactant-added water for the assessment of the influence of surface tension on the air pocket head loss and net air discharge.
- 3 Experiments with untreated wastewater in order to determine the air pocket head loss and net air discharge in pipelines carrying wastewater. Obviously, these results have been compared with the first experimental series on clean water.

The following main conclusions are drawn from this thesis:

- 1 A physically-based predictive model has been developed for the net air discharge by flowing water in downward sloping pipes. The model parameters include the length of the downward sloping reach and total length of the air pockets, pipe angle, pipe

- 
- diameter, water (or liquid) discharge, viscosity, surface tension and pipe friction factor.
- 2 The model has been calibrated to a unique dataset of co-current air-water flows in downward sloping pipes.
  - 3 The composition of wastewater, i.e. lower surface tension and solids content, does not enhance the air transport in comparison with the air transport in clean water.
  - 4 A new velocity criterion for the occurrence of multiple air pockets in a downward sloping reach has been developed (Figure S 2). This criterion defines whether the maximum gas pocket head loss may occur in practice.
  - 5 A new momentum balance for elongated air pockets in downward sloping pipes has been developed. This momentum balance defines the clearing flow number as illustrated in Figure S 2. It is useful in practice to predict the direction and velocity of an elongated air pocket in a downward sloping pipe. The momentum balance and velocity criterion support the design of storm water storage tunnels and bottom outlets of hydropower stations for the proper venting of pipes and tunnels and for the prevention of severe blow-back events. Furthermore, two-phase flow models for the prediction of the transition to slug flow and its properties may benefit from these developments.
  - 6 The required water velocity to start the transport of an elongated gas pocket to the bottom of a downward sloping pipe reach is  $v_{sw} = 0.9 \cdot (gD)^{1/2}$  (or  $F_w = 0.9$ ) over a wide range of pipe angles ( $5^\circ - 20^\circ$ ). This statement has been substantiated with experimental data at  $D > 0.19$  m and the derived momentum balance.
  - 7 A gas pocket detection method for the prediction of a gas pocket location has been extended with a total gas volume prediction. The detection method has been tested successfully in a field experiment.

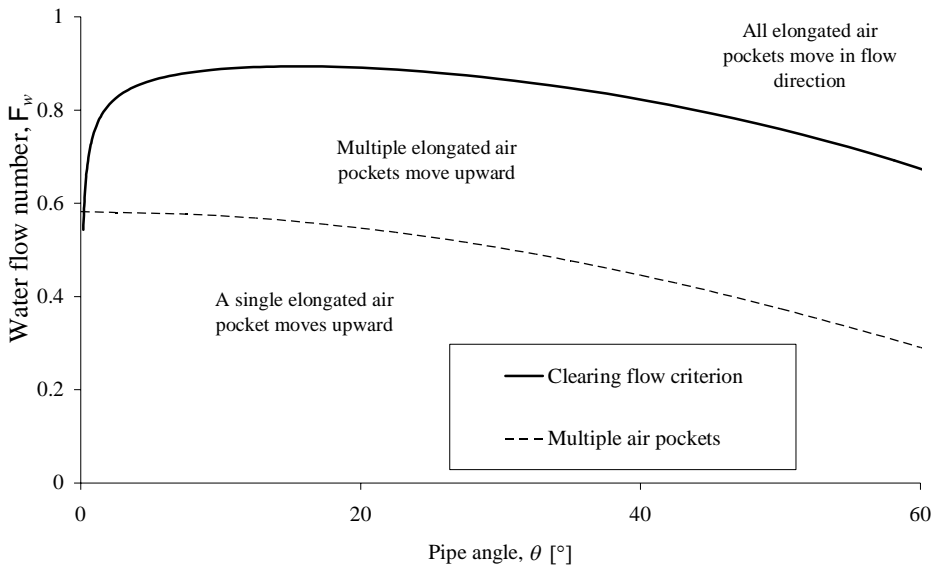


Figure S 2: Overview of criteria and elongated air pocket motion in downward sloping pipes

The CAPWAT research project (2004 – 2010) has led to a much better understanding of the accumulation, breakdown and transport of gas pockets in downward sloping sections of pipelines. The research project has led to many practical recommendations for the hydraulic design, commissioning, safe operation and maintenance of pressurised wastewater mains, which are available in an electronic handbook (Deltares, 2010).

---

## Samenvatting

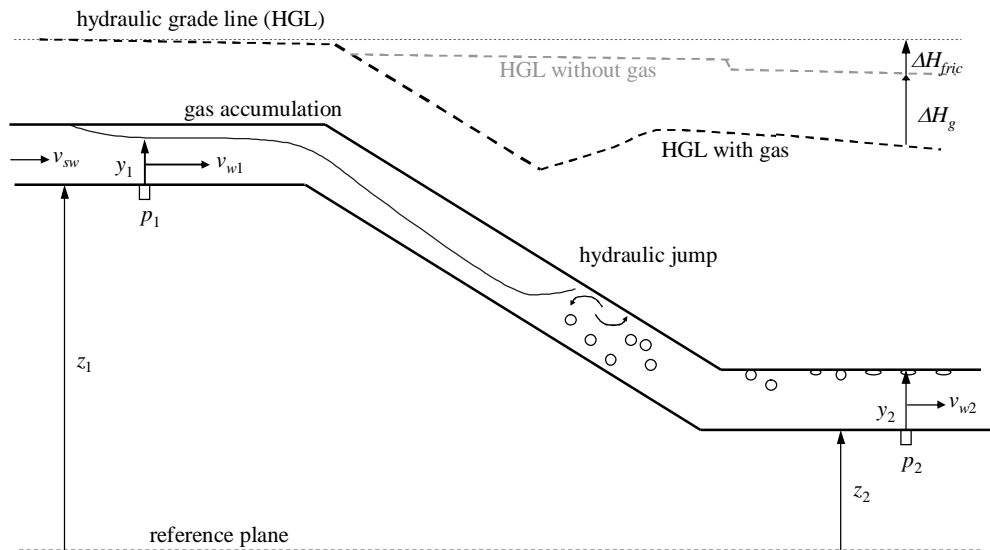
Water-luchtstroming is een ongewenst verschijnsel in persleidingen voor water- en afvalwatertransport. Lucht in regenwateropslagtunnels kan ingesloten raken en het systeemgedrag negatief beïnvloeden. Luchtbellen in riolen of in het leidingwerk van waterkrachtcentrales kunnen leiden tot ongecontroleerde ontluchting en ontoelaatbare drukstoten. Waterleidingen en afvalwaterleidingen zijn gevoelig voor luchtophoppingen in neergaande leidingdelen, zoals die voorkomen in zinkers en glooiend terrein. Luchtophoppingen veroorzaken energieverliezen en bijbehorende capaciteitsverliezen. In horizontale of opgaande leidingen stroomt de lucht altijd in dezelfde richting als het water, maar in neergaande leidingen kan de lucht in beide richtingen stromen. Kennis over de beweging van luchtbellen in neergaande leidingen is essentieel voor een goede ontluchting van persleidingen en ter voorkoming van incidenten.

Het gedrag van luchtbellen in neergaande leidingen is nauw verwant met het gedrag van vloeistofslugs in opgaande gas-condensaatleidingen met een kleine vloeistoffractie. De belvormige waterspiegel en de luchtinslag aan de voorkant van de slug zijn twee eigenschappen die een sterke analogie hebben met luchtbellen in neergaande leidingen. Bestaande twee-fasen-modellen zijn hoofdzakelijk gevalideerd met data uit horizontale en verticale leidingen, waarbij vloeistofslugs door de gasfase getransporteerd worden. De geschiktheid van dergelijke modellen in hellende leidingen, waarbij het gas door de vloeistof getransporteerd wordt, is onbekend.

Ondanks de praktische relevantie in meerdere vakgebieden is de bestaande literatuur over water-luchtstroming in neergaande leidingen zeer beperkt. De fundamentele krachtenbalans, die voorspelt wanneer een lange luchtbel blijft hangen, moet nog ontwikkeld worden. Lubbers heeft als eerste een systematisch onderzoek gedaan naar het luchttransport in neergaande leidingen over het complete bereik van luchtbellengtes. Zijn onderzoek was een onderdeel van het CAPWAT-project over capaciteitsverliezen in afvalwaterpersleidingen; dit proefschrift is ook een onderdeel van dat project.

De belangrijkste onderzoeksvraag, die in dit proefschrift besproken wordt, is de ontwikkeling en validatie van een rekenmodel voor het totale luchtdebiet door stromend water, waarbij de volgende factoren in rekening worden gebracht: hellingshoek van de leiding, lengte van het neergaande been, diameter, oppervlaktespanning, absolute druk, wrijvingsfactor en de viscositeit. Hiernaast worden het luchtdebiet en energieverlies in afvalwater vergeleken met die in schoon water; zie hiervoor Figuur S 1.

Er zijn metingen uitgevoerd in twee nieuwe lab-opstellingen en in een grootschalige opstelling op RWZI Nieuwe Waterweg in Hoek van Holland. De metingen in de lab-opstellingen met inwendige diameters van 0.08 m en 0.15 m zijn gebruikt om schaal-effecten te kwantificeren.



Figuur S 1: Definitieschets voor metingen luchtbeltransport

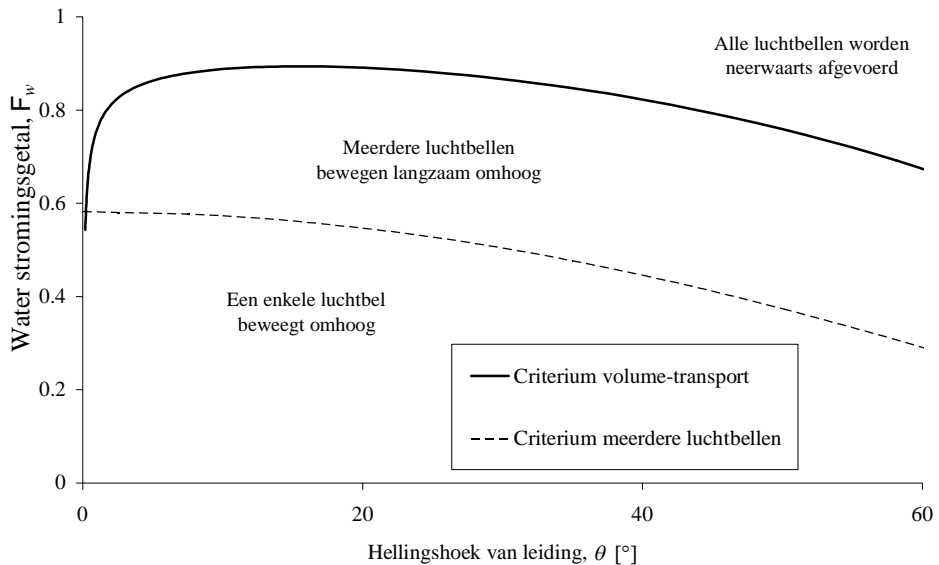
In de opstelling op de zuivering, met een lengte van 40 m, diameter van 0.192 m en hellingshoek van  $10^\circ$ , zijn drie meetseries uitgevoerd, elk met een specifieke doelstelling:

- 1 Metingen met schoon water, waarmee de invloed van de lengte van het dalende been op het luchtdebiet en energieverlies gekwantificeerd is
- 2 Metingen met water met detergents om de invloed van de oppervlaktespanning te onderzoeken
- 3 Metingen met ruw afvalwater om het luchtdebiet en energieverlies in afvalwaterleidingen te bepalen. Uiteraard zijn deze meetresultaten vergeleken met de overige metingen.

---

De onderstaande conclusies volgen uit dit onderzoek:

- 1 Een op behoudswetten gebaseerd rekenmodel is ontwikkeld voor het luchttransport in neergaande leidingen door stromend water. De modelparameters zijn de neergaande leidinglengte, de totale luchtbellengte, hellingshoek, leidingdiameter, waterdebiet, viscositeit, oppervlaktespanning en de wrijvingsfactor.
- 2 Het model is gecalibreerd met de omvangrijke en unieke verzameling van meetdata van water-lucht-stroming in neergaande leidingen.
- 3 De samenstelling van het afvalwater, met name de lagere oppervlaktespanning en het vaste stof gehalte, hebben geen gunstig effect op het luchttransport in vergelijking met het luchttransport in schoon water.
- 4 Een nieuw snelheids criterium voor de aanwezigheid van meerdere luchtbelllen is ontwikkeld (Figuur S 2). Dit criterium bepaalt in de praktijk wanneer het maximale energieverlies nog kan optreden.
- 5 Een nieuwe krachtenbalans is ontwikkeld voor de beweging van lange luchtbelllen in neergaande leidingen. Deze krachtenbalans bepaalt het kritieke stromingsgetal, waarbij lange luchtbelllen neerwaarts beginnen te bewegen (zie Figuur S 2). In de praktijk kan met deze balans de richting en snelheid van luchtbelllen bepaald worden. Beide criteria zijn ook direct toepasbaar in het ontwerp van regenwater-opslag tunnels of uitlaatwerken van waterkrachtcentrales; in dergelijke systemen is een goede gecontroleerde ontluchting essentieel om blow-back incidenten te voorkomen. Bovendien zouden twee-fasen-modellen de ontwikkelde kennis kunnen gebruiken om de overgang naar slug flow beter te voorspellen.
- 6 De kritieke watersnelheid, waarbij lange luchtbelllen neerwaarts beginnen te bewegen, is  $v_{sw} = 0.9 \cdot (gD)^{1/2}$  (oftewel  $F_w = 0.9$ ) over een brede range van hellingshoeken ( $5^\circ - 20^\circ$ ). Deze conclusie wordt ondersteund met meetdata van opstellingen met  $D > 0.19$  m en met de ontwikkelde krachtenbalans.
- 7 Een detectiemethode voor de gasbellokatie en het totale gasbelvolume is ontwikkeld en in het veld getoetst.



Figuur S 2: Overzicht van criteria voor de beweging van grote luchtbellen in neergaande leidingen

Het CAPWAT onderzoeksproject (2004 – 2010) heeft geleid tot een beter begrip van de ophoping, de afbraak en het transport van luchtbellen in neergaande leidingen. Het onderzoeksproject heeft tot vele praktische aanbevelingen geleid, die zijn samengebracht in een nieuw handboek voor het hydraulisch ontwerp en beheer van afvalwaterpersleidingen. (Deltares, 2010).

## List of Symbols

Symbol	Unit	Description
$A$	$[m^2]$	Cross-sectional area
$A_D$	$[m^2]$	Pipe cross-section
$a$	$[m^2 / m^3]$	Specific surface of air bubbles
$C$	$[mol/m^3]$	Air bubble concentration
$c$	$[-]$	Empirical constant
$c$	$[m/s]$	Acoustic wave speed
$D$	$[m]$	Internal pipe diameter
$d$	$[m]$	Water depth in channel
$E$	$[Pa]$	Young's modulus of pipe material
$Eo$	$[-]$	Eötvös number, $Eo \equiv \rho_w g D^2 / \sigma$
$e$	$[m]$	Pipe wall thickness
$F$	$[-]$	Flow number, $F \equiv Q / [A_D (gD)^{1/2}]$
$Fr$	$[-]$	Froude number, $Fr \equiv Q_w / [A_w (gA_w T)^{1/2}]$
$f$	$[Hz]$	Frequency
$g$	$[m/s^2]$	Gravitational acceleration
$H$	$[m]$	Energy head
$h$	$[m]$	Pressure head
$K$	$[Pa]$	Liquid bulk modulus
$k_n$	$[m]$	Wall roughness
$k$	$[-]$	Polytropic coefficient of gas pocket
$k_H$	$[mol / (m^3 \cdot bar)]$	Henry's law constant
$L$	$[m]$	Slope length or length of main pipeline
$\dot{m}_a$	$[kg/s]$	Air mass flow rate
$P$	$[s]$	Pipe period for acoustic wave propagation
$p$	$[Pa]$	(absolute) Pressure
$Q$	$[m^3/s]$	Discharge
$q$	$[m^2/s]$	Discharge per unit width
$R$	$[-]$	Reynolds number
$R$	$[m]$	Pipe radius
$R_h$	$[m]$	Hydraulic radius



---

$T$	[m]	Interface width
$T$	[°C]	Water temperature
$u$	[m/s]	Water velocity in channel
$u_*$	[m/s]	Friction velocity
$V$	[m <sup>3</sup> ]	Volume
$v$	[m/s]	Water velocity in pipe
$We$	[-]	Weber number, $We \equiv \rho_w v_{sw}^2 D / \sigma$
$x$	[m]	Longitudinal length parameter
$y$	[m]	Water depth in pipe
$\mathcal{A}$	[m <sup>2</sup> ]	Internal storage area
$\partial H / \partial x$	[-]	Hydraulic gradient
$\Delta H_{fric}$	[m]	Frictional head loss
$\Delta H_g$	[m]	Air pocket head loss
$\varepsilon$	[m <sup>2</sup> /s]	Turbulent air bubble diffusion coefficient
$\theta$	[rad]	Downward pipe angle
$\lambda$	[-]	Pipe friction factor
$\mu$	[Pa·s]	Dynamic viscosity
$\rho$	[kg/m <sup>3</sup> ]	Density
$\sigma$	[N/m]	Surface tension
$\sigma$	variable	Standard deviation

*Subscripts*

<b>Subscript</b>	<b>Description</b>
$a$	air
$b$	Balanced, bubble
$c$	Clearing
$cr$	Critical free surface flow
$d$	Drift, rise
$f$	final
$g$	Gas / air
$h$	Hydraulic (diameter/depth)
$i$	incipient
$n$	Uniform flow condition at normal depth
$p$	Pressurised pipe flow
$s$	Superficial or stagnation or saturation
$w$	Water

---

<i>X</i>	Gas species in gas composition
<i>0</i>	Reference without air pockets
<i>1</i>	Upstream of hydraulic jump or downward sloping reach
<i>2</i>	Downstream of hydraulic jump or downward sloping reach



# 1 Introduction

## 1.1 Air-water flow in pipes

Air-water flow is an undesired condition in many systems for the transportation of water or wastewater. Air in storm water tunnels may get trapped and negatively affect the system (Vasconcelos and Wright, 2009). Air pockets in hydropower tunnels or sewers may cause blow-back events and inadmissible pressure spikes (Capart et al., 1997). Water pipes and wastewater pressure mains in particular are subject to air pocket formation in downward-sloping reaches, such as inverted siphons or terrain slopes. Air pocket accumulation causes energy losses and an associated capacity reduction (Lubbers, 2007). The extra head loss due to the air pocket presence is roughly equal to the vertical distance between the pocket nose and tail (Lubbers and Clemens, 2007). Air pockets in pressurised wastewater mains often are not expelled via air valves, because:

- Hazardous gases may be released,
- Air valves often do not cope with the composition of wastewater and remain closed or, even worse, remain open after the air has been expelled,
- Pressure may be sub-atmospheric at the intended air valve location, and
- Preferred air valve location is on private property or on an inaccessible location for maintenance.

Therefore, air must be transported by the flowing water in many pressurised wastewater mains.

The recent research efforts on air accumulation in storm water tunnels (Vasconcelos and Wright, 2009) or hydropower tunnels (Wickenhäuser and Kriewitz, 2009) confirms the existing knowledge gap on the motion of elongated air pockets in downward sloping pipes. Whereas in horizontal and in upward inclined pipes all entrained air is transported with the water flow, the air in downward sloping pipes can move in both directions. The fundamental momentum balance that predicts when an elongated air pocket becomes stagnant in a downward inclined pipe, is yet to be developed. Knowledge on air pocket motion in downward sloping pipes is essential for the proper venting of pressurized pipes and for the prevention of severe blow-back events.

Finally, the motion of air pockets in downward sloping pipes, is closely related to liquid slugs in inclined pipes carrying gas with a small fraction of liquids (i.e. water, oil and gas condensate). The bubble-shaped interface and gas entrainment at the slug front are two features with great similarity with air pockets in downward sloping pipes. No generally accepted model exists for the prediction of slug occurrence, slug length and frequency (Al-

Safran, 2008; Hurlburt and Hanratty, 2002). Only recently, flow regime independent numerical models deliver reasonable predictions of flow regime transitions in horizontal pipes (Bonizzi et al., 2009). The performance of these models in inclined pipes is not yet known. Therefore, a better understanding of air-water flow in downward sloping pipes may prove valuable for slug flow predictability as well.

## 1.2 Context

Since the Surface Waters Act of December 1<sup>st</sup>, 1970 (Wet Verontreiniging Oppervlaktewateren) has come into force, many wastewater treatment plants were built in the Netherlands. Due to topology of the Netherlands, a significant fraction of the wastewater and polluted storm water has to be pumped to the treatment plants via pressurised mains. Some air was admitted into the pumping stations after each pump stop, because the sealings could not handle negative pressures. Therefore, the presence of air in wastewater mains was inevitable. Kent's design rule (1952) for the mitigation of air pockets, eq. (1.1), has become popular in engineering practice in the Netherlands since the 1970s.

$$v_c = 1.23 \cdot \sqrt{gD \sin \theta} \quad (1.1)$$

where  $v_c$ ,  $g$ ,  $D$  and  $\theta$  are the required velocity for air pocket clearing, constant of gravitational acceleration, pipe diameter and downward pipe angle. The clearing velocity  $v_c$  is the pipe average water velocity to start moving an air pocket in downward direction. Kent's design rule predicts small required water velocities at small downward pipe angles.

The horizontal directional drilling technique (HDD) has become the preferred construction method for inverted siphons since the 1980s. Typical inclination angles with HDD vary from  $5^\circ$  to  $20^\circ$ ; the largest angles can be used for small diameter pipes only. With typical design velocities of 1.5 m/s air can be easily transported through pipes up to  $D = 0.86$  m at  $\theta = 10^\circ$  and up to  $D = 1.7$  m at  $\theta = 5^\circ$ , according to this design rule. Despite Kent's recommendation on verification of his findings at other pipe diameters, equation (1.1) has been applied to pipe diameters up to 1.8 m.

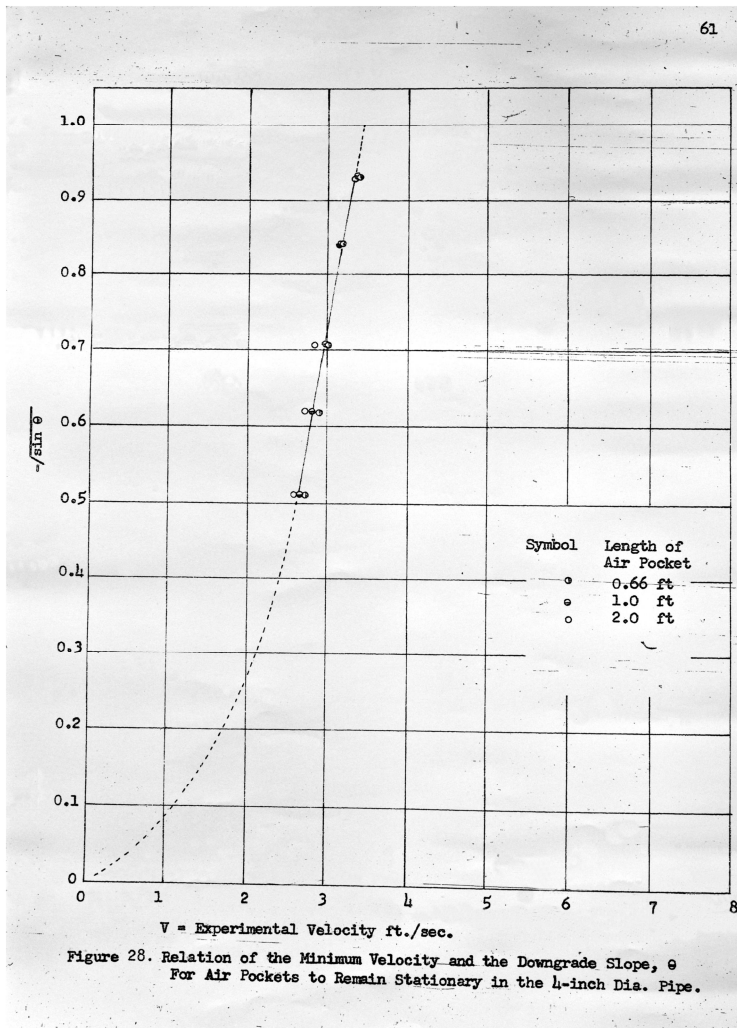


Figure 1.1 Kent's erroneous curve fit on page 61 of his thesis (Kent, 1952).

Unfortunately, Kent made a crucial mistake by graphically fitting his data to the functional relation in equation (1.1). The straight line in Figure 1.1 is different from equation (1.1), because equation (1.1) includes the origin and a linear extrapolation of the experimental data obviously does not. The dotted parabolic curve is incorrect.

Wisner *et al.* (1975) reported the correct curve fit to Kent's experimental data, but this improved correlation has never reached the engineering practice in the Netherlands.

$$v_c / \sqrt{gD} = 0.55 + 0.5\sqrt{\sin \theta} \quad (1.2)$$

The ongoing scale-up of wastewater treatment plants demands for a more robust and reliable wastewater transportation system. The largest wastewater treatment plants (WWTP) in the Netherlands serve about 1 million inhabitants each (Table 1.1). Their treatment capacity is in the order of 1 million inhabitant equivalents (i.e.).

Table 1.1: Overview of large WWTPs and transportation systems

Treatment plant	Capacity		Pressurised main length (km)	Largest diameter (m)	Pumping stations (-)	Booster stations (-)
	(10 <sup>6</sup> i.e.)	(m <sup>3</sup> /s)				
Harnaspolder, Delft	1.3	9.9	57	1.8	14	0
West-Amsterdam	1.0	8.1	90	1.6	35	4
Eindhoven	0.75	7.3	26	1.0	10	0
Bath (NB)	0.52	4.5	44	1.8	31	2

These large centralised treatment plants rely on robust wastewater transportation systems. A capacity problem in these large transportation systems causes combined sewer overflows, urban flooding and consequential damage to the receiving waters and possibly public health.

Water Board West-Brabant (Kamma et al., 1995) investigated pipelines with capacity problems and reported fluctuating hydraulic gradients with friction factors varying from 0.018 to 0.032. Kamma suspected the presence of accumulated gas pockets in inverted siphons. A first workshop on gas pockets in wastewater mains was organized by Delft Hydraulics (Lemmens, 1996). The Dutch water industry did not recognize the problems associated with capacity reducing gas pockets at that time, partially due to the absence of flow metering devices in wastewater mains. Since the 1990s, the installation of electromagnetic flow meters became common practice in pumping stations and more capacity problems were identified. A second workshop in 2002 led to the initiation of the joint research project CAPWAT, which is an abbreviation of *CAPacity reduction and hydraulic losses in wasteWATER mains*.

This thesis is part of this joint research project CAPWAT. CAPWAT was started in 2004 by Deltares, Delft University of Technology and sixteen co-funding partners from the water industry, including ten water boards, three consultants, one pump manufacturer, STOWA<sup>1</sup>,

1. STOWA: Dutch foundation for applied research in water management and wastewater treatment. STOWA is mainly funded by the water boards.

Stichting RIONED<sup>2</sup> and the Ministry of Economic Affairs. A first PhD thesis was delivered within the CAPWAT project in 2007 (Lubbers, 2007). The most important cause of a deteriorated performance of an urban drainage system is pump failure (Korving et al., 2006). If the pumping station is functioning correctly, then 90% of the capacity reductions are caused by gas accumulations in inverted siphons, according to the CAPWAT participants.

Apart from the environmental damage in terms of sewer overflows and urban flooding, the gas accumulations in wastewater mains cost 3 M€ 19 million kWh and 10,000 ton CO<sub>2</sub> per annum for pumping energy (Pothof et al., 2009).

### 1.3 Structure of thesis

Chapter 2 presents a literature survey on air-water flows in downward sloping pipes and details a number of possible transport mechanisms, such as entrainment in the hydraulic jump, surface entrainment and dissolving of air in the water phase. The research questions addressed in this thesis result from the literature survey.

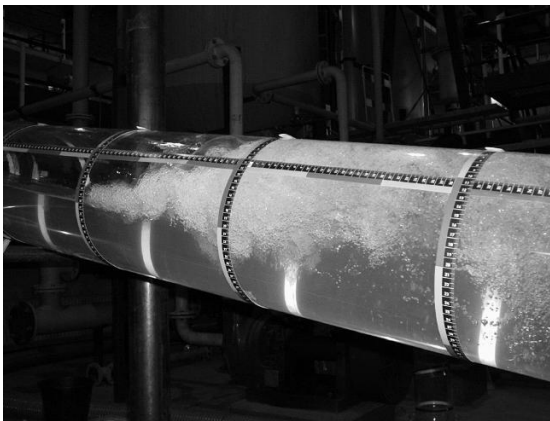


Figure 1.2: Gas entrainment in the hydraulic jump

The new and available experimental data on co-current air-water flow in downward sloping pipes are outlined in chapter 3. This chapter contains a dimensional analysis, a description of the experimental facilities, the test procedures, an uncertainty analysis and an overview of the experimental results. The experimental results include descriptions of observed flow

---

2. *Stichting RIONED: Dutch foundation for sewer management and urban drainage. Stichting RIONED is mainly funded by municipalities.*



regimes and an initial analysis of the influence of important parameters, such as the pipe diameter, length of the inclined section, surface tension and absolute pressure. Under certain conditions, multiple elongated air pockets were observed, under other conditions only one elongated air pocket was observed. Chapter 4 aims to answer two fundamental questions: (1) which criterion defines the transition from a single to multiple elongated air pockets and (2) in which direction move these elongated air pockets? An energy balance and a momentum balance are exploited to address these fundamental questions in chapter 4. Chapter 5 uses the results from chapter 4 to develop an analytical air transport model. The new model is calibrated against available experimental data. The air transport model is particularly useful in practice, if the presence of air pockets can be detected before the air pockets create an excessive extra head loss. Such an air pocket detection method is detailed in chapter 6. This detection method aims at predicting the air pocket location and volume. Two practical applications from pressurised wastewater mains are outlined in chapter 7. Chapter 8 presents the conclusions and recommendations from this thesis.

## 2 Literature review

This chapter extends conference papers, presented at the Int. Conference on Urban Drainage (Pothof and Clemens, 2008b) and the 33<sup>rd</sup> IAHR World Congress (Pothof and Clemens, 2009).

This chapter focuses on the presence of air and gas pockets in wastewater pipelines and on air transport mechanisms. Literature related to the detection of air pockets, will be summarised in chapter 6.

### 2.1 Gas pockets in wastewater mains

Gas pockets in wastewater mains originate from a number of sources:

- 1 free-falling jet in the pump pit,
- 2 pump stop,
- 3 leaks,
- 4 air valves and
- 5 biochemical processes.

Air may entrain continuously in case the sewer outflow is a free-falling jet into the pump pit (Kranendonk, 2007; Smit, 2007). Kranendonk has shown that the air entrainment via plunging jets may easily exceed the air transport capacity of downward sloping sections.



Figure 2.1 Air entraining plunging jets in the lab (Kranendonk, 2007) and the field

Air may also entrain discontinuously after pump stop if the pump inertia is sufficient to drain the pit down to the bell-mouth level. This kind of discontinuous air entrainment occurs mainly in wastewater systems with a marginal static head. Another transient phenomenon causing an inflow of air, however more unlikely, is a pump trip in a dendritic pressurised wastewater system. The induced transient may suck wastewater from an idle pumping station, causing air entrainment in the idle pumping station.

If the pipeline is subject to negative pressures during normal operation or during transients, then air may leak into pipeline or may enter intentionally via air valves.

Another possible cause of gas pocket development consists of biochemical processes in the pipeline, mainly  $\text{CO}_2$ ,  $\text{H}_2\text{S}$ ,  $\text{N}_2$  and  $\text{CH}_4$ . Carbon dioxide and hydrogen sulphide are highly soluble in water. Hydrogen sulphide ( $\text{H}_2\text{S}$ ) production is limited by the availability of sulphur-ions ( $\text{S}^{2-}$ ). The design concentration of sulfides in domestic wastewater is 100 mg/ltr (Butler and Davies, 2009), from which at most 35.4 mg( $\text{H}_2\text{S}$ )/ltr may be produced. The solubility of  $\text{H}_2\text{S}$  is temperature dependent (Table 2.1), but exceeds the dissolved  $\text{H}_2\text{S}$  concentration with a factor 100 or more. Therefore, the partial  $\text{H}_2\text{S}$  pressure in a gas pocket will be at most 1% of the total pressure and hydrogen sulphide may be eliminated from the above list of components in a capacity reducing gas pocket. Analyses of gas samples from long pressurised wastewater mains confirms the dominant presence of methane ( $\text{CH}_4$ ) and nitrogen ( $\text{N}_2$ ) (Lemmens, 1996).

Table 2.1 Solubility of hydrogen sulphide in water

Temperature [ $^{\circ}\text{C}$ ]	Solubility [mg/ltr/bar]
0	6800
13	5100
20	3900
30	3200

Pressurised wastewater mains are characterized by an intermittent operation. If air bubbles are present in wastewater, then they will accumulate in elevated sections of the pipeline during shut down periods and dry weather flow conditions. If an air pocket is present in the top of a declining section and water is flowing through the conduit, then a hydraulic jump will develop at the tail of the gas accumulation. The hydraulic jump ejects air bubbles from the air accumulation (Figure 1.2). The pumping action of the hydraulic jump transports part of the ejected air down to the bottom of the declining section, as schematized in Figure 2.2.

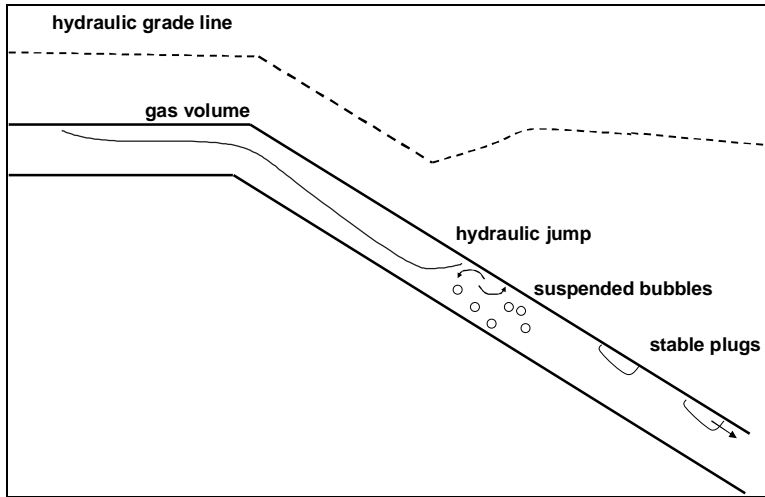


Figure 2.2: Schematic overview of downward gas transport by flowing water.

## 2.2 Air-water flow in downward sloping pipes

This section provides an overview of available literature on gas transport in downward sloping pipes. Since the terminology stems from air-water flows in horizontal pipes, the possible flow regimes in horizontal pipes are briefly summarised. The flow regimes that may occur in horizontal pipe flow (Falvey, 1980), are sketched in Figure 2.3.

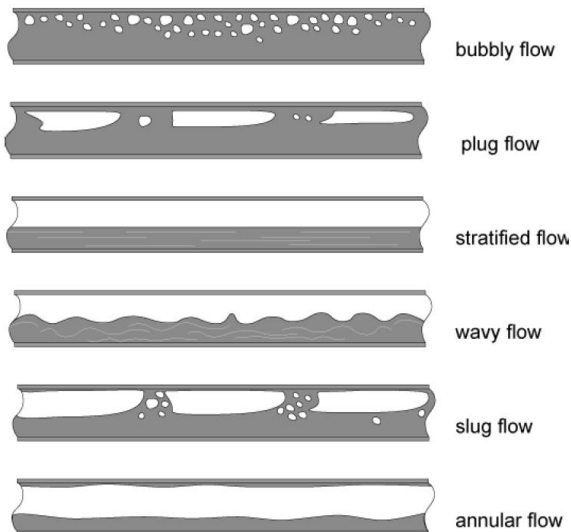


Figure 2.3: Possible flow regimes in horizontal pipes.

The slug and plug flow regimes are the most relevant ones within the context of this thesis. A slug is defined as a liquid blockage propagating down the pipe whose front may be approximated by a single stage hydraulic jump (Ruder and Hanratty, 1990). Air or gas enters the liquid slug at the hydraulic jump. In the plug flow regime, plugs of gas and liquid flow alternately along the top of the pipe. Gas-entrainment is essentially absent in the plug flow regime.

The overview of literature on air-water flow in downward sloping pipes is presented in chronological order and the applicability of the results for pressurised wastewater pipelines is briefly discussed.

Among the oldest available research works in the field of liquid driven gas transport in downward sloping pipes are the publications by Kalinske and Bliss (1943) and Kalinkse and Robertson (1943).

Kalinske and Bliss described three distinct flow regimes (Kalinske and Bliss, 1943):

- A blow-back flow regime at relatively small water discharges, although still above the critical discharge in (2.1). In this flow regime, the bubbles coalesce and periodically blow back upward, which limits the net gas transport. The net gas transport is controlled by the flow characteristics below the hydraulic jump, which are described by a Froude-scaled dimensionless velocity; see eq. (2.2).
- A full gas transport or plug flow regime at higher water discharges, at which all entrained gas bubbles are transported to the bottom of the downward slope. The gas transport becomes almost independent of the dimensionless velocity in this flow regime. Kalinske and Bliss (1943) conclude that the Froude number upstream of the hydraulic jump determines the gas transport.
- At the transition from the blow-back flow regime to the plug flow regime, a series of 2 to 4 stationary gas pockets and hydraulic jumps were observed in the downward slope. The length of the downward slope of their test rig was 10.5 m long. Blow-back did not occur any more in this transitional flow regime.

They determined the dimensionless water discharge  $Q^2/(gD^5)$  at which gas bubbles are ripped off the air accumulation by the hydraulic jump and start to move downward to the bottom of the slope. Kalinske and Bliss (1943) proposed the following relation for this incipient downward air transport, based on experiments in pipes with  $D = 0.10$  m  $D = 0.15$  m:

$$\frac{Q_i^2}{gD^5} = \frac{\sin \theta}{0.71} \quad (2.1)$$

where  $Q_i$  refers to the water discharge for *incipient* air transport. Kalinske et al. defined the pipe slope as the sine of the angle with the horizontal plane.

This equation cannot be considered an equation for the clearing velocity, as explained by Kalinske and Bliss: “..to maintain proper air removal, the actual value of the water discharge should be appreciably larger than  $Q_i$ ” (Kalinske and Bliss, 1943). In fact, this curve may depend on the length of the downward slope, which was 10.5 m (i.e.  $105 \cdot D$  for the 100 mm pipe and  $70 \cdot D$  for the 150 mm pipe). Equation (2.1) is equivalent with:

$$\frac{v_i}{\sqrt{gD}} = \frac{Q_i}{(0.25\pi D^2)\sqrt{gD}} = \frac{4}{\pi} \frac{Q_i}{D^2\sqrt{gD}} = \frac{4}{\pi} \sqrt{\frac{\sin \theta}{0.71}} \quad (2.2)$$

The left-hand side of equation (2.2) is known as the Pipe Froude number or Flow number  $F$ , defined as the superficial phase velocity divided by  $(gD)^{1/2}$ .

$$F \equiv \frac{v}{\sqrt{gD}} = \frac{Q}{(0.25\pi D^2)\sqrt{gD}} \quad (2.3)$$

The flow number applies to the water phase, denoted by  $F_w$ , and to the air/gas phase, denoted by  $F_g$ . The term flow number will be used in this thesis in order to avoid confusion with the Froude number of the stratified water film, which drives the air entrainment in hydraulic jumps at  $Fr > 1.5$ , where the Froude number is defined as

$$Fr \equiv \frac{v_w}{\sqrt{gA_w/T}} = \frac{Q_w}{A_w\sqrt{gA_w/T}} \quad (2.4)$$

Here  $v_w$ ,  $A_w$  and  $T$  are the water film velocity  $Q_w/A_w$ , the water cross section and the interface width at the toe of the hydraulic jump.

Kalinske and Robertson (1943) also determined the gas transport by measuring the gas pocket length reduction during a certain time interval. The time was started after the hydraulic jump had moved up “an appreciable distance from the end of the pipe” (Bliss, 1942). Kalinske *et al.* (1943) established the following correlation from experimental data in pipes at downward inclination up to  $\theta = 8.6^\circ$  (or slope = 15%).

$$\frac{Q_g}{Q_w} = \frac{F_g}{F_w} = 0.0066(Fr_1 - 1)^{1.4} \quad (2.5)$$

where  $Q_w$ ,  $Q_g$  and  $Fr_1$  are the water discharge, air discharge and the Froude number of the water film upstream of the air-entraining hydraulic jump.

The transition from the blow-back to the plug flow regime is highly relevant from a practical point of view, because the gas pocket head loss in the plug flow regime is negligible. Bliss has reported this transition in his research report only (Bliss, 1942); these results have not yet been published elsewhere to the authors' knowledge. The transition to plug flow requires a significantly larger dimensionless velocity than the more widely reported 'incipient air transport' according to equation (2.1). Bliss reported that plug flow occurred at lower water flow rates, if the gas pocket was not held in position by the roughness of a joint or a projecting point gage. The results in Figure 2.4 apply to the required velocities with a projecting point gage at the beginning of the downward slope, because Bliss anticipated that any prototype pipe would contain sufficient roughness elements to hold a gas pocket in position in the top of the downward slope. Finally Bliss noted that the 4" pipe required smaller clearing velocities than the 6" pipe; the difference was not quantified.

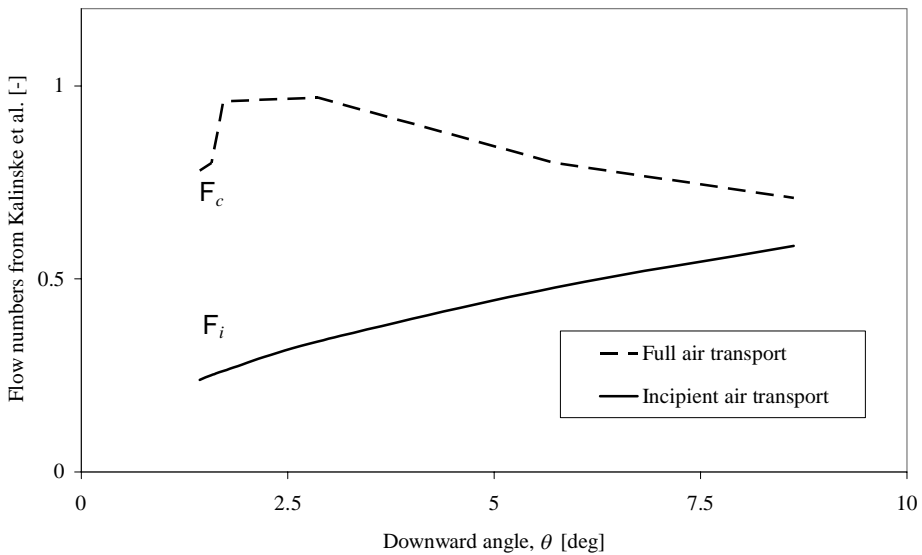


Figure 2.4 Required dimensionless velocities for 'start of gas transport' (Kalinske and Bliss, 1943) and clearing velocity (Bliss, 1942).

This test setup was in reasonable agreement with the practical situation in which an air pocket has accumulated in the top of a downward sloping section. The upstream pipework consisted of an inclining pipe at 45 degrees followed by an appropriate bend towards the downward slope; the test rig did not include a horizontal section upstream of the downward sloping section.

Kent (1952) has performed detailed experiments in a 33 mm pipe and a 102 mm (4") pipe on *stationary* gas pockets in declining pipes with pipe angles varying between 15° and 60°. The length of the downward slope was 5.5 m (18 ft) for the 102 mm pipe. Since the gas pockets are stationary, the flow regime is similar with Kalinske's transitional flow regime between blow-back and full gas transport. An important difference, however, is the fact that Kent injected air in the downward sloping reach rather than upstream of it.

Kent focused on the determination of the drag coefficient,  $C_D$ , as a function of the plug length,  $L_b$  and the maximum projected plug area,  $A_b$ . Kent's gas pockets were large enough to form a hydraulic jump at the tail of the gas pocket. In order to maintain a constant gas pocket volume, Kent continuously injected air in the stationary pocket. He measured the total air volume in the downward sloping reach by rapidly closing two valves at the beginning and end of the inclined section simultaneously, after which he could measure the total gas volume in the isolated section. This enabled Kent to determine the total buoyant force, which must balance the drag force, because the gas pocket remained stationary. Kent established the following relation from his experiments:

$$F_c = \frac{v_c}{\sqrt{gD}} = 1.23 \cdot \sqrt{\sin \theta} \quad (2.6)$$

A clearly better curve fit on Kent's data, which allows for a non-zero offset is given in equation (2.7); see (Mosvell, 1976), (Lauchlan, 2005) and (Wisner et al., 1975), who first published the systematic deviation between Kent's data and equation (2.6); see Figure 1.1 and Figure 2.5.

$$F_c = 0.55 + 0.5 \cdot \sqrt{\sin \theta} \quad (2.7)$$

Equation (2.7) is valid for gas pockets with a dimensionless length  $L/D$  exceeding 1.5, which coincides with a gas pocket volume exceeding 0.55D in full pipe diameters ( $n \equiv Vol / (A_D \cdot D) > 0.55$ ). Unfortunately, the incorrect Equation (2.6) has been used frequently in the design of Dutch sewerage mains; even for pipe angles smaller than 15°, where the difference is most pronounced.

Kent's datapoints with stationary air pockets were re-analysed to obtain a correlation between the air-water discharge ratio and the upstream Froude number. This correlation is independent of the pipe inclination ( $R^2 = 0.97$ ):

$$\frac{Q_g}{Q_w} = \frac{F_g}{F_w} = 0.0212(Fr_1 - 1)^{1.59} \quad (2.8)$$



It must be noted that Kent's setup is not a perfect representation of gas transport in wastewater or water pipelines, because Kent injected air in the downward sloping reach.

Kent also performed measurements on relatively small air plugs from which no bubbles were ejected by the hydraulic jump. These measurements, which have not been published before except for in Kent's thesis (Kent, 1952), reveal that both the maximum stable plug length and the clearing velocity decreases at steeper slopes (Figure 2.5); the length of a gas plug or gas pocket is defined as the distance from the upstream end (or nose) of the gas plug to the impingement point of the hydraulic jump. The stable plug flow number decreases in the pipe angle, which indicates that air may be transported more easily at steeper pipe angles in the plug flow regime.

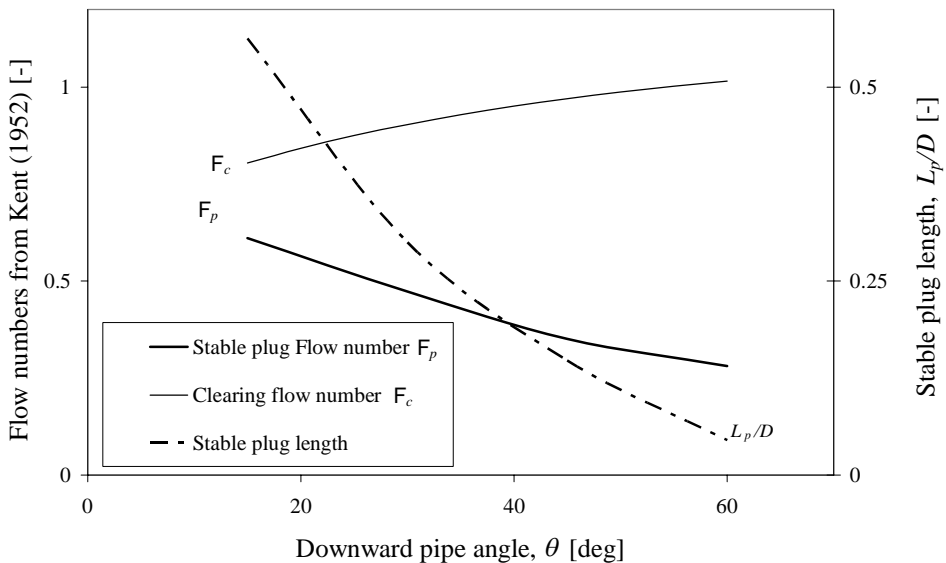


Figure 2.5. Required dimensionless clearing velocities for large pockets with air entraining hydraulic jumps and for stable pockets without air entrainment. The maximum stable pocket length is indicated as well.

Gandenberger (1957) has performed measurements on individual stationary pockets and pockets moving downward in various pipes with internal diameter between 10 mm and 100 mm at downward angles between  $5^\circ$  and  $90^\circ$  (Figure 2.7). Most of Gandenberger's results are based on measurements in a 45 mm glass pipe. Gandenberger measured a maximum clearing velocity at  $40^\circ$ . He investigated gas pocket volumes up to  $n = 1.5$  and found that the gas pocket velocity becomes constant if the gas pocket volume  $n > 0.5$  at all pipe angles, which confirms Kent's results. The applicability of Gandenberger's

measurements for downward gas transport in water pipelines has the same limitations as Kent's results. A further limitation of Gandenberger's measurements is the fact that Gandenberger did not inject air to maintain a constant pocket volume. Hence, the bubbly flow at the tail of the hydraulic jump could not be maintained during the experiments. Gandenberger's clearing velocities are slightly smaller than Kent's velocities, which may be attributed to the smaller pipe diameter or to the lack of air injection in the pocket.

Nicklin et al. (1962) have proposed the drift flux model for the motion of elongated bubbles in vertical pipes.

$$v_b = c_0 v_{sm} + v_d = c_0 (v_{sw} + v_{sg}) + v_d \quad (2.9)$$

Here  $v_b$ ,  $v_{sm}$ , and  $v_d$  are the bubble velocity, the superficial mixture velocity and the drift velocity. The superficial velocity, denoted by subscript  $s$ , is the velocity based on the entire pipe cross sectional area. The drift velocity is the bubble rise velocity in a stagnant liquid. The coefficient  $c_0$  is an empirical constant. Division by  $(gD)^{1/2}$  expresses the drift flux model in terms of water, air and drift flow numbers  $F_w$ ,  $F_g$  and  $F_d$ .

$$\frac{v_b}{\sqrt{gD}} = c_0 (F_w + F_g) + F_d \quad (2.10)$$

Zukoski (1966) has shown that the drift flow number in vertical pipes converges to  $F_d = 0.35$  for Eötvös number  $EO > 40$  or pipe diameter  $D > 0.017$  m for air-water systems. The Eötvös number  $EO$  is a dimensionless number characterising the ratio of the gravity force and the surface tension force.

$$EO \equiv \rho_w g D^2 / \sigma \quad (2.11)$$

where  $\rho_w$  and  $\sigma$  are the water density and surface tension. The drift flow number is closely related to the clearing flow number  $F_c$ . At the clearing flow number of an individual elongated air pocket, the air pocket just stabilises, so that the net air transport is zero. Hence in eq. (2.10):  $v_b = 0$ ,  $F_g = 0$  and  $F_w = F_c$ , yielding:

$$0 = c_0 F_c + F_d \quad (2.12)$$

Bendiksen (1984) has shown experimentally that  $c_0 = 0.98$  for downward pipe angles  $\theta \leq 30^\circ$ . It is noted that this result was obtained in small diameter pipes ( $D = 0.0242$  m).

Wisner *et al.* (1975) recognized the large spread in proposed clearing velocities for downward gas transport in the literature up to 1975 including Gandenberger (1957), Kalinske *et al.* (1943) and Kent (1952). Wisner assumed that scale effects could have

caused the large spread and therefore performed experiments in a large 245 mm pipe at a fixed downward angle of 18°. Wisner focused on stable plugs rather than the clearing velocity in his experiments. Finally, Wisner et al. developed an envelope curve from the available data from Veronese (1937), Gandenberger, Kent and Kalinkse and found:

$$F_c = \frac{v_c}{\sqrt{gD}} = 0.825 + 0.25 \cdot \sqrt{\sin \theta} \quad (2.13)$$

Falvey (1980) has combined several literature sources to obtain an expression for the clearing velocity (Figure 2.7).

Escarameia *et al.* (2007) have performed experiments in a 150 mm pipe with gas pockets up to 5 litres ( $n = 1.9$ ) and pipe angles up to 22.5°. Escarameia proposed the following formula for the dimensionless clearing velocity, which extends Kent's data, eq. (2.7), to angles smaller than 15°:

$$F_c = \frac{v_c}{\sqrt{gD}} = 0.61 + 0.56 \cdot \sqrt{\sin \theta} \quad (2.14)$$

The same limitations as mentioned in Kent's paragraph apply to these results. Escarameia (2007) also derived an expression for the air-water discharge ratio, which was verified at pipe angles up to  $\theta = 16.7^\circ$ .

$$\frac{Q_g}{Q_w} = \frac{F_g}{F_w} = 0.0025 (Fr_1 - 1)^{1.8} \quad (2.15)$$

The effect of air pocket length, air discharge and pipe diameter on the clearing flow number is considerable, yet this was investigated only recently by Lubbers (2007). Lubbers has performed experiments in three different pipe sizes ( $D = 0.11$  m, 0.22 m and 0.50 m), with different lengths of the inclined section and at various downward slopes from 5° to 30° and 90°. Lubbers injected air upstream of the inclined reach in a horizontal section and determined the extra head loss due to the gas accumulation at different combinations of air and water discharge. The clearing velocity (or critical velocity) is reached when the extra head loss due to the presence of the gas flow attains a minimum. This minimum gas pocket head loss value is close to zero. Lubbers found that the largest clearing velocity is required at downward pipe angles of 10° to 20°. Figure 2.6 shows a gradual drop in clearing velocity at pipe angles steeper than 20°. The clearing flow number drops to about 0.4 for a vertical pipe with  $D = 0.22$  m. A comparison of the clearing velocities at a downward slope of 10° and the three pipe sizes, revealed that the clearing velocity at  $D = 0.11$  m was smaller than at the two larger diameters  $D = 0.22$  m or 0.50 m.

Wickenhäuser and Kriewitz (2009) have determined the maximum air discharge as a function of downward pipe angle and water discharge in the plug flow regime – i.e. without air accumulation in the downward sloping reach.

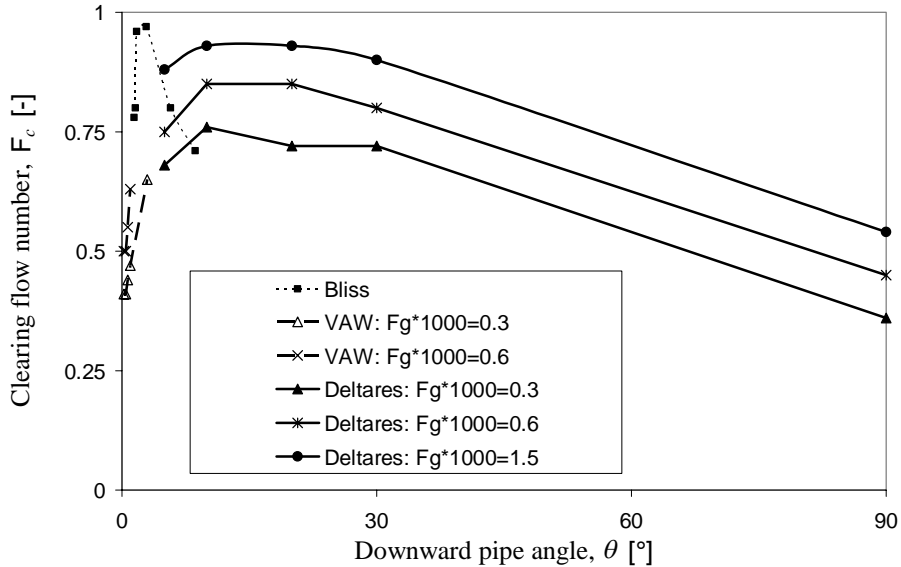


Figure 2.6 Correlations for the clearing flow number at various gas discharges with data from Bliss (1942), Wickenhäuser and Kriewitz (2009) and Lubbers (label Deltares, 2007).

### 2.2.1 Discussion

The experimental data from Bendiksen (1984), Gandenberger (1957), Kent (1952), and Escaramia (2007) on the motion of an individual elongated air pocket are combined in Figure 2.7, revealing similar trends in the clearing flow number. The differences between the results seem to be caused by diameter differences, which induce a Reynolds number influence and possibly a surface tension influence. The Reynolds number influence is included in the friction factor. A logical extension of the dimensionless clearing velocity is the clearing velocity multiplied with the square root of the pipe friction factor  $\lambda^{1/2}$ , yielding:

$$F_{fc} \equiv \sqrt{\frac{\lambda}{gD}} v_c \quad (2.16)$$

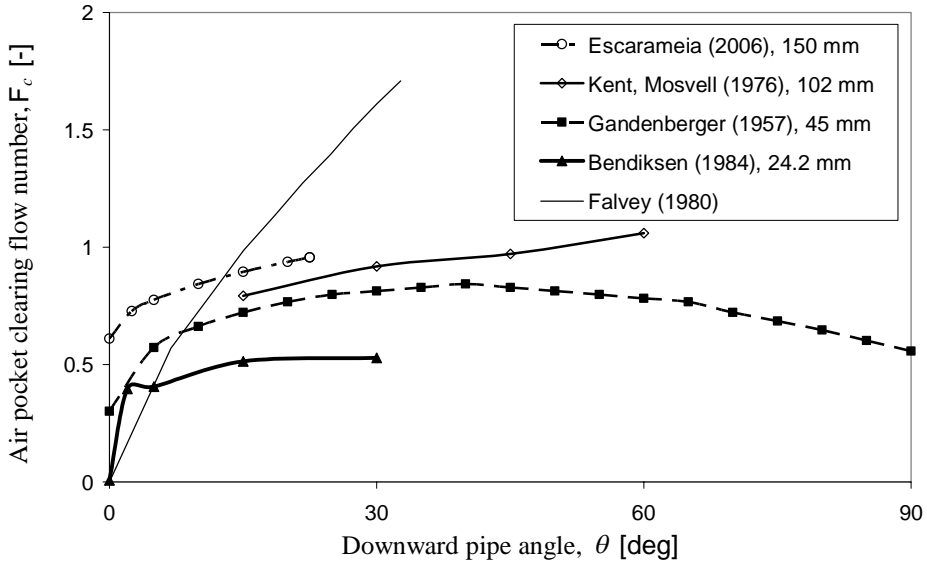


Figure 2.7 Correlations for the clearing flow number of individual air pockets.

In fact, this definition implies that the hydraulic grade lines are identical if the dimensionless clearing velocities including friction, are identical, as illustrated for pipe diameters  $D_1$  and  $D_2$  in equation (2.17):

$$\frac{\partial H}{\partial x}(D_1) = \frac{\partial H}{\partial x}(D_2) \Leftrightarrow \frac{\lambda}{D_1} \frac{v_{sw}^2(D_1)}{2g} = \frac{\lambda}{D_2} \frac{v_{sw}^2(D_2)}{2g} \Leftrightarrow$$

$$\Leftrightarrow F_{fc}(D_1) = \sqrt{\frac{\lambda}{gD_1}} v_{sw}(D_1) = \sqrt{\frac{\lambda}{gD_2}} v_{sw}(D_2) = F_{fc}(D_2) \quad (2.17)$$

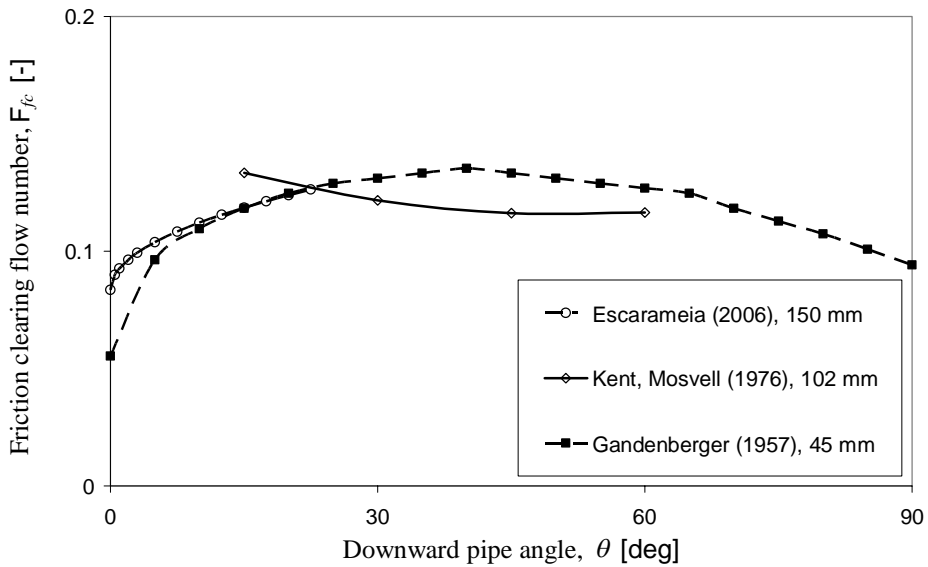


Figure 2.8 Friction clearing flow number, derived from various experiments

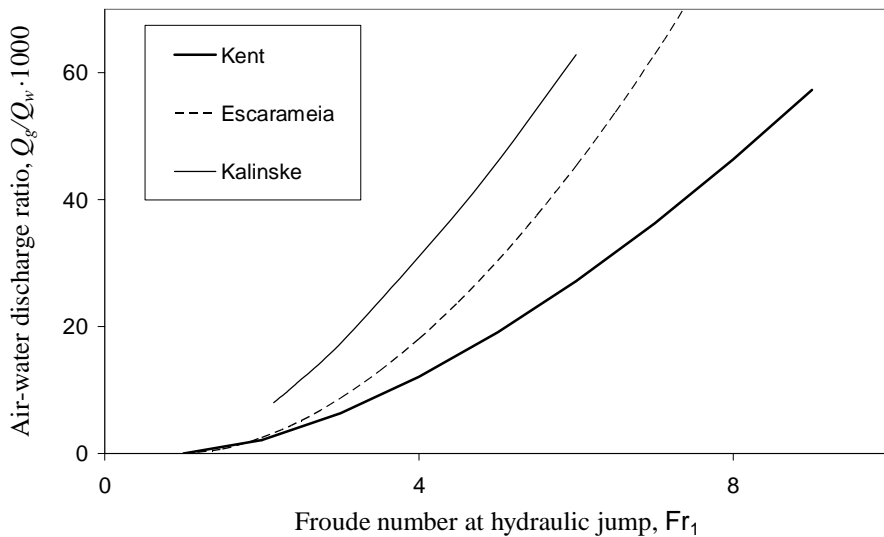


Figure 2.9 Experimental correlations of the air-water discharge ratio. Kent's (1952) correlation was validated at  $D = 0.101$  m and pipe angles in the range  $15^\circ \leq \theta \leq 60^\circ$ . Kalinski's (1943) and Escarameia's (2007) correlations were validated at  $D = 0.15$  m and pipe angles up to  $\theta = 16.7^\circ$ .

Figure 2.8 suggests that a flow number including friction explains the scale effect at pipe diameters  $D \leq 0.15$  m. This suggestion will be addressed in paragraph 5.4 of this thesis.

Figure 2.9 shows a large spread in available experimental correlations between the water Froude number and the air-water discharge ratio, suggesting that the modelling approach in equations (2.5), (2.8) and (2.15), based on the Froude number preceding the hydraulic jump, may be feasible for the air entrainment rate, but it is incomplete for the modelling of the net air transport at the bottom of a downward sloping section. Lubbers' air pocket head loss measurements show that the air pocket length also affects the net air discharge. The influence of the air pocket length on the net air discharge at the bottom of the downward sloping reach will be discussed in detail in this thesis.

### 2.3 Air transport by hydraulic jumps

Since the pumping action of hydraulic jumps is an important mode of air transport, literature on hydraulic jumps may be valuable. A number of properties of hydraulic jumps, like the sequent depth ratio, velocity profiles and local void fraction have been investigated over the last century; overviews are provided in a number of books (Chanson, 1996; Hager, 1993; Rajaratnam, 1967). Air entrainment in rectangular horizontal channels by hydraulic jumps has been extensively investigated (Chanson and Brattberg, 2000; Gualtieri and Chanson, 2007; Hager, 1993).

The transport of air bubbles from the impingement point through the hydraulic jump is essentially an advection-diffusion problem, driven by turbulent diffusion (Chanson, 2004). However, the literature on turbulent kinetic energy profiles in decelerating jets is scarce. Rouse (Rouse et al., 1959) has performed turbulence measurements and derived the dominant terms in the turbulence equations. Rouse's experiments were performed in an air duct, which causes differences with proper hydraulic jumps due to the absence of a free surface and gas entrainment. Further measurements of turbulent shear stress and turbulent kinetic energy were performed in the 1970s (Resch and Leutheusser, 1972; Resch et al., 1976). Svendsen *et al.* (2000) have investigated weak hydraulic jumps without gas entrainment. Only very recently, other turbulence characteristics, like the axial turbulence intensity and integral length scale of vortices, have been investigated (Kucukali and Chanson, 2008; Murzyn and Chanson, 2008).

Hydraulic jumps with fully developed inflow conditions differ significantly from hydraulic jumps with undeveloped inflow conditions. The influence of skin friction on the sequent depth ratio is limited to about 3% of the Bélanger equation,  $d_2 / d_1 = 0.5 \cdot [(1+8 \cdot Fr^2)^{1/2} - 1]$ ,

for non-developed inflow conditions (Hager and Bremen, 1989). Resch and Leutheusser have measured similar skin friction effects in their non-developed inflow experiments. However, in fully developed inflow, the sequent depth is 10% smaller than predicted by the Bélanger equation (Resch et al., 1976), as illustrated in Figure 2.10.

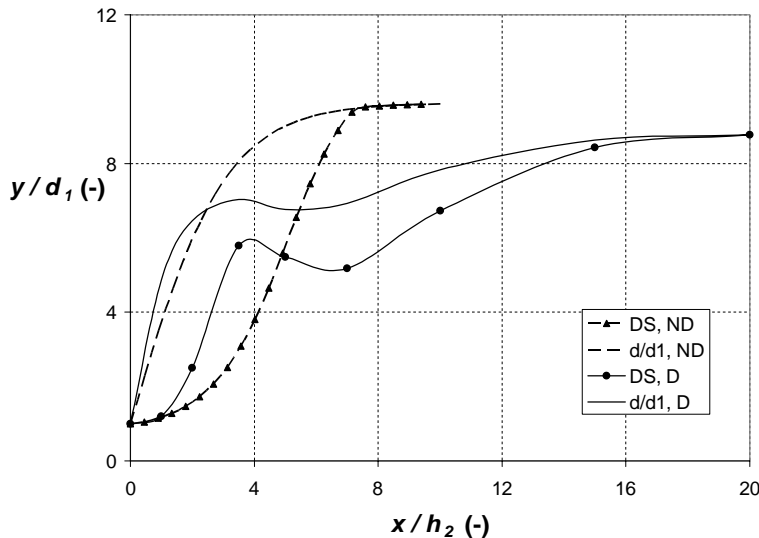


Figure 2.10 Dividing streamlines (DS, marked lines) and water level in hydraulic jump for non-developed (ND, dotted lines) and developed (D, solid lines) inflow conditions at  $Fr_1=7.3$ . Non-developed data from (Hager, 1993), developed data from (Resch et al., 1976).

Further inspection of the dividing streamlines in Figure 2.10 shows that the fully developed inflow decelerates more quickly between the impingement point and  $x = 4d_2$ . This initial deceleration is triggered by the fluid properties at the free surface of the inflowing jet. The turbulent kinetic energy at the free surface is non-zero for a developed inflow,  $k = 0.65 \cdot u_*^2$  (Nezu, 1993), but zero for a non-developed inflow. These observations indicate that the upstream turbulent kinetic energy  $k_i$  affects the downstream water level and dividing streamline profiles in the hydraulic jump.

Inspection of suspended bubble measurements by Resch *et al.* (1974) shows that bubbles remain suspended considerably longer in a hydraulic jump with developed inflow, especially at a distance greater than  $6d_2$ . Since the turbulence production has diminished at  $6d_2$ , the bubble dispersion beyond this location must be driven by the turbulent kinetic energy  $k$ . The increased aeration length may also be explained by a smaller average bubble



size in hydraulic jumps with fully developed inflow, but the available experimental is not conclusive on this issue.

### 2.3.1 Discussion on air transport by hydraulic jumps

The eddy viscosity is a key parameter in mixing and diffusion problems in fluid dynamics. Air bubbles diffuse in the turbulent shear layer in a hydraulic jump (Chanson and Brattberg, 2000). The current approach to suspended bubble modelling in hydraulic jumps is based on the vertical mixing equation (2.18), neglecting the bubble rise velocity in the hydraulic jump (Chanson, 2004).

$$u_1 \frac{\partial C}{\partial x} = \varepsilon_y \frac{\partial^2 C}{\partial y^2} \quad (2.18)$$

where  $C$ ,  $u_1$ ,  $\varepsilon_y$  are the suspended bubble concentration, upstream average channel velocity and vertical turbulent diffusion coefficient. Chanson has analysed the air bubble diffusion and found (Chanson, 2004):

$$\varepsilon_y \approx 0.04 \cdot d_1 \cdot u_1 \approx 0.7 \cdot d_1 \cdot u_{*1} \quad (2.19)$$

where  $u_{*1}$  is the upstream friction velocity.

The increased mixing coefficients are due to the local deceleration losses in the hydraulic jump. The author of this thesis proposes to model the eddy viscosity in a more generalized way by focusing on the a priori knowledge of the macroscopic energy loss.

**Scaling of turbulent mixing.** The eddy viscosity and bubble diffusion coefficient should be derived from both the skin friction losses and local deceleration losses. Since the friction velocity  $u_*$  represents the energy losses due to skin friction, it is possible to rephrase the friction velocity in terms of the local hydraulic grade line:

$$u_* = \sqrt{\frac{\lambda}{8}} u = \sqrt{g R_h} \sqrt{\frac{\partial H}{\partial x}} = \sqrt{\frac{g A}{P}} \sqrt{\frac{\partial H}{\partial x}} \quad (2.20)$$

where

$u$	[m/s]	Advective channel velocity
$\lambda$	[-]	White-Colebrook friction factor for pipe or channel flow
$x$	[m]	Flow direction parallel to channel bottom
$\partial H / \partial x$	[-]	Hydraulic gradient, $H(x) = d + u^2 / 2g$
$R_h$	[m]	Hydraulic radius
$A$	[m <sup>2</sup> ]	Wet cross section
$P$	[m]	Wet perimeter

Now, the diffusion coefficient can be expressed as a function of the hydraulic gradient, that may be affected by skin friction and local losses.

$$\varepsilon_y \sim d \cdot u_* \sim \left( g d^3 \frac{\Delta H}{L} \right)^{1/2} \quad (2.21)$$

where  $d$  and  $\Delta H/L$  are a certain length scale – typically the upstream water depth – and the hydraulic gradient, based on the deceleration length of local losses.

The integrated macroscopic deceleration loss for a 1D duct flow or hydraulic jump are the well known Borda-Carnot  $\Delta H_{BC}$  and hydraulic jump  $\Delta H_{HJ}$  head loss equations, derived from the overall momentum and energy balance.

$$\text{Borda-Carnot} \quad \Delta H_{BC} = \left( 1 - \frac{A_2}{A_1} \right)^2 \frac{v_2^2}{2g} = \left( \frac{A_1}{A_2} - 1 \right)^2 \frac{v_1^2}{2g} \quad (2.22)$$

$$\text{Hydraulic jump (rect.)} \quad \Delta H_{HJ} = \frac{d_1^2}{4d_2} \left( \frac{d_2}{d_1} - 1 \right)^3 \quad (2.23)$$

where  $A$  and  $d$  are the cross-sectional duct area and channel water depth. Subscripts 1 and 2 refer to locations just up- and downstream of the sudden expansion. Derivation of the head loss equation for a hydraulic jump in a downward sloping pipe, which fills the pipe cross sectional area, yields a Borda-Carnot head loss with a correction term for the free surface

$$\frac{\Delta H_{HJ}}{E_{1,kin}} = \left( \frac{A_1}{A_D} - 1 \right)^2 - \frac{\cos \theta}{E_{1,kin}} \left\{ \begin{array}{l} \frac{R - y_1}{2} + \frac{R}{\pi} \left( \frac{y_1}{R} - 1 \right) \arcsin \left( \frac{y_1}{R} - 1 \right) + \\ + \frac{R}{3\pi} \left[ \left( \frac{y_1}{R} \right)^2 - \frac{2y_1}{R} + 3 \right] \left( \frac{2y_1}{R} - \left( \frac{y_1}{R} \right)^2 \right)^{0.5} \end{array} \right\} \quad (2.24)$$

where  $E_{1,kin}$  is the kinetic energy upstream of the hydraulic jump. If the elongated air pocket is long enough, the water depth will reach normal depth ( $y_1 = y_n$ ). The free surface correction term is less than 10% of the Borda-Carnot term, if the upstream water depth  $y_1 < 0.75R$ .

The a priori deceleration length is  $6D$  for any deceleration loss in a pipe geometry (bend, valve, etc.); see e.g. standards for control valve capacity measurements (ANSI/ISA-75.02, 1996). The deceleration length of a hydraulic jump can be assessed more accurately, but it is around  $6d_2$  over a wide range of inflow Froude numbers (Hager, 1993). Consequently a deceleration length  $L = 6d_2$  seems a widely applicable deceleration length. Now, the eddy viscosity and diffusivity can be assessed for local losses. Equation (2.22) to (2.24) neglect

the influence of skin friction. It is desirable to include the effect of skin friction and fully developed inflow conditions on the hydraulic jump properties. Since normal depth is reached in about  $9D$  in downward pipe slopes between  $5^\circ$  and  $30^\circ$  (Lubbers, 2007), the inflow to the hydraulic jump is generally fully developed, which does affect the total head loss and the turbulent diffusion coefficient. If the air transport would be dominated by turbulence, generated in the hydraulic jump, the following turbulent bubble diffusion coefficient  $\varepsilon_y$  would affect the air bubble concentration profiles and air transport rate. This parameter follows from a combination of equations (2.21) and (2.24).

$$\varepsilon_y \sim \left( g y_n^3 \Delta H_{HJ} / 6D \right)^{1/2} \quad (2.25)$$

## 2.4 Air transport by surface entrainment

Although surface entrainment has not been observed by any of the investigators on air transport phenomena in downward sloping pipes, the air transport may be significantly enhanced by surface entrainment. If the water Reynolds number and pipe diameter are sufficiently large. Furthermore, surface entrainment was not observed by the author of this thesis in any of the experiments in the transparent facilities.

Surface entrainment is triggered by the destabilising momentum of surface turbulence, exceeding the stabilising forces due to gravity and surface tension (Brocchini and Peregrine, 2001). Therefore, a necessary condition for surface entrainment is that the boundary layer must have developed up to the water surface. Surface entrainment is initiated by water drops that are ejected from the surface or by air bubbles that are enclosed in the turbulent water film. Air entrainment by water drops falling back onto the water film requires water velocities exceeding 10 m/s (Rein, 1998). Air entrainment by air bubbles that are enclosed in the turbulent water film requires smaller velocities (Rein, 1998). Several theoretical criteria for the initiation of surface entrainment have been proposed (Brocchini and Peregrine, 2001; Chanson, 2009; Davies, 1972), but these criteria have limited practical value for two reasons. First, the criteria depend on the bubble diameter, which would have to be known a priori. Second, the criteria focus on the entrainment of an individual bubble rather than on the start of a sustained air-water flow. More recently, Chanson (2009) has emphasised the importance of scale effects in air-water flows.

The inception of self-aerating free-surface flows has been investigated experimentally by a.o. Volkart (1982) and Wood (1983; Wood, 1991). Volkart derived an experimental Boussinesq-criterion  $B$  for the start of surface entrainment in circular tubes, provided that

the turbulent boundary layer has reached the water surface; this criterion is based on the water film velocity  $v_w$  and hydraulic radius of the water film  $R_h$ .

$$B = v_w / \sqrt{gR_h} > 6 \quad (2.26)$$

This conditions seems strange, when applied to a uniform flow condition. For uniform flow, the condition reduces to a relation between pipe angle  $\theta$  and friction factor  $\lambda$  (based on Darcy Weisbach), predicting surface entrainment inception for sufficiently smooth pipes at a given pipe inclination.

$$\sin \theta > 4.5 \cdot \lambda \quad (2.27)$$

Chanson (1997) re-analysed Volkart's data and found a power law coefficient  $n \approx 6$ , which would correspond to a relatively large pipe friction factor  $\lambda = 0.03$ .

Wood (1991) defined a generic length scale  $d_{cs}$  for accelerating flows on spillways and found the following relation for the distance  $x$  to the inception point for self-aeration:

$$d_{cs} = \left( q^2 / [g \cdot \sin \theta] \right)^{1/3} \quad (2.28)$$

$$x = 13.5 \cdot d_{cs} (\sin \theta)^{0.08} \left( \frac{d_{cs}}{k_n} \right)^{0.069} \quad (2.29)$$

where  $\theta$  and  $k_n$  are the spillway angle and wall roughness.

This equation was calibrated on prototype measurements, but a minimum Reynolds number for the validity of equation (2.29) was not provided.

#### 2.4.1 Discussion on air transport by surface aeration

From a theoretical point of view, one would expect that self-sustaining surface aeration occurs, if a turbulent velocity at the free surface exceeds a certain function of the Froude number and Weber number to account for the stabilising effects of gravity and surface tension.

$$\overline{v'^2} > f(\text{Fr}, \text{We}) \quad (2.30)$$

Such a criterion for the inception of self-sustaining surface aeration has not been found in literature.

The inception criteria from Volkart, eq. (2.26), and Wood, eq. (2.28), would predict surface aeration for most flow conditions in facility 4 with a 40 m long, 10° downward inclined pipe of 192 mm internal diameter; further details of the experimental facilities are provided

in Table 3.1 in chapter 3. However, surface aeration was not observed in any flow condition in this facility. It is noted that Volkart's setup, including the 240 mm pipe at 11°, was very similar to facilities 4 and 6. A significant difference is that Volkart's facility was constructed from PVC sections of 5 m length and Perspex sections of 1 m length. Each PVC section was combined with a transparent section, which may have caused capillary waves at the pipe joints and may have triggered self-sustaining surface aeration. It is concluded that self-sustaining surface aeration in partially filled pipe flow may enhance the air transport at sufficiently large Reynolds numbers, but the conditions for the inception of surface entrainment are not known yet.

## 2.5 Air transport by dissolving into the water phase

The last physical mechanism that transports air to the bottom of a downward sloping section is the dissolving of air into the water phase. The analysis should be performed per species in the gas mixture. The concentration of a gas species at the gas-liquid interface ( $C(0,t)$ ) is supposed to be equal to the saturation concentration. The saturation concentration is defined by Henry's law (2.31):

$$C_{sX} = k_{HX} m_{gX} p \quad (2.31)$$

where

$C_{sX}$	[mol m <sup>-3</sup> ]	saturation concentration of species X at equilibrium
$k_{HX}$	[mol m <sup>-3</sup> bar <sup>-1</sup> ]	Henry's law constant for species X (see Table 2.2)
$m_{gX}$	[-]	molar fraction of species X
$p$	[bar]	total pressure in gas phase

Table 2.2: Henry's constants for typical gases in wastewater at 15°C.

Species	$k_H$ mol m <sup>-3</sup> bar <sup>-1</sup>
O <sub>2</sub>	1.3 10 <sup>-3</sup>
N <sub>2</sub>	6.5 10 <sup>-4</sup>
CO <sub>2</sub>	3.4 10 <sup>-2</sup>
NH <sub>3</sub>	1.0 10 <sup>+1</sup>
CH <sub>4</sub>	1.4 10 <sup>-3</sup>
H <sub>2</sub> S	1.0 10 <sup>-1</sup>

The air-water gas transfer in hydraulic jumps is modelled as a bulk process with an exponential evolution towards the saturation concentration (Chanson, 1995; Chanson, 2004):

$$\frac{C_{sX} - C_X(t)}{C_{sX} - C_X(0)} = \exp\{-K_X \cdot a \cdot t\} \quad (2.32)$$

where

$C_X(t)$  [mol m<sup>-3</sup>] Dissolved concentration of species X at time t

$K_X$  [m s<sup>-1</sup>] Mass transfer coefficient of species X

$a$  [m<sup>2</sup> m<sup>-3</sup>] Surface area of air bubbles per unit volume

Chanson (2004) has proposed and verified representative functions of the residence time t and the surface area per unit volume in partially developed hydraulic jumps. A similar approach could be applied to hydraulic jumps in closed conduits.

## 2.6 Research questions

Lubbers (2007) made a number of recommendations for further research including:

- Quantification of the influence of pipe diameter and length of the inclined section on the air transport,
- the influence of the water quality on the air transport and
- improvement of the air transport model.

The main R&D question, addressed in the PhD thesis is the development and validation of a total air transport model by flowing water, including the influence of pipe angle, length of downward sloping section, pipe diameter, surface tension, absolute pressure and viscosity. First, the recent experimental data on air-water flow are presented and the influence of a number of parameters is discussed (chapter 3). Secondly, an energy balance and a momentum balance are developed (chapter 4). The new air transport model is derived from the momentum balance and calibrated against available experimental data (chapter 5). The air transport model is particularly useful in practice, if the presence of air pockets can be detected before the air pockets create an excessive extra head loss. Such an air pocket detection method is developed (chapter 6). This detection method aims at predicting the air pocket location and volume. The practical implications are illustrated in two applications from pressurised wastewater mains (chapter 7).



## 3 Experiments

This chapter is extracted from a paper published in International Journal of Multiphase Flow (Pothof and Clemens, 2010a).

<http://dx.doi.org/10.1016/j.ijmultiphaseflow.2010.10.006>

### 3.1 Dimensional analysis

Air may be transported by flowing water through a downward sloping pipe by a number of mechanisms as discussed in chapter 2:

- 1 dispersed bubbles, if the water flow number is very large;
- 2 plugs moving along the pipe soffit;
- 3 bubbles entrained in hydraulic jumps while larger pockets move upstream;
- 4 an air-water mixture by surface entrainment, if the turbulence is sufficient for sustained surface entrainment, and
- 5 dissolved air in the water phase.

The bottom line is that the transport of air pockets, plugs and bubbles is determined by drag and pressure forces due to gravity and wall friction. The shape of the air bubbles in relation to the pipe diameter is influenced by the surface tension and contact angle. Furthermore, if the air-water contact area is large, a significant fraction of the air may dissolve into the water phase. The following parameter groups influence the air transport by flowing water:

- 1 Fluid properties: densities  $\rho_g$ ,  $\rho_w$ , kinematic viscosities  $\nu_g$ ,  $\nu_w$ , surface tension  $\sigma$ , contact angle  $\theta_c$ .
- 2 System parameters: length of downward sloping reach  $L$ , pipe angle  $\theta$ , pipe diameter  $D$ , wall roughness  $k_n$ .
- 3 Boundary conditions: superficial inflow velocities  $v_{sg}$ ,  $v_{sw}$ , gravitational acceleration  $g$ , absolute pressure  $p$ , dissolved gas species concentration  $c$ , Henry's constant  $k_H$ , molar fraction of gas species  $m$ , saturation concentration of gas species  $c_s (=k_H \cdot m \cdot p)$  water turbulence  $K$ , bubble diameter  $d$ , gas pocket head loss  $\Delta H_g$ .

The water turbulence and bubble diameter fully depend on other variables and introduce no new independent variables. The remaining 19 parameters, mentioned earlier in this paragraph, are all derived from four primary units (mass, length, time and molar



concentration), so that four parameters can be selected to determine the non-dimensional parameter groups for the modelling of air discharge. The selected parameters are water density  $\rho_w$ , water velocity  $v_{sw}$ , pipe diameter  $D$  and saturation concentration  $C_s$ , yielding the following functional relation for the superficial air velocity.

$$\frac{v_{sg}}{v_{sw}} = f \left( \frac{\rho_g}{\rho_w}, \frac{v_g}{v_{sw}D}, \frac{v_w}{v_{sw}D}, \frac{\sigma}{\rho_w v_{sw}^2 D}, \cos \theta_c, \sin \theta, \frac{L}{D}, \frac{k_n}{D}, \frac{gD}{v_{sw}^2}, \frac{p}{\rho_w v_w^2}, \frac{C}{k_H m \cdot p}, \frac{K}{v_{sw}^2}, \frac{d}{D}, \frac{\Delta H_g}{D} \right) \quad (3.1)$$

The influence of the air Reynolds number is considered negligible, because the air is driven by the water flow and the motion of air inside the air bubbles is assumed to be of limited importance. A possible influence of the contact angle is irrelevant for wastewater applications, because the contact angle is  $90^\circ \pm 3^\circ$  for the most popular pipe materials in inverted siphons (PE and PVC) and for the pipe materials in the lab facilities (PMMA and transparent PVC). Therefore, the contact angle may be eliminated from the functional relationship. It is more convenient to scale the gas pocket head loss to the elevation difference  $L \cdot \sin \theta$ , which is a combination of other parameters. Since the pipe Froude parameter or Flow number  $v_{sw}/(gD)^{1/2}$  is one of the dependent variables, substitutions may be carried out. Substitution of the Flow number in the pipe Weber parameter ( $We \equiv \rho_w v_{sw}^2 D / \sigma$ ) yields the Eötvös number ( $Eo \equiv \rho_w g D^2 / \sigma$ ), which is independent of the water velocity. However, the Eötvös number is a ratio of gravity to surface tension forces which is considered relevant for air plug transport. The Weber number is a ratio of inertia to surface tension forces and considered essential in the blow back flow regime with multiple hydraulic jumps. Furthermore, air transport by dissolving into the water phase may play a role in the blow-back flow regime, due to the large interfacial area in the hydraulic jumps, but this mass transfer is negligible in the plug flow regime. It is concluded that the dimensionless functional relation (3.1) can be rephrased more specifically for the blow-back and plug flow regimes, yielding:

$$\text{Blow-back} \quad F_g = \frac{v_{sg}}{\sqrt{gD}} = f \left( \frac{\rho_g}{\rho_w}, Re_D, We_D, \sin \theta, \frac{L}{D}, \frac{k_n}{D}, F_w, \frac{p}{\rho_w v_{sw}^2}, \frac{c}{k_H m \cdot p}, \frac{\Delta H_g}{L \sin \theta} \right) \quad (3.2)$$

$$\text{Plug} \quad F_g = f \left( \frac{\rho_g}{\rho_w}, Re_D, Eo_D, \sin \theta, \frac{L}{D}, \frac{k_n}{D}, F_w, \frac{\Delta H_g}{L \sin \theta} \right) \quad (3.3)$$

Even the simplified functional expressions show the complexity of air-water flows in inclined pipes. True dynamic similarity is obtained if all dimensionless parameters are identical at two different scales (e.g. model and prototype). True dynamic similarity cannot be achieved in air-water flows in model and prototype, because the Froude-scaling implies that the Reynolds-, Weber- and Eötvös-scaling cannot be respected. These dimensionless numbers remain functions of the pipe diameter:

$$\frac{\text{Re}_{D_1}}{\text{Re}_{D_2}} = \left(\frac{D_1}{D_2}\right)^{3/2}, \quad \frac{\text{Eo}_{D_1}}{\text{Eo}_{D_2}} = \frac{\text{We}_{D_1}}{\text{We}_{D_2}} = \left(\frac{D_1}{D_2}\right)^2 \quad (3.4)$$

It remains to be verified whether these effects diminish at sufficiently large pipe diameters.

### 3.2 Experimental facilities and instrumentation

Co-current downward flow experiments were conducted in seven similar facilities covering a wide range of pipe diameters, slope angles and length of sloping reach as outlined in Table 3.1; the table includes identifiers 1 to 7 for referencing purposes. The dynamic similarity is incomplete. The facility scaling is based on the flow number, because gravity driven flow phenomena dominate the air-water flow in all flow regimes. The possible influence of Reynolds, Weber and Eötvös number will be discussed in chapter 5.

All facilities, except for facility 4, were set-up in the Hydraulics Laboratory of Deltares (formerly Delft Hydraulics) in Delft, Netherlands. Facility 4 was erected at the wastewater treatment plant in Hoek van Holland in order to perform experiments with raw wastewater and with surfactant-added water in addition to the experiments with clean water. A definition sketch for the head loss measurements in these facilities is shown in Figure 3.1.

The experimental data from facilities 1, 3 and 4 were obtained under the author's responsibility. The data from the other facilities were obtained under Lubbers' responsibility (Lubbers, 2007).

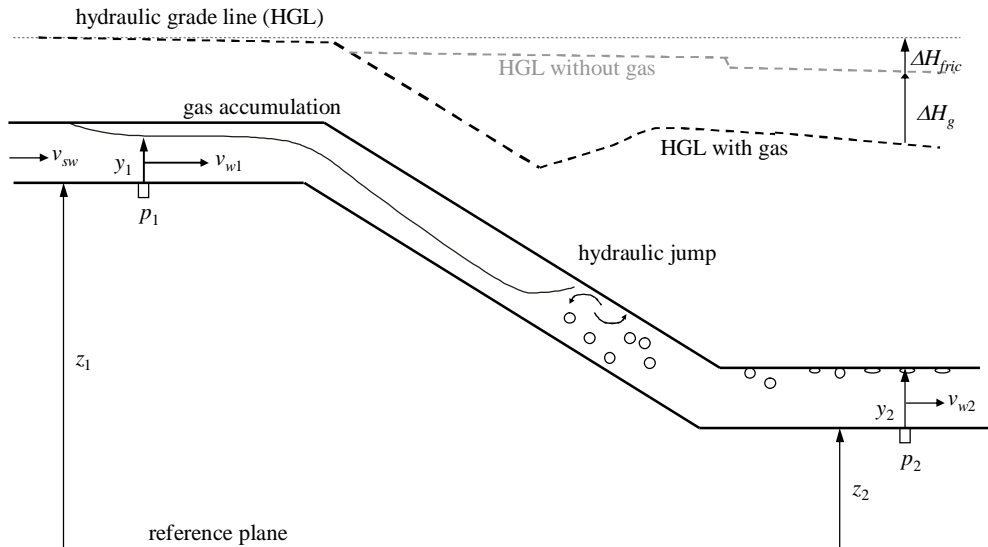


Figure 3.1: Definition sketch for gas pocket head loss measurements in experimental facilities

Table 3.1: Overview of experimental facilities. Table fields show slope length ( $L/D$ ) and the number of air-water flow combinations, i.e. 30/77 means  $L/D = 30$  and the number of air-water discharge combinations is 77. Data in grey-marked cells were obtained by Lubbers (2007).

ID	Pipe Diameter (m)	Angle(°)	5	10	12.5	20	30	90
1	0.080				30 / 77 <sup>#)</sup>			
2	0.110			27 / 78				
3	0.150			30 / 105 <sup>#)</sup>				
4	0.192			209 / 130 <sup>*)</sup>				
5	0.220		30 / 90 <sup>#)</sup>	30 / 95		30 / 51	30 / 83	10 / 98
6	0.220			21 / 61 <sup>#)</sup>		57 / 55		
7	0.500			25 / 23 <sup>#)</sup>				

<sup>\*)</sup> 65 Combinations with clean water were measured, 27 with surfactant added water and 38 with raw wastewater.

<sup>#)</sup> Upstream pressure tapping in horizontal section. Otherwise: upstream pressure tapping in the rising pipe (Figure 3.3)

The common components of the facilities are presented in Figure 3.2 and Figure 3.3. All facilities include a rising pipe, an upstream horizontal section with a length-diameter ratio  $L_u/D > 10$ , a mitre bend into the downward slope, a second mitre bend to a downstream horizontal section, followed by horizontal or rising pipework back to the reservoir with a separation function. This lay-out guarantees that none of the injected air can escape in the upstream direction. The pipe material of the two horizontal sections and the downward slope was transparent (PMMA or transparent PVC), except for the 500 mm facility, which was entirely constructed in steel. The experiments in lab facility 5 had identical lengths of the inclined section ( $L/D = 30$ ) and thus made the determination of the influence of the pipe angle ( $5^\circ \leq \theta \leq 30^\circ$ ) possible. The experiments at  $\theta = 10^\circ$  and very similar lengths ( $25 \leq L/D \leq 30$ ) were analysed to determine the diameter influence and thus the Reynolds and Eötvös influence. Facility 1 was accidentally positioned at  $\theta = 12.5^\circ$  instead of  $\theta = 10^\circ$ , but the results in facility 5 and the theoretical developments, detailed in of chapter 4, suggest that the differences between  $\theta = 10^\circ$  and  $\theta = 12.5^\circ$  are less than 1%. The results from facilities 4, 5 and 6 allow for the assessment of the influence of the length of the inclined section.

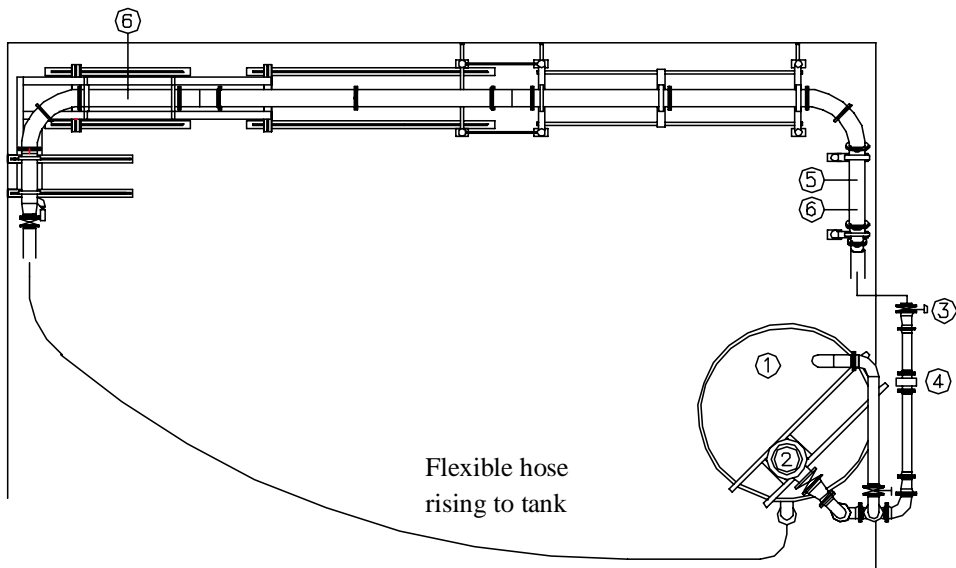


Figure 3.2: Top view of facility 5: 1) reservoir, 2) pump, 3) flow control valve, 4) EMF flow meter, 5) air injection, 6) up- and downstream pressure sensors.

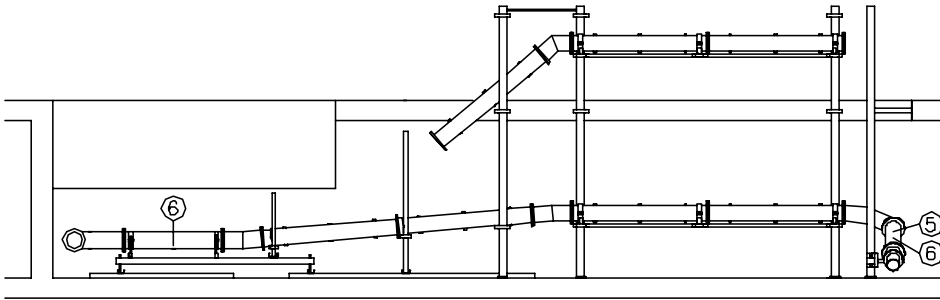


Figure 3.3: Side view of facility 5 showing the feasible range of downward pipe angles and the locations of air injection (5) and up- and downstream pressure sensors (6).

Air was injected either in the upstream horizontal section or just upstream of the horizontal section. The air mass flow rate  $\dot{m}_a$  was measured by a thermal air mass flow meter (Bronkhorst High-Tech); the measuring principle is based on a temperature drift measurement in an accurately split by-pass flow. The mass flow rate was controlled to a pre-set volumetric flow rate  $Q_a$ , using the water temperature  $T$  and pressure at the location of the upstream absolute pressure transducer. The upstream absolute pressure  $p_1$  was measured in the riser pipe upstream of the horizontal section. During the initial measurements, the upstream pressure transducer was installed in the bottom of the horizontal pipe where stratified flow conditions would occur when the liquid flow number  $F_w < 0.58$  (Benjamin, 1968; Montes, 1997). In those circumstances, surface waves and the air-water interface level affect the gas pocket head loss; this influence will be quantified in paragraph 3.3. The facilities with the upstream pressure tapping in the horizontal section are marked with a <sup>#</sup> in Table 3.1. The downstream pressure tapping was located in the downstream horizontal section. This tapping was connected to a second absolute pressure transmitter  $p_2$  or a differential pressure transmitter  $\Delta p$ . The differential pressure transmitters were used in the smaller facilities (1 – 3) and in facility 4 to achieve optimum accuracy in the measured gas pocket head loss. The high pressure side of the differential pressure transmitter was connected to the upstream pressure tapping. The absolute pressures were measured with Druck PDCR4010 instruments, the differential pressure was measured with Rosemount transmitters.

The water flow rate  $Q_w$  was measured with an Electro-Magnetic Flow meter (EMF), positioned in an upstream pipe segment without air. A flow control valve controlled the water flow rate to a pre-set value. Table 3.2 summarises the instrument specifications.

These signals ( $\dot{m}_a$ ,  $T$ ,  $Q_w$ ,  $p_1$ ,  $p_2$  and/or  $\Delta p$ ) were sampled with 100 Hz for at least 30 s to capture turbulent fluctuations and determine the 30 s average values.

Table 3.2: Instrumentation and experimental facilities in which they were used

Instrument	Brand, type	Range	Instrument accuracy (%FS)
Water flow meters			
Fac. 1	Foxboro, 2800, Ø0.125 m	0 – 0.01 m <sup>3</sup> /s	< 0.25
Fac. 2 - 6	E+H, Promag50, Ø 0.125 m	0 – 0.1 m <sup>3</sup> /s	< 0.25
Fac. 7	Foxboro, EM, Ø 0.500 m	0 – 2.0 m <sup>3</sup> /s	< 0.25
Air mass flow meters			
Fac. 1 - 4	Bronkhorst High-Tech, F20-AC	0 – 50 nl/min	< 1
Fac. 2 - 7	Bronkhorst High-Tech, F201-AC	0 – 3 nl/min	< 0.25
Absolute pressure sensors (all facilities)	Druck PDCR4010	0 – 5 bara	< 0.1
$\Delta P$ sensors			
Fac. 1, 2 and 3	Rosemount 3051 CD	0 – 0.06 bar	< 0.25
Fac. 4	Rosemount 1151 DP	0 – 1 bar	< 0.5
Temperature sensor (all facilities)	RS-PT100	0 – 50 °C	< 1
Surface tension			
Fac. 4	Kibron AquaPi	0.01 – 0.1 N/m	< 0.1

The surface tension in facility 4 was adjusted by adding non-foaming surfactants to the clean water tank, so that surface tension values between 0.04 and 0.07 N/m were obtained. The surface tension was measured during the experiments with reduced surface tension and wastewater as static surface tension according to the Langmuir principle with a Kibron AquaPi tensiometer. The samples for the surface tension measurements were extracted at 15 minute intervals and analysed immediately.

### 3.3 Test procedure

The gas pocket head loss was determined as follows. At a given air and water discharge, the system gradually evolved towards a new equilibrium state. This process was monitored by visual observation and by monitoring the trend in the gas pocket head loss. As soon as the

equilibrium state was reached, at least three measurements of 30 seconds at a frequency of 100 Hz were performed.

Since the stabilization process in facility 4 could take up to eight hours, a more strict stabilization criterion was applied. The stabilization criterion consisted of the following procedure:

Once the gas pocket head loss appeared stable, the 100 Hz measurements were collected at 5 minute intervals. If the 30s-average values of 7 consecutive measurements were within bandwidth of 5 mbar (5 cm head loss approximately), the system state was defined as stationary; Figure 3.4 shows an example of this stabilization process.

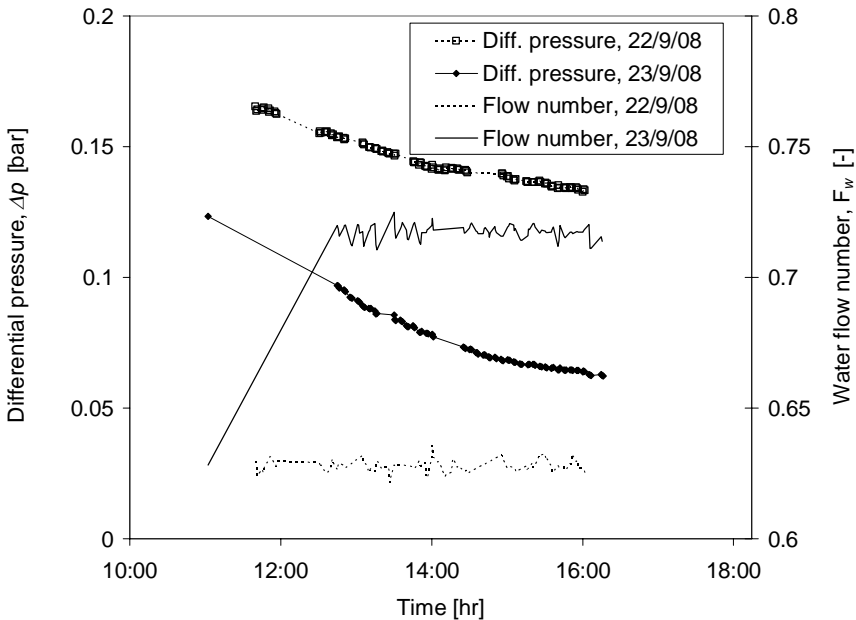


Figure 3.4: Examples of stabilisation process in facility 4 at  $F_g \cdot 1000 = 0.44$ .

The experimental facilities with upstream pressure transmitter  $p_1$  in the horizontal section, marked <sup>#)</sup> in Table 3.1, require a correction factor which is detailed hereafter. If air accumulates in a downward sloping reach, the air pocket head loss  $\Delta H_g$  approximately equals the aggregated height of the air pockets, which will be confirmed experimentally in chapter 5. The total energy conversion between the pressure tapplings in the experimental facilities, indicated with subscripts 1 and 2, includes losses  $\Delta H_{fric}$  due to wall friction and the mitre bends, energy losses due the air pocket  $\Delta H_g$  and energy conversions due to

differences in kinetic energy of the water film  $v_w^2/2g$ , hydrostatic pressure  $p/\rho_w g$  and elevation  $z$ . The frictional head loss  $\Delta H_{fric}$  refers to the situation without air. The air pocket head loss  $\Delta H_g$  represents all extra losses due to the presence of air in the downward sloping reach. A difference in kinetic energy occurs only if stratified flow occurs at one or both pressure tapings, typically at  $p_1$ .

$$\frac{p_1}{\rho_w g} + z_1 + \frac{v_{w,1}^2}{2g} = \frac{p_2}{\rho_w g} + z_2 + \frac{v_{w,2}^2}{2g} + \Delta H_{fric} + \Delta H_g \quad (3.5)$$

If  $p_1$  is located in the horizontal section and stratified flow occurs at a small water discharge, then the kinetic energy difference must be taken into account. Recognizing that the upstream water acceleration along the air bubble nose in the horizontal section is essentially frictionless, the upstream kinetic energy can be expressed as

$$\frac{v_{w,1}^2}{2g} + y_1 = \frac{v_{sw}^2}{2g} + D \quad (3.6)$$

where  $y_1$  is the local water depth at pressure tapping 1. The downstream velocity  $v_2$  practically equals the superficial water velocity  $v_{sw}$ , because the gas hold up at this location is negligible. Substitution of equation (3.6) in equation (3.5) and elimination of the superficial water velocity yields

$$\frac{p_1}{\rho_w g} + z_1 + D - y_1 = \frac{p_2}{\rho_w g} + z_2 + \Delta H_{fric} + \Delta H_g \quad (3.7)$$

The term  $D - y_1$  may contribute significantly to the total energy head loss of the gas pocket: for a typical water level  $y_1 = 0.5D$  or less, the term  $D - y_1$  represents at least 11% of the maximum gas pocket head loss in facility 7 and even 19% in facility 5 at the smallest slope of  $5^\circ$ . The term  $D - y_1$  automatically vanishes if the gas hold up is zero at the location 1. The upstream pressure transducers in the facilities, marked with #), were located at different positions in the horizontal section (Figure 3.5). Observations in the transparent facilities showed that the water level correction drops to zero at a flow number  $F_w = 0.63$ . These observations are consistent with literature on the cavity length of a free outflow from a horizontal pipe (Hager, 1999). The water level corrections  $D - y_1$  for the lower flow numbers were obtained from a channel flow computation for hydraulically smooth pipes (Figure 3.5).



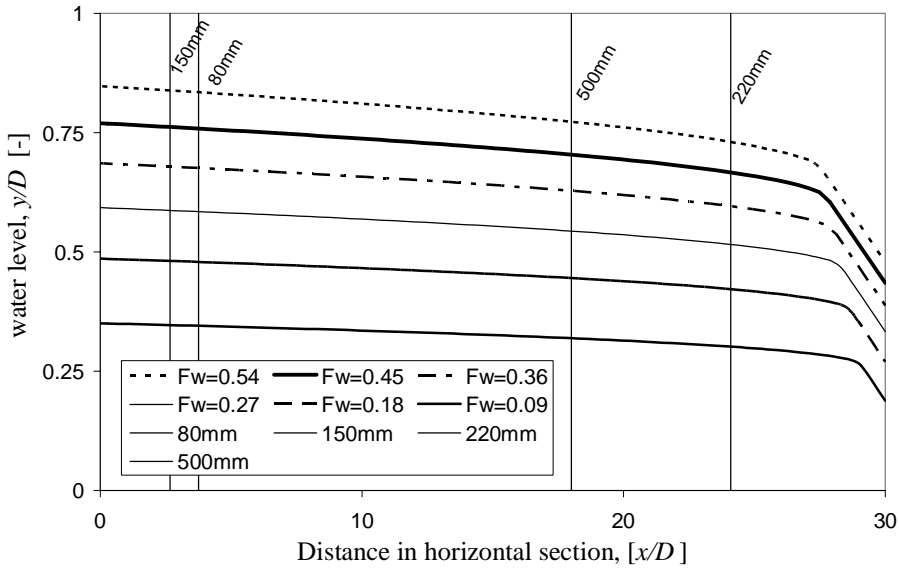


Figure 3.5: Water levels in horizontal section at applicable flow numbers; vertical lines and markers indicate position of  $p_1$  in the different facilities.

### 3.4 Uncertainty of results

The instrumentation has been selected in such a way that the process fluctuations dominate the total observed uncertainties. The uncertainty analysis focuses on the results in the water flow number range where the water level correction, eq. (3.7), can be neglected, because the important reduction in gas pocket head loss occurs at  $F_w > 0.6$ . In facilities 2, 4 and 5, the upstream pressure transducer was installed in the riser pipe, so that there is no water level correction, irrespective of the water flow number. In both cases equation (3.7) simplifies to

$$\Delta H_g = \frac{p_1 - p_2}{\rho_w g} + z_1 - z_2 - \Delta H_{fric} \quad (3.8)$$

Presuming that the individual measurements are considered mutually independent measurements, the accumulated standard deviation is calculated as

$$\sigma_{\Delta H_g}^2 = \frac{\sigma_{p_1}^2 + \sigma_{p_2}^2}{(\rho_w g)^2} + \sigma_{z_1}^2 + \sigma_{z_2}^2 + \sigma_f^2 \quad (3.9)$$

Uncertainty in the water density  $\rho_w$  is considered negligible. The individual terms in the accumulated standard deviation will be briefly discussed in the following paragraphs. The frictional head loss  $\Delta H_{fric}$  is measured (without air in the pipe) over the complete range of discharges using 30 s average values of data recorded at 100 Hz. The curve of 30 s average values is approximated by parabolic functions in the water velocity.

$$\Delta H_{fric} = c_1 \cdot v_w^2 + c_2 \cdot v_w + c_3 \quad (3.10)$$

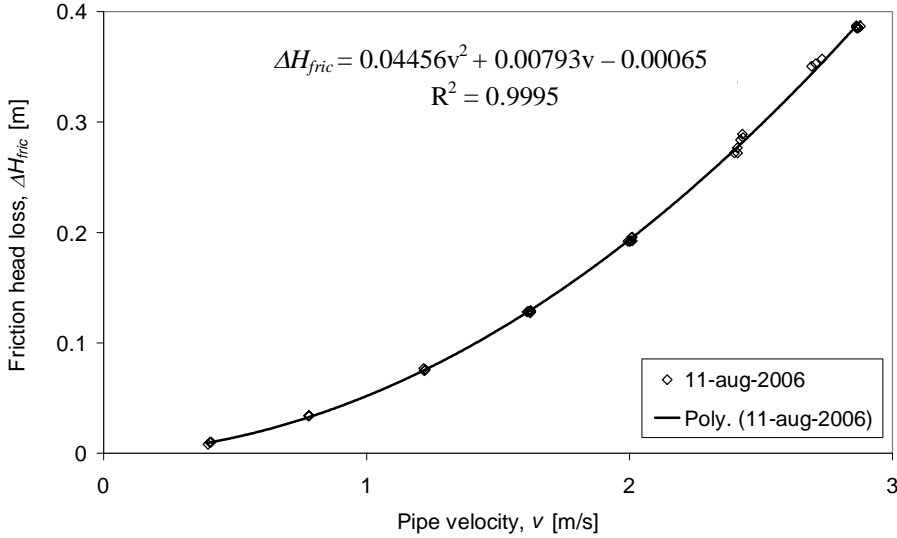


Figure 3.6: Example of friction head loss measurement in facility 7 ( $D = 0.5$  m)

The typical coefficient of determination ( $R^2$ ) in the parabolic function was  $R^2 = 0.999$ . Since the parabolic function will be used at any intermediate water discharge, a quadratic approximation of the friction head loss will be used. The variance of an arbitrary quadratic function with maximum  $\Delta H_{f,max}$  is computed as

$$Var(\Delta H_f) = E\left(\Delta H_f - \overline{\Delta H_f}\right)^2 = \frac{1}{Q_{max}} \int_0^{Q_{max}} \left(c_1 x^2 - \Delta H_{f,max}/3\right)^2 dx = \frac{4}{45} \Delta H_{f,max}^2 \quad (3.11)$$

Now equation (3.11) and the explained variance,  $R^2$ , can be combined to obtain the standard deviation of the remaining error in the parabolic approximation

$$\sigma_f^2 = (1 - R^2) Var(\Delta H_f) = (1 - R^2) \frac{4}{45} \Delta H_{f,max}^2 \quad (3.12)$$

The measurement of the elevation difference ( $z_1 - z_2$ ) may include a systematic error in the order of 0.5 cm; this error does not increase the random noise of the gas pocket head loss,

which implies that  $\sigma_{z_{1,2}} = 0$ . The elevation difference in facility 4 was more difficult to measure directly, because of the absence of a flat floor. Therefore, this elevation difference was cross-checked with hydrostatic pressure measurements, resulting in a maximum systematic error of at most 3 cm ( $< 0.5\%$  of the total elevation difference). The accumulated standard deviation in the gas pocket head loss  $\sigma_{\Delta H_g}$  is based on the standard deviation from two absolute pressure measurements  $\sigma_p$  or the differential pressure measurement  $\sigma_{\Delta p}$  and the standard deviation of the friction head loss  $\sigma_f$ . Since the coefficient of determination  $R^2$  is so large, the dominant term in the standard deviation of the gas pocket head loss is the standard deviation of the differential pressure measurement(s). One should realise that the standard deviations computed in this way characterise the uncertainty in the 100 Hz signal, thus including noise due to turbulence.

In order to compare the standard deviations from different facilities, the standard deviation is scaled by the elevation difference of the facility  $L \cdot \sin\theta$ . The procedure above yields uncertainty information on every gas pocket head loss datapoint. As an example, the average standard deviations per air-water flow combination in facility 5 with a pipe angle of  $10^\circ$  are plotted in Figure 3.7. Figure 3.7 shows a tendency with the largest uncertainties around  $F_w = 0.75$ , where the gas pocket head loss is approximately 50%. Furthermore, the uncertainty increases in the air discharge. The typical standard deviation in this facility is 5% of the elevation difference, which coincides with 0.35 m head loss.

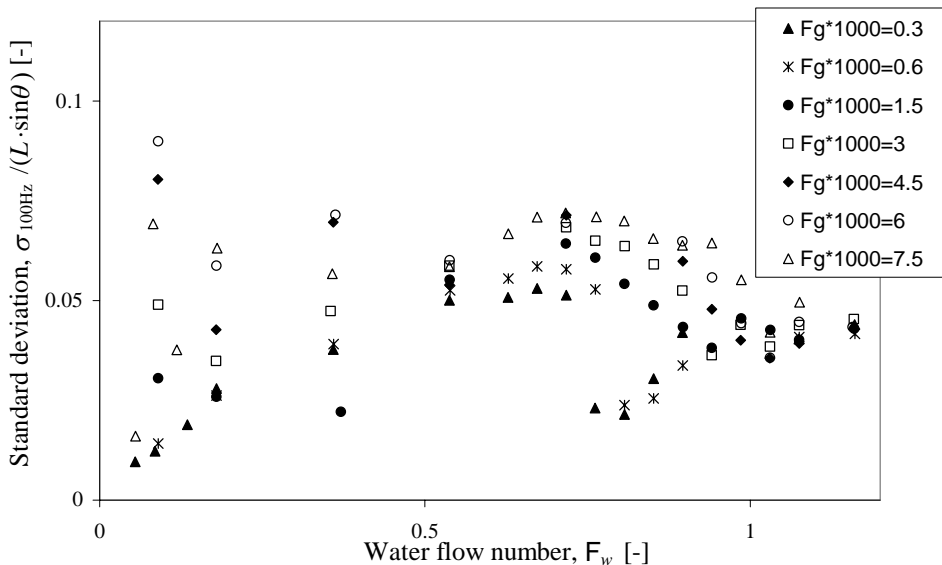


Figure 3.7: Standard deviation in 100 Hz gas pocket head loss data in facility 5 with pipe angle  $\theta = 10^\circ$ . Figure shows average standard deviations per air-water flow combination.

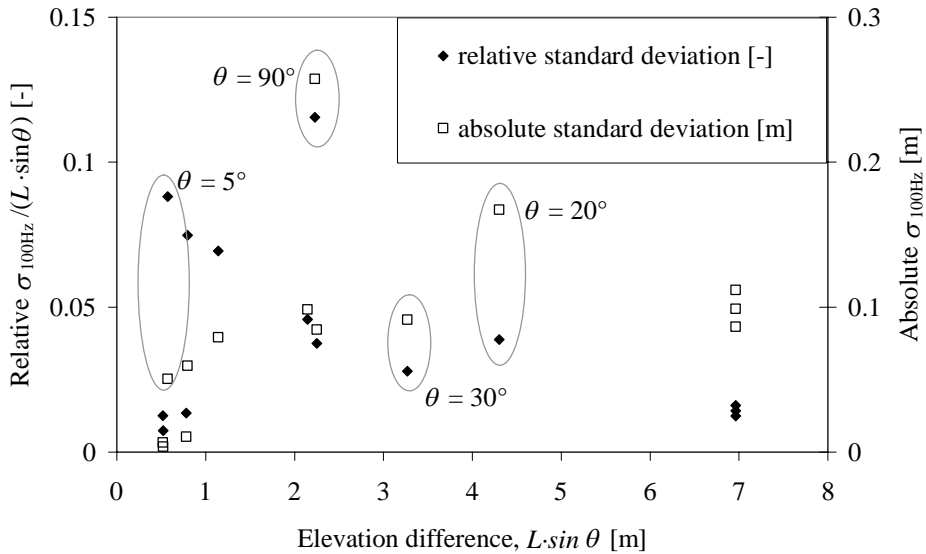


Figure 3.8: Relative and absolute standard deviations of the gas pocket head loss as a function of the elevation difference. Data points with pipe angles, other than  $\theta = 10^\circ$ , are indicated.

In order to obtain a single representative standard deviation per facility and pipe configuration, the 90-percentile value is used as the representative facility standard deviation. The 90-percentile values of the 100 Hz gas pocket head loss standard deviations (relative and absolute) are depicted in Figure 3.8. The 90-percentiles of the absolute standard deviations in the facilities with  $\theta = 10^\circ$  are typically around 0.1 m, independent of the length of the downward sloping reach. The absolute uncertainties in the facilities with pipe diameters  $D < 0.15$  m are considerably smaller (around 0.01 m). The largest random noise was measured in facilities 5 ( $\theta = 90^\circ$ ) and 6 ( $\theta = 20^\circ$  and  $L = 57D$ ).

The 100 Hz standard deviations provide insight in the short term uncertainty, but these standard deviations do not provide insight in the accuracy of the recorded 30s-average gas pocket head loss data. The standard deviation in the 30s-average values could be determined directly from the series of stabilised gas pocket head loss data. These 30s standard deviations are plotted in Figure 3.9, which again shows the 90-percentiles per system configuration. The 30s standard deviations in facility 4 are dominated by relatively slow process fluctuations. The relative standard deviations in the lab facilities are typically around 0.5% of the elevation difference. All relative standard deviations are smaller than 1% of the elevation difference. These values are too small to use error bars in the figures with experimental results on the gas pocket head loss data.

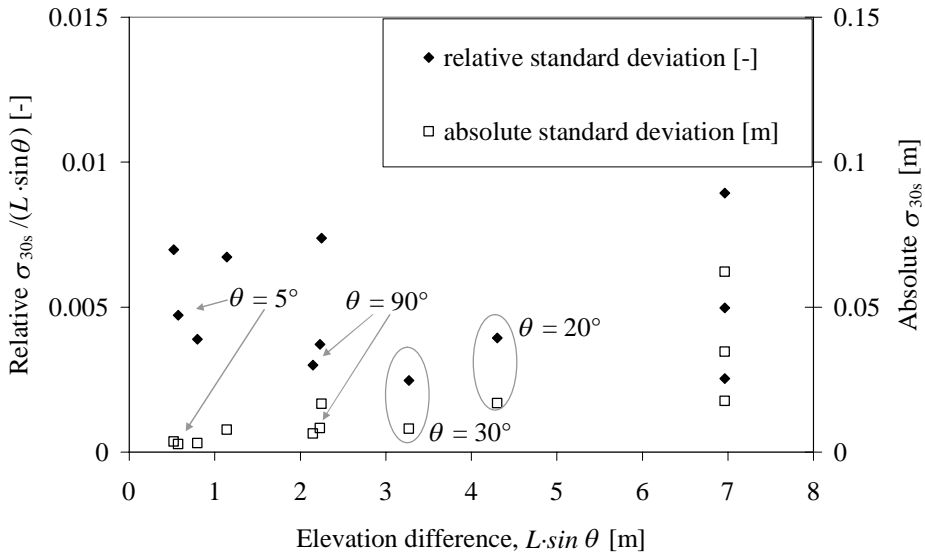


Figure 3.9: 90-Percentile values of gas pocket head loss standard deviations of the 30s average values.

### 3.5 Experimental results

#### 3.5.1 Observed flow regimes and gas pocket head loss

This section presents the observed flow regimes during co-current water-air experiments in facility 4 ( $D = 192$  mm,  $L/D = 209$ ,  $\theta = 10^\circ$ ), because the different flow regimes are most pronounced in the longest sloping section. The flow regimes 1, 2a, 2b, 3 and 4 occur consecutively at increasing water discharge. The flow regime labels, 1 to 4, are used in Table 3.3 and Figure 3.12b. Kalinske (1943) and Bliss (1942) identified qualitative descriptions of a blow-back flow regime, transitional flow regime and full gas transport flow regime. The observed flow regimes extend and further detail the available description from literature (Bliss, 1942):

1. Stratified flow in entire slope. A single gas pocket fills the entire slope, causing the maximum gas pocket head loss. The gas entraining hydraulic jump occurs in the downstream horizontal section. The transition to the blow-back flow regime depends on the gas flow number.
2. Blow-back flow regimes 2a and 2b. The gas pocket fills a part of the slope with a water film underneath. The downward sloping pipe contains one or more gas-entraining hydraulic jumps (Figure 3.10 and Figure 3.11); up to seven simultaneous jumps were observed in facility 4. The entrained gas bubbles rise to the pipe soffit, coalesce to larger bubbles and secondary gas pockets. These

secondary gas pockets have their own hydraulic jumps that pump the gas further downward. The larger bubbles and gas pockets blow back into the top gas pocket. The larger the water flow rate, the smaller the upward velocity of the secondary gas pockets. The gas pocket head loss decreases gradually at increasing water discharge (Figure 3.12a). Only a fraction of the entrained air reaches the bottom of the inclined section. The presence of a single air pocket and hydraulic jump is indicated by label 2a, the presence of multiple air pockets and hydraulic jumps by label 2b (Table 3.3 and Figure 3.12b). The experimental data suggest that the transition from flow regime 2a to 2b occurs around  $F_w = 0.53$ , independent of the gas discharge.

3. Plug flow regime. Stratified flow conditions and blow back phenomena do not occur anymore. A series of gas plugs slowly moves in downward direction along the pipe soffit. The water hardly entrains air from the air pockets, which means that the Froude number of the water film must be smaller than 2 ( $Fr < 2$ ). The gas pocket head loss has become marginal. The transition from flow regime 2 to 3 marks the dimensionless clearing velocity or required flow number  $F_c$  to keep elongated air pockets stationary, as investigated by other researchers (Escaramaia, 2007; Gandenberger, 1957; Kent, 1952; Wisner et al., 1975).
4. Dispersed bubble flow regime. All gas is transported in downward direction in dispersed bubbles and plugs. The gas pocket head loss is negligible.

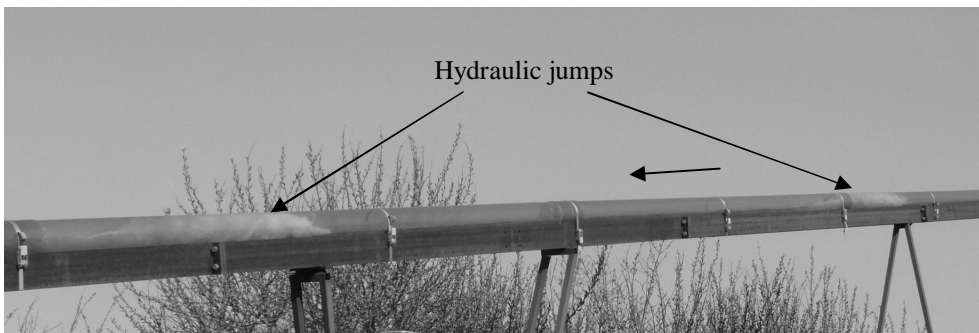


Figure 3.10: Subsequent hydraulic jumps in facility 4 ( $D = 192$  mm,  $L/D = 209$ ,  $\theta = 10^\circ$ ). Water is flowing from right to left

The observed flow regimes in the other facilities are similar, although the laboratory facilities were not long enough to clearly identify multiple gas pockets in the blow back flow regime. Surface entrainment phenomena were not observed over the range of downward slopes from  $5^\circ$  to  $30^\circ$ . Since the water phase was under-saturated at most pressure conditions in the downward slope, a certain fraction of the air dissolves into the water phase in the blow back flow regime; in this flow regime with gas entraining hydraulic

jumps the contact surface is large, which promotes air to dissolve into the water. The gas pocket head loss measurements are summarised in appendix B.

Table 3.3: Observed flow regimes in facility 4. The table lists the flow regime identifiers from section 3.5.1

$F_w$	0.09	0.18	0.27	0.36	0.45	0.54	0.63	0.72	0.81	0.9	0.98	1.07	1.16
$F_g * 1000$													
0.4	1	1	2a	2a	2a	2b	2b	2b	3	3	4	4	4
0.8	1	1	1	1	2a	2b	2b	2b	2b	3	3	4	4
2	1	1	1	1	2a	2b	2b	2b	2b	2b	3	3	4
4	1	1	1	1	2a	2b	2b	2b	2b	2b	3	3	3
6	1	1	1	1	2a	2b	2b	2b	2b	2b	3	3	3

Table 3.3 summarizes the observed flow regimes, using the identifiers, defined in paragraph 3.5.1. It is remarkable that multiple hydraulic jumps can only occur if the flow number is within the range  $0.53 \leq F_w \leq 1$ . Two new criteria for the occurrence of multiple air pockets in downward sloping pipes will be derived in chapter 4 from energy and momentum considerations. The validity of these criteria will be confirmed by these observations. The transition from the blow-back to the plug flow regime is marked by the absence of air entrainment into the hydraulic jumps. This transition has strong similarities with the plug-slug flow transition in horizontal pipes (Ruder and Hanratty, 1990).

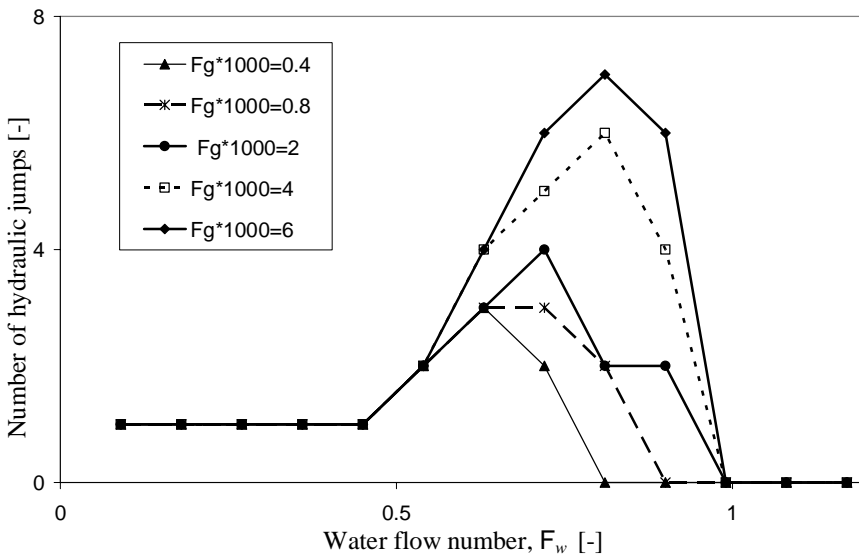


Figure 3.11: Observed number of hydraulic jumps in facility 4.

A more detailed investigation of camera images of the length of the mixing zones and subsequent air pockets at  $F_g = 0.002$  showed that the length of individual air pockets decreases along the slope. The gas pocket head loss is strongly correlated with the total dimensionless gas pocket length, as shown in Figure 3.13.

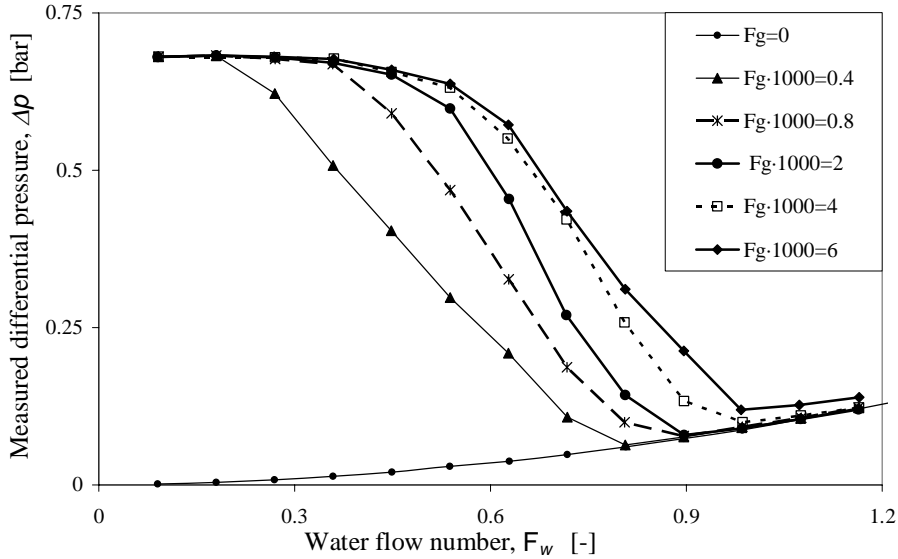


Figure 3.12a: Measured differential pressure in facility 4.

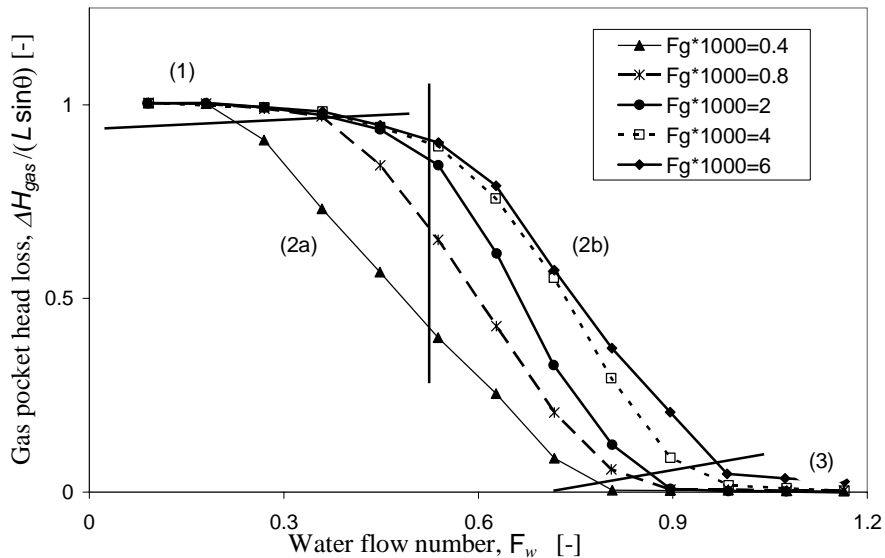


Figure 3.12b: Non-dimensional gas pocket head loss in facility 4, including flow regime labels.



The gas pocket head loss is slightly smaller than the total gas pocket length, because there is some pressure recovery in each hydraulic jump. The more subsequent hydraulic jumps, the larger the aggregated pressure recovery which is reflected in the difference between the gas pocket length and head loss.

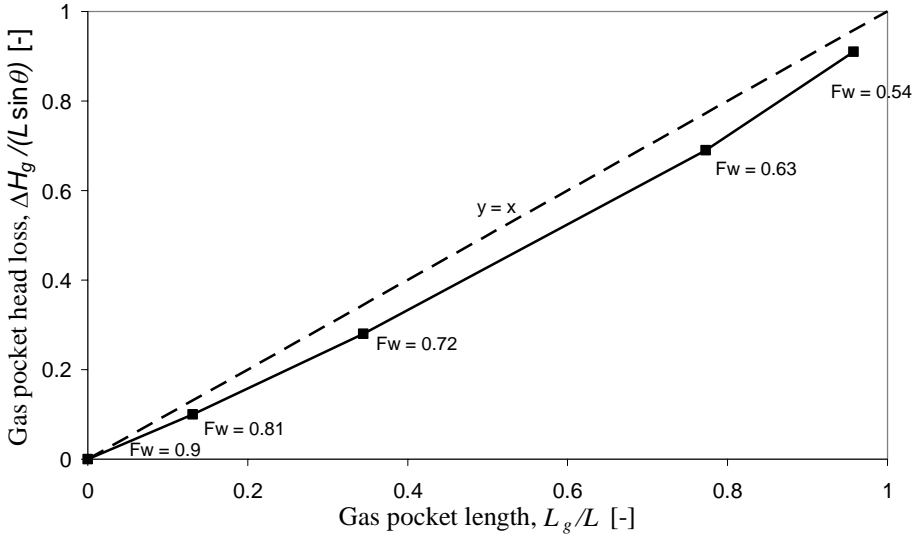


Figure 3.13: Gas pocket head loss versus total length of gas pockets at  $F_g = 0.002$ .

### 3.5.2 Maximum air transport without air pocket accumulation

Figure 3.14a and 3.14b show the clearing flow numbers from facility 5. Recent experimental data (Wickenhäuser and Kriewitz, 2009) at pipe angles  $\theta < 5^\circ$  and  $D = 0.484$  m has been included in Figure 3.14a (label VAW). The maximum clearing flow numbers occur at a downward slope angle between  $10^\circ$  and  $20^\circ$ . The smallest clearing flow numbers were measured in the vertical pipe, implying that the air transport capacity without air accumulation is the largest in a vertical pipe. Two qualitative physical arguments explain the enhanced air transport capacity in a vertical pipe. First, the pipe soffit is absent at  $90^\circ$ , so that entrained bubbles in the plunging jet at  $90^\circ$ , do not easily coalesce into large air pockets. Secondly, the entrained bubbles experience a relatively large drag force, because the frontal bubble area is relatively large in a vertical pipe. Therefore, the blow back flow regime was hardly observed in the vertical pipe (Lubbers, 2007). The clearing flow number in the vertical pipe at the smallest air discharge is  $F_c = 0.36$ , which is consistent with the drift flux model (eq. (2.9),  $v_b = c_0 v_{sm} + v_d = c_0 (v_{sw} + v_{sg}) + v_d$ )

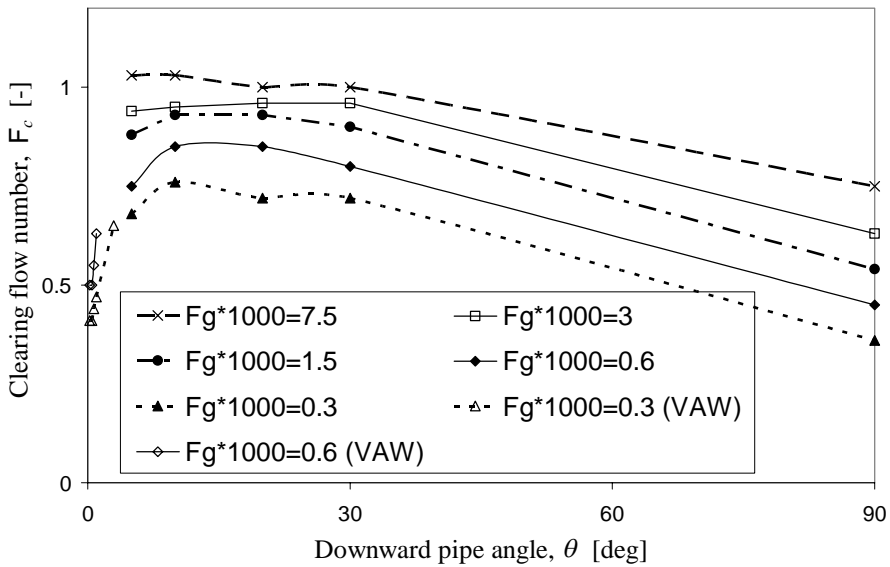


Figure 3.14a: Clearing flow number from facility 5 and Wickenhäuser (2009, Label VAW).

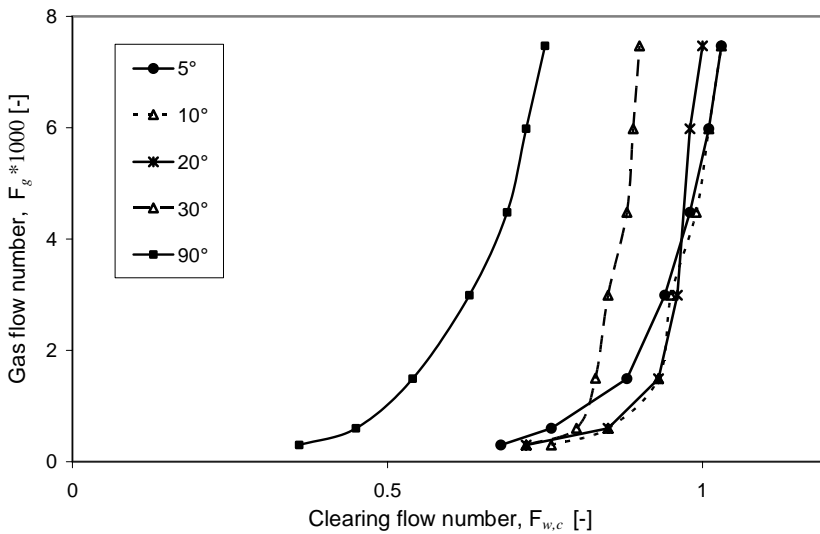


Figure 3.14b: Flow regime transition from blow back to plug flow regime.

Bendiksen (1984) has shown that the coefficient  $C_0$  equals 0.98 in downward sloping pipes up to  $\theta = 30^\circ$ . Assuming that the same  $C_0$  is applicable at a  $\theta = 90^\circ$  downward slope (i.e. a

vertical pipe), the clearing flow number  $F_c = 0.35 / 0.98 = 0.36$ . Figure 3.14b shows that the clearing flow number weakly depends on the gas discharge.

### 3.5.3 Influence of pipe diameter and sloping reach length

The influence of the pipe diameter on the gas pocket head loss at a given downward slope angle  $\theta = 10^\circ$  and length of the downward sloping reach  $L/D \approx 30$  is illustrated in Figure 3.15, showing that the influence of the pipe diameter on the clearing flow number diminishes above  $D = 150$  mm. A minimum diameter  $D > 200$  mm (or  $Eo > 5000$ ) is proposed for further experiments on the clearing velocity  $F_c$  or drift velocity  $F_d$ .

Figure 3.16 presents the influence of the length of the sloping reach on the gas pocket head loss. Figure 3.16 shows that the maximum dimensionless gas pocket head loss is independent of the length and that the gas pocket head loss becomes zero at  $F_w = 0.98$ , independent of the length of the sloping reach. It is thus concluded that the clearing flow number is independent of the length of the sloping reach, provided that  $L/D > 20$ . The gas pocket head loss drops more linearly in the shorter facilities.

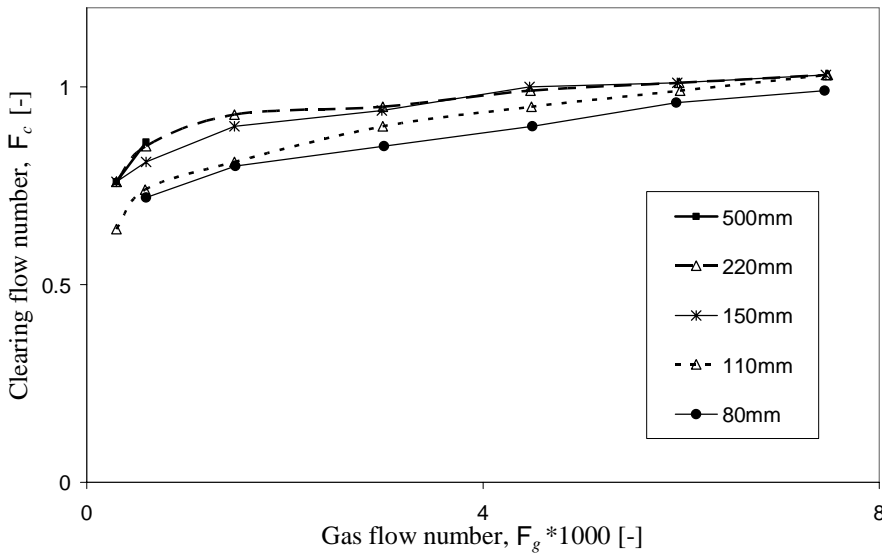


Figure 3.15: Clearing flow number in different lab facilities, marking the transition from flow regime 2b to 3 ( $\theta = 10^\circ$ ;  $L/D \approx 30$ ).

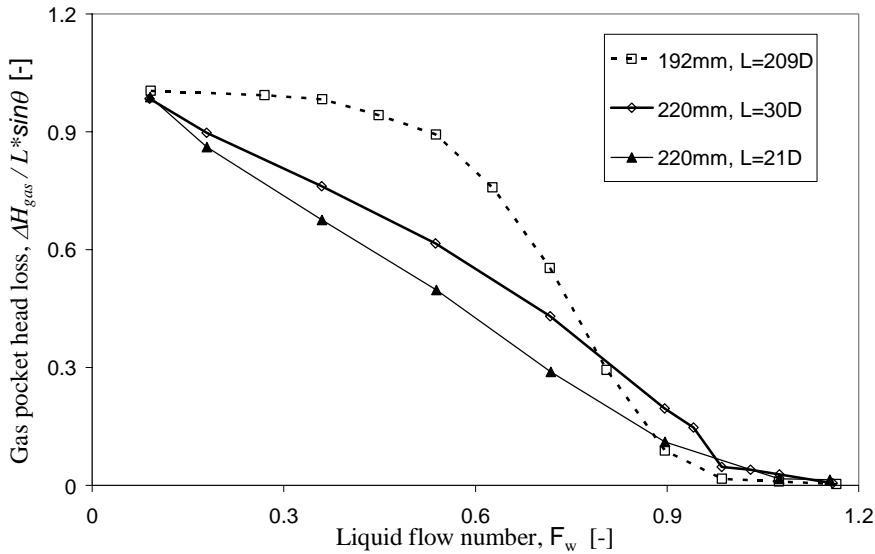


Figure 3.16: Influence of slope length on gas pocket head loss ( $\theta = 10^\circ$ ;  $F_g * 1000 = 4.5$ ).

### 3.5.4 Influence of surface tension

The surface tension may not affect the clearing velocity if  $Eo > 5000$ , but it clearly affects the gas pocket head loss in the blow back flow regime (Figure 3.17). Figure 3.18 plots the available gas pocket head loss data at two air discharge rates and variable surface tension from facility 4 as a function of the pipe Weber number  $We_D$ .

$$We_D = \rho v_{sw}^2 D / \sigma \quad (3.13)$$

These data are compared with the experimental points for clean water ( $\sigma = 0.072$  N/m). The experimental data in Figure 3.18 collapse to a single line in the blow back flow regime, showing that the pipe Weber number is a suitable scaling parameter for the gas pocket head loss in this flow regime. If the length scale in  $We_D$  were based on a typical bubble diameter in the turbulent hydraulic jump (Hinze, 1955), the data would not collapse to a single line. It is concluded from the Weber scaling in Figure 3.18 that the pipe velocity and pipe flow number should be multiplied with the ratio  $(\sigma / \sigma_w)^{1/2}$  to obtain identical results for the clearing velocity and gas pocket head loss, for fluid systems with another surface tension than air-water.

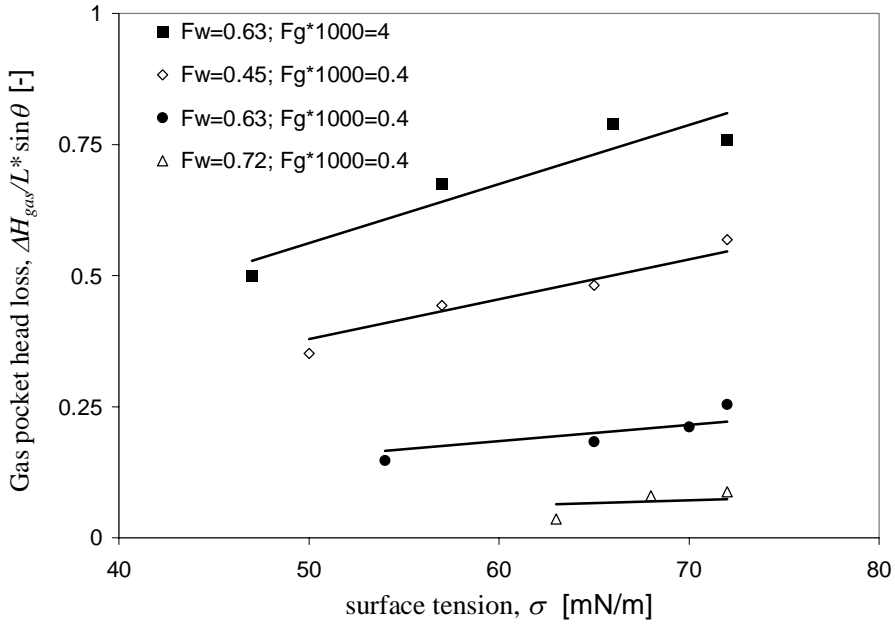


Figure 3.17: Influence of surface tension on gas pocket head loss in facility 4 ( $D = 0.192$  m,  $L/D = 209$ ,  $\theta = 10^\circ$ ).

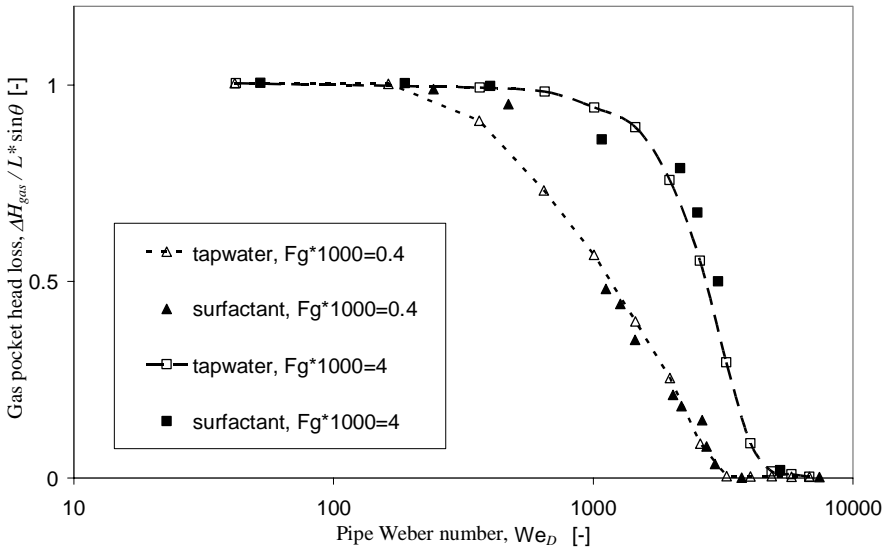


Figure 3.18: Gas pocket head loss as a function of the pipe Weber number.

### 3.5.5 Influence of absolute pressure

Figure 3.19 shows a reduction in the gas pocket head loss at increased downstream pressure. It is emphasized that the volumetric gas flow number at increased absolute pressure was kept constant. The large interface area in the hydraulic jump promotes air to dissolve into the water phase. This mode of air transport is more dominant at the lower gas flow numbers, as illustrated in Figure 3.19. Therefore, the saturation level of the water phase has an influence on the total air transport.

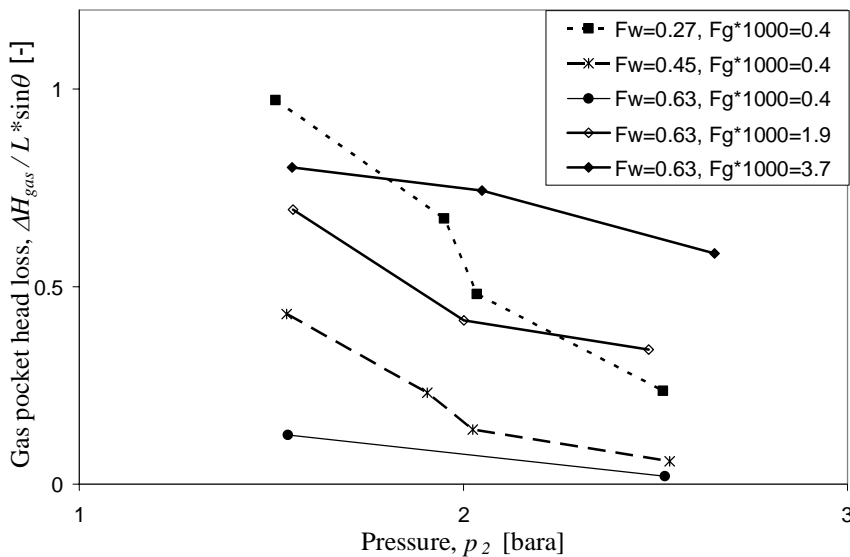


Figure 3.19: Gas pocket head loss at increased absolute pressure.

### 3.5.6 Influence of wastewater

It is anticipated that the different constituents in wastewater will influence the gas transport processes. Initial tests with the wastewater showed that the surface tension of dry-weather-flow wastewater hardly varied during the day.

During all measurements in dry-weather-flow conditions the wastewater surface tension varied between 45 and 55 mN/m. Therefore, measurements could be performed at constant liquid and gas flow rates. Figure 3.20 shows that the gas pocket head loss in wastewater is comparable with the head loss in clean water at  $F_w = 0.63$  and  $F_g = 0.004$ , despite the smaller surface tension of wastewater. Similar results were obtained at the other water and air discharges, as illustrated in Figure 3.21.

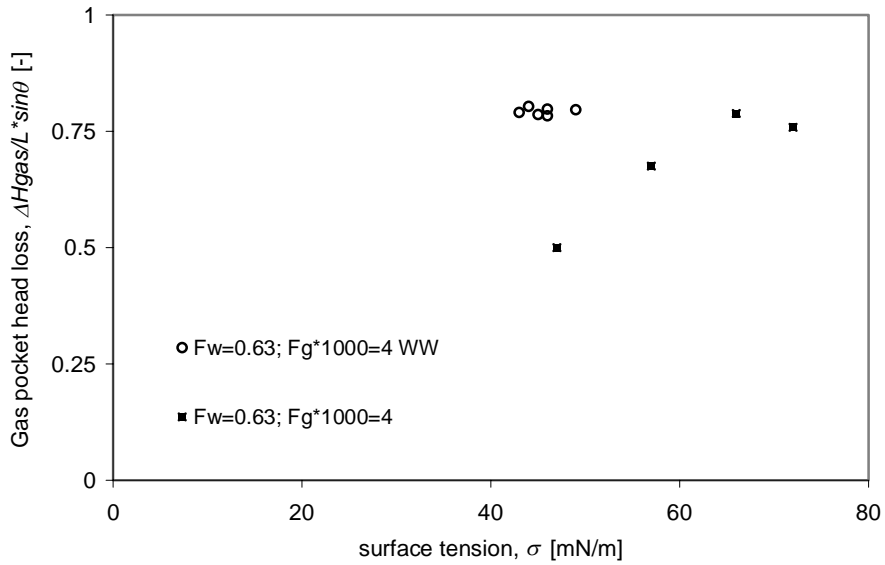


Figure 3.20: Influence of wastewater surface tension on gas pocket head loss in comparison with surfactant-added water

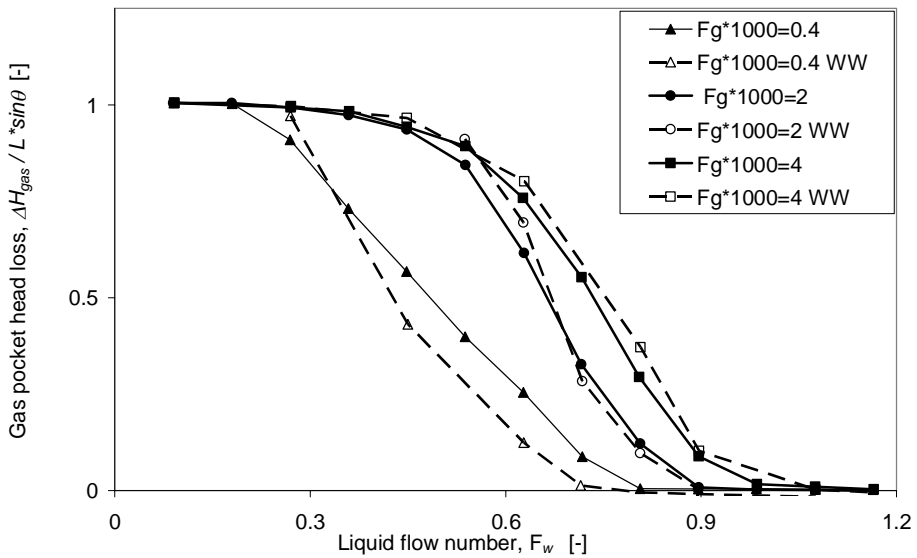


Figure 3.21: Gas pocket head loss in clean water and wastewater

The insensitivity of the air transport for the surface tension of wastewater may be caused by the lower molecular diffusion of the  $\sigma$ -reducing constituents in wastewater compared to the detergents used to reduce the surface tension of the clean water. In fact, the surface tension is a dynamic variable, because the detergents need time to reach an equilibrium between the interface concentration and the bulk concentration. In a lab analysis the dynamic evolution of the surface tension is dominated by molecular diffusion. Measurements of the dynamic surface tension of a couple of samples of wastewater and surfactant-added water were performed to investigate this dynamic behaviour. A  $10^{-5}$  solution with surfactants had a static surface tension of 44 mN/m, which is comparable with the surface tension of wastewater samples (Figure 3.22). The average composition of the wastewater in our facility was a 4:1 mixture of Wastewater1 and Wastewater2. The straight lines in Figure 3.22 confirm that the dynamic surface tension is diffusion-controlled.

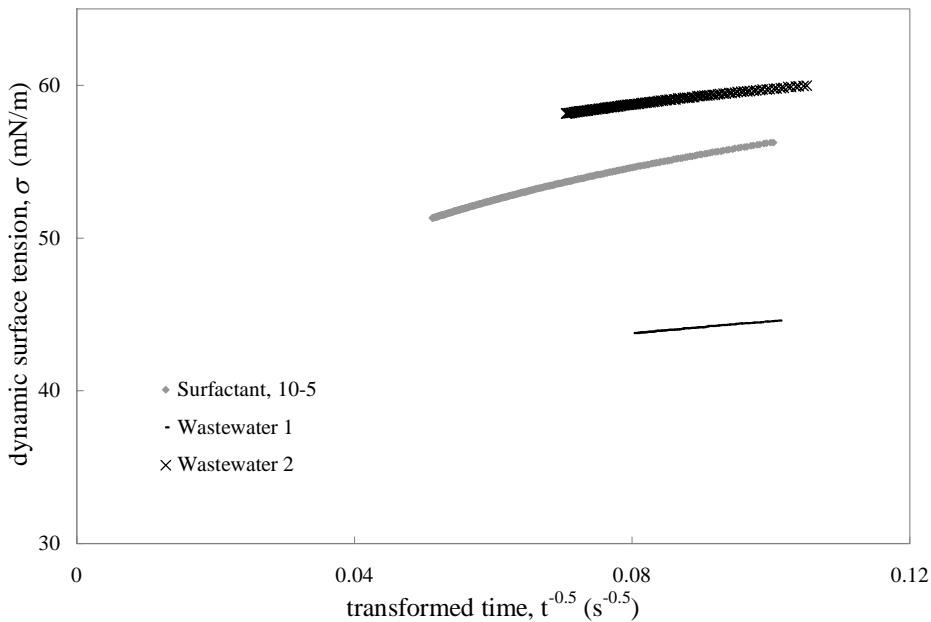


Figure 3.22: Plot of dynamic surface tension versus  $t^{-1/2}$

The gradients in Figure 3.22 do not differ by an order of magnitude. Therefore, the molecular diffusion in wastewater cannot explain the observed differences in the gas pocket head loss between wastewater and surfactant-added water.

Another explanation for the observed differences takes the turbulent mixing in the water film into account. On one hand, if a new interface is created in the top of the inverted siphon, turbulent mixing promotes the motion of surfactant particles towards the interface.



On the other hand, turbulence may shed particles from the interface. Therefore, turbulence may affect the time scale at which the equilibrium surface tension is reached and it may affect the equilibrium surface tension itself. Figure 3.23 shows that manual stirring of the sample accelerates the transport of surfactants towards the interface. The effect of stirring on the wastewater sample is less pronounced. The influence of turbulence on the surface has not been investigated in sufficient detail to draw firm conclusions, but the exploratory experiments indicate that turbulence has a more positive influence on the surfactant-added water than on the wastewater. Probably, the surfactants in wastewater (mainly proteins, fat molecules) are detached more easily from the interface than the surfactants added to the clean water.

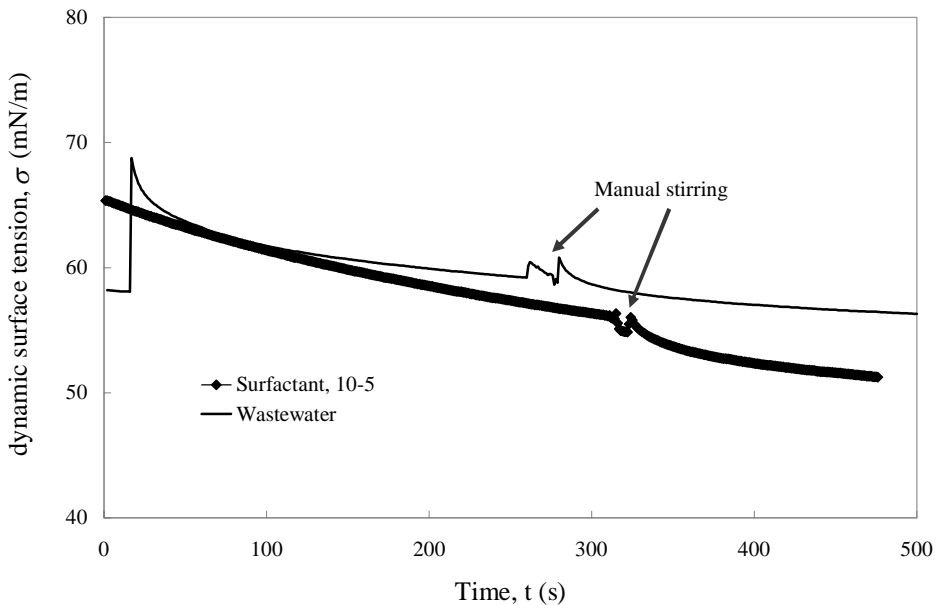


Figure 3.23: Dynamic surface tension with manual stirring

### 3.6 Limitations of air transport models

Current experimental correlations on the transported air-water ratio  $Q_a/Q_w$  are based on the Froude number at the toe of the hydraulic jump. The Froude number is the correct scaling parameter for the entrained air-water ratio, but it is highly questionable whether the same Froude number can be used to predict the net air transport ratio at the bottom of a downward sloping reach.

The air pockets in a downward sloping section are long enough to reach uniform flow at normal depth at the toe of the air-entraining hydraulic jumps. Therefore, the Froude number can be based on the normal flow condition. The relation between the flow number  $F_w$  and the Froude number at normal depth  $Fr_n$  shows that  $Fr_n$  is practically constant over a wide range of water flow numbers (Figure 3.24); the derivation of this relation is included in appendix A.2, *Free surface flow at normal depth*.

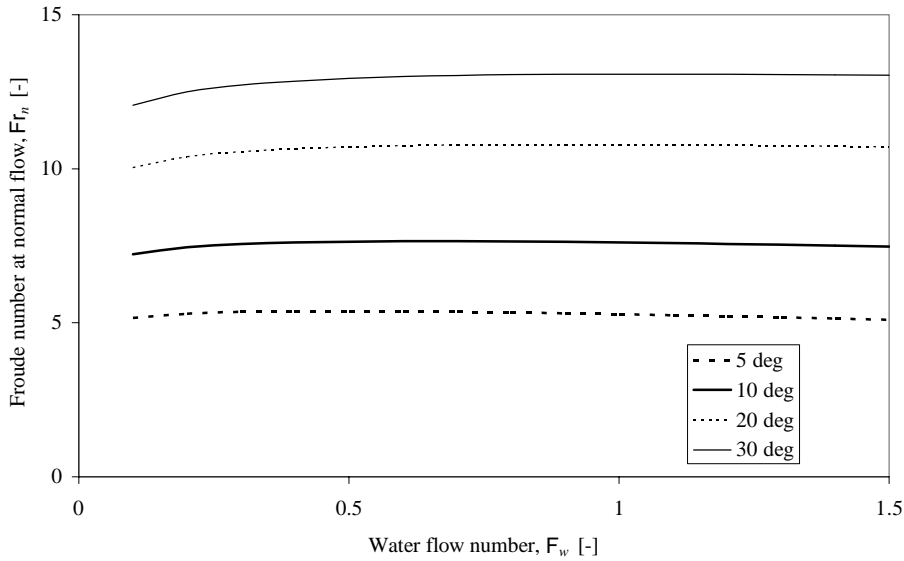


Figure 3.24: Froude number at normal flow condition as a function of the water flow number in a circular pipe with diameter  $D = 0.2$  m, wall roughness  $k_n = 0.1$  mm and kinematic viscosity  $\nu = 1.2E-6$ .

Since most investigators have proposed to model the air-water discharge ratio ( $Q_a/Q_w$ ) as a function of the Froude number only, this observation would imply that the air-water discharge ratio is constant over a wide range of water flow numbers. Figure 3.25 clearly shows that the data do not collapse to a single line, which proves that the air-water discharge ratio, even at a certain gas pocket head loss, cannot be derived from the Froude number at the toe of the hydraulic jump  $Fr_n$ .

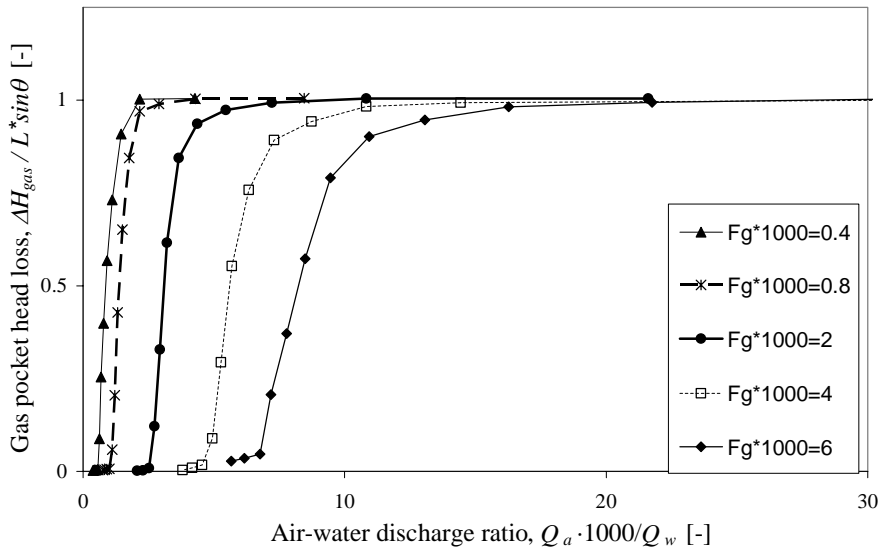


Figure 3.25: Gas pocket head loss as a function of the air-water discharge ratio; data from facility 4.

It is concluded that the Froude number  $Fr_n$  contains less information than the water flow number  $F_w$ , because the uniform flow Froude number remains constant over a wide range of water flow numbers at a given pipe angle.

It is concluded that the air transport model should not be based on the Froude number at the toe of a hydraulic jump. The water flow number seems a more promising scaling parameter, which will be exploited in the following chapters of this thesis.

## 4 Theoretical considerations

This chapter is based on a technical note, published by Journal of Hydraulic Research (Pothof and Clemens, 2010b). Pothof, Ivo and Clemens, Francois(2010) 'On elongated air pockets in downward sloping pipes', Journal of Hydraulic Research, 48: 4, 499 — 503. <http://dx.doi.org/10.1080/00221686.2010.491651>

### 4.1 Introduction

In this chapter, two criteria will be developed relating to flow regime transitions, provided that the influence of surface tension on the flow regime transition has become negligible. The surface tension influence is investigated in section 4.2. Section 4.3 and 4.4 discuss the energy balance and momentum balance that define the observed flow regime transitions. Both are validated with data from large-scale experimental facilities over a range of downward sloping pipe angles, lengths and diameters.

### 4.2 Surface tension influence on clearing velocity

Experimental data were acquired for  $\theta = 10^\circ$  over a range of pipe diameters, to analyze its effect. Dimensional analysis indicates that  $F_c$  depends on the water Reynolds number  $R \equiv \rho v_s D / \mu$  and the Eötvös number  $Eo \equiv \rho g D^2 / \sigma$ , characterizing the ratio of gravity to surface tension forces, where  $\sigma$  = surface tension and  $\rho$  = water density. Zukoski (1966) demonstrated that  $R$  is negligible for rising bubbles in inclined pipes if the drift flow number  $F_d > 0.1$  (i.e.  $D > 0.0084$  m). Figure 4.1: shows the clearing flow numbers for  $\theta = 10^\circ$  as a function of  $Eo$ . The curve labelled 'Various,  $10^\circ$ ' combines the data of Bendiksen (1984), Gandenberger (1957), Kent (1952) and Escarameia (2007). Kent did not consider  $\theta = 10^\circ$ , but an extrapolation to  $\theta = 10^\circ$  seems reasonable by combining Kent's and Escarameia's data. Zukoski's (1966) drift flow numbers  $F_d$  at  $\theta = 0^\circ$  and  $\theta = 15^\circ$  were included for comparison, confirming that  $Eo$  significantly affects both the drift and clearing flow numbers. Note that Zukoski's data were obtained in relatively short pipes, explaining the systematic deviation between the drift and clearing flow numbers. The present data require that  $D > 0.2$  m ( $Eo > 5,000$ ) to avoid scale effect.

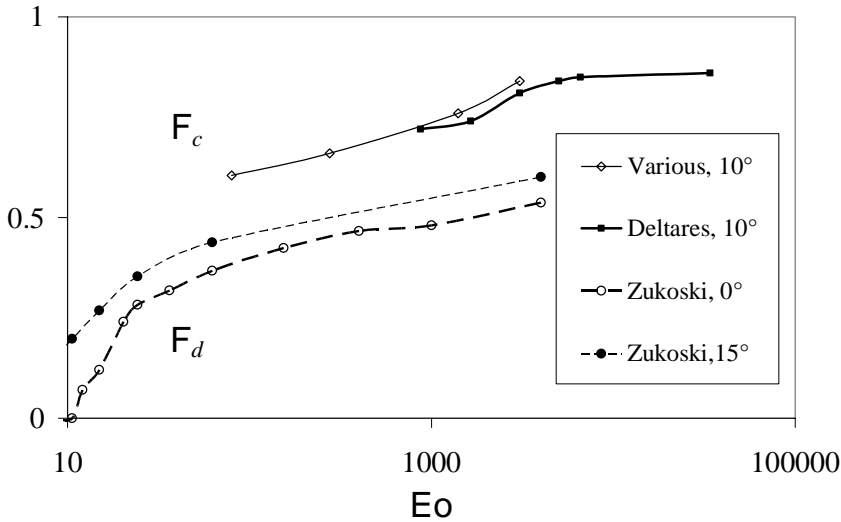


Figure 4.1: Effect of  $Eo$  on clearing flow number  $F_c$  and drift flow number  $F_d$  for pipe angle  $\theta=10^\circ$

### 4.3 Flow regime transition 2a to 2b

The experimental results in facility 4 show a clear transition from a single gas pocket to multiple gas pockets in the downward sloping reach. An analytical expression will be derived for this transition. The analysis of Montes (1997) for horizontal pipes is extended to arbitrary downward slopes, taking into account that a bubble nose corresponds to a stagnation point (Benjamin, 1968). Montes' stagnation criteria for horizontal rectangular and circular pipes express that specific energy of pressurised flow equals the specific energy of the stratified flow, resulting in

$$\text{Rectangular:} \quad \begin{cases} y_{cr} + \frac{v_{cr}^2}{2g} = \frac{3}{2} y_{cr} = D \\ F_s = \left(\frac{2}{3}\right)^{1.5} = 0.5443 \quad \text{at} \quad \frac{y_{cr}}{D} = \frac{2}{3} \end{cases} \quad (4.1)$$

$$\text{Circular:} \quad \begin{cases} y_{cr} + \frac{v_{cr}^2}{2g} = y_{cr} + \frac{A_{cr}}{2T_{cr}} = D \\ F_s = 0.5818 \quad \text{at} \quad \frac{y_{cr}}{D} = 0.6886 \end{cases} \quad (4.2)$$

where  $y$  = water film depth,  $v$  = film velocity,  $A$  = wet area,  $T$  = surface width and  $D$  = conduit height (rectangular) or pipe diameter (circular). Subscript  $cr$  refers to critical free surface flow ( $Fr = 1$ ) and subscript  $s$  refers to the stagnation condition for the transition from stratified to pressurised flow in a horizontal duct. The flow regime – i.e. stratified or pressurised flow – with the lowest specific energy will occur in the horizontal duct. The idea to compare the specific energy of stratified flow with that of pressurised flow is generalised to arbitrary pipe slopes. Eqs. (4.1) and (4.2) are generalised to arbitrary pipe slopes and air pressure heads.

The bubble nose is a stagnation point, so that the specific energy of pressurised flow (subscript  $p$ ) equals that at the bubble stagnation point. Neglecting the differential pressure due to surface tension, equation (4.3) expresses the condition at the bubble nose

$$\frac{P_p}{\rho_w g} + \frac{v_p^2}{2g} = D \cos \theta + \frac{P_g}{\rho_w g} \quad (4.3)$$

The specific energy of the stratified flow in a downward sloping pipe is

$$y \cos \theta + \frac{v_w^2}{2g} + \frac{P_g}{\rho_w g} \quad (4.4)$$

where  $y$  and  $v_w$  are the water depth and water film velocity. If the specific energies for pressurised and stratified flow are identical, then

$$y \cos \theta + \frac{v_w^2}{2g} + \frac{P_g}{\rho_w g} = D \cos \theta + \frac{P_g}{\rho_w g} \quad (4.5)$$

Eliminating the air pressure gives for the stagnation flow number (Figure 4.2)

$$F_s = \left( \frac{4A_w}{\pi D^2} \right) \left[ 2 \left( 1 - \frac{y}{D} \right) \cos \theta \right]^{1/2} \leq 0.5818 [\cos \theta]^{1/2} \quad (4.6)$$

The right-hand side of Eq. (4.6) has its maximum at  $y = 0.6886D$  at which  $Fr = 1$ . If  $F < F_s$ , the specific energy of stratified flow is smaller and stratified flow will prevail. The bubble nose of large bubbles thus always moves upward to the beginning of the downward sloping reach. The air pocket then accumulates along the entire downward sloping reach until the air in- and outflow have become identical. For  $F > 0.5818[\cos \theta]^{1/2}$ , both pressurised and stratified flows occur in the blow-back flow regime.

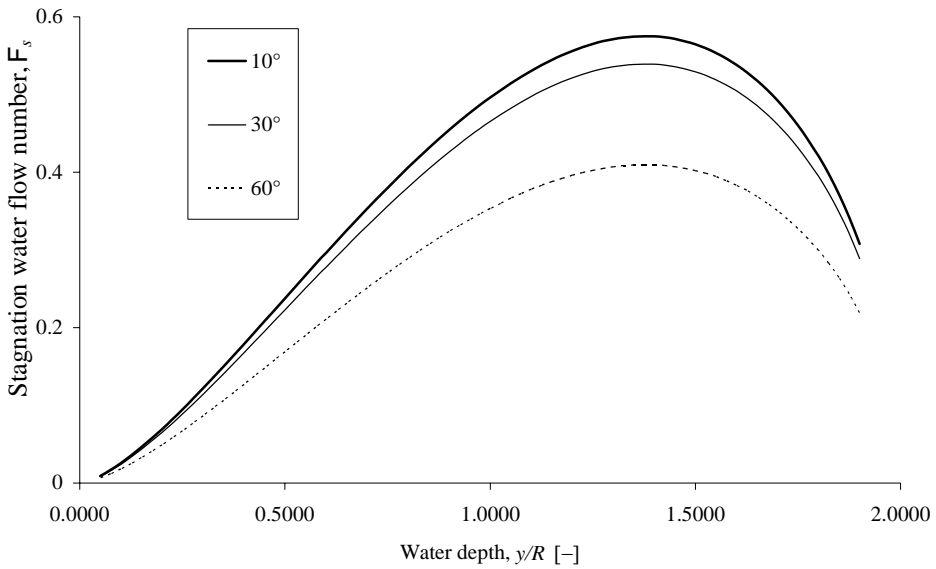


Figure 4.2: Stagnation flow number, at which stratified flow and pressurised flow have the same specific energy, plotted as a function of the stratified water depth. The labels refer to pipe angles.

#### 4.4 Flow regime transition 2b to 3

Air pocket motion is modelled by the forces on the control volume with dashed boundaries in Figure 4.3. Because surface tension effects are neglected, the analysis is limited to  $E_o > 5,000$ .

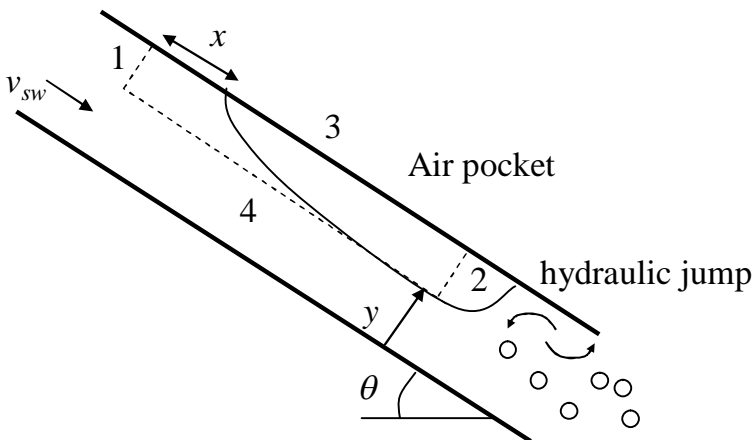


Figure 4.3: Definition sketch for momentum balance of elongated air pocket

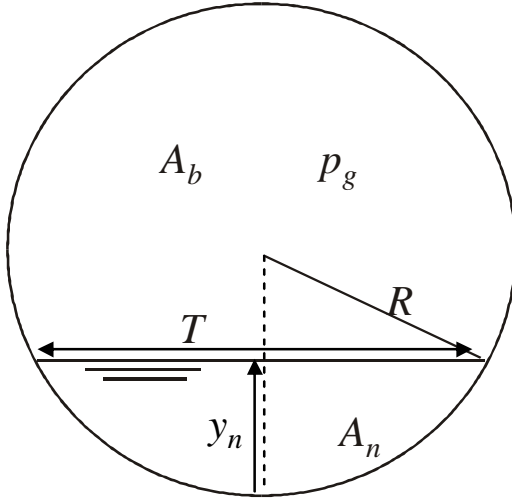


Figure 4.4: Definition sketch for momentum balance, if elongated air pocket reaches normal depth at cross section 2

The force on surface 2 equals  $(p_g A_b)$ , neglecting a hydrostatic pressure gradient in the air pocket, which is a valid assumption at a small air-water density ratio:  $\rho_g \ll \rho_w$ . The water pressure at the air pocket nose equals the air pocket pressure  $p_g$ , presuming that the surface tension effect is negligible. Furthermore, the internal air circulation does not affect the stagnation pressure at the bubble nose. At upstream boundary 1, the liquid streamlines are parallel. There, the local pressure at the pipe soffit  $p_{1,y=D}$  is smaller than the air pocket pressure because of higher elevation, and deceleration towards the bubble nose, according to Bernoulli. Distance  $x$  from section 1 to the bubble nose is of the order of the bubble height. The pressure at the pipe soffit at section 1 is

$$p_{1,y=D} = p_g - \frac{\rho_w}{2} v_{sw}^2 - \rho_w g \cdot x \cdot \sin \theta \quad (4.7)$$

Since streamlines are parallel at section 1, the liquid pressure is hydrostatic. Hence, the average pressure  $\bar{p}_1$  results from integrating the hydrostatic pressure distribution across the bubble area  $A_b$  from the water depth  $y$  to the pipe soffit  $D$  as

$$\bar{p}_1 = p_g - \frac{\rho_w}{2} v_{sw}^2 - \rho_w g \cdot x \cdot \sin \theta + \cos \theta \cdot \frac{\rho_w g}{A_b} \int_y^D (D-y) T(y) dy \quad (4.8)$$

where  $T(y)$  = conduit width at distance  $y$  above the pipe bottom. The analytical solution is



$$\int_y^D (D-y)T(y)dy =$$

$$= R^3 \left[ \frac{2}{3} \sqrt{\frac{2y}{R} - \left(\frac{y}{R}\right)^2} \left(\frac{y}{R} - 3\right) \left(\frac{y}{R} - \frac{1}{2}\right) + \arcsin\left(1 - \frac{y}{R}\right) + \frac{\pi}{2} \right] \quad (4.9)$$

The body force on the control volume includes the water mass between section 1 and the bubble nose, thereby neglecting the air pocket mass. No shear force acts on the control volume along the pipe soffit (boundary 3). The axial momentum, entering through boundary 1, leaves through boundary 4. The shear force at boundary 4 increases the liquid momentum between boundaries 1 and 4 and the assumption is that the shear force on boundary 4 equals the axial momentum increase. A physical explanation for this assumption is that the air pocket motion is not affected by the acceleration of water around the bubble nose. The bubble motion is determined from pressure forces on boundaries 1 and 2 and a body force, i.e.

$$\bar{p}_1 \cdot A_b - p_g \cdot A_b + A_b \cdot x \cdot \rho_w g \cdot \sin \theta = 0 \quad (4.10)$$

Substitution of Eqs. (4.8) and (4.9) in Eq. (4.10) eliminates the air pressure and distance  $x$ , so that division by  $\rho_w g A_b D$  results in

$$\frac{v_{sw}^2}{gD} = \frac{A_D \cos \theta}{A_b \pi} \left[ \frac{2}{3} \sqrt{\frac{2y}{R} - \left(\frac{y}{R}\right)^2} \left(\frac{y}{R} - 3\right) \left(\frac{y}{R} - \frac{1}{2}\right) + \arcsin\left(1 - \frac{y}{R}\right) + \frac{\pi}{2} \right] \quad (4.11)$$

where  $A_D$  = pipe cross-section. The resulting momentum balance states that an elongated air pocket stays at a fixed position, if the stagnation pressure of the pressurized flow equals the average hydrostatic pressure upstream of the air pocket. This momentum balance applies to all situations in which the water film velocity is supercritical; this situation may occur at any pipe slope, except for nearly vertical pipes. The maximum air pocket cross-section  $A_b$  is reached if the water film thickness reaches the uniform flow at normal depth  $y_n$ . The non-dimensional form of the uniform flow equation is

$$F_w^2 = \frac{v_{sw}^2}{gD} = \frac{2 \sin \theta}{\lambda} \frac{D_h}{D} \left( \frac{A_{w,n}}{A_D} \right)^2 \quad (4.12)$$

with  $D_h$  = hydraulic diameter at normal depth. The friction factor  $\lambda$  is computed from e.g. the White-Colebrook equation. If Eqs. (4.11) and (4.12) are satisfied simultaneously, an analytical expression for the clearing flow number of an individual elongated gas pocket  $F(\theta)$  as a function of the downward pipe angle  $\theta$  and the normal depth  $y_n$  is obtained as

$$\begin{aligned}
F^2(\theta) = & \frac{\sin \theta}{\lambda} \frac{D_h}{D} \left( \frac{A_n}{A_D} \right)^2 + \\
& + \frac{A_D}{A_b} \frac{\cos \theta}{2\pi} \left[ \frac{2}{3} \sqrt{\frac{2y_n}{R} - \left( \frac{y_n}{R} \right)^2} \left( \frac{y_n}{R} - 3 \right) \left( \frac{y_n}{R} - \frac{1}{2} \right) + \arcsin \left( 1 - \frac{y_n}{R} \right) + \frac{\pi}{2} \right] \quad (4.13)
\end{aligned}$$

Figure 4.5 shows Eq. (4.13) and  $F_c$  obtained by Deltares for  $0.0003 \leq F_g \leq 0.0075$  (Lubbers, 2007). Wickenhäuser and Kriewitz (2009) reported experimental data on the required water discharge to prevent air accumulation in a large diameter pipe of  $D = 0.484$  m. These data extend the Deltares dataset for small air discharges and  $\theta < 5^\circ$ . These data also confirm that a 220 mm pipe is suitable for extrapolation to larger diameters. The derived momentum balance in Eq. (4.13) reproduces the observed trends, except for an air-discharge-dependent offset because: (1) at the smallest air flow numbers a fraction of the air dissolves in the hydraulic jump, reducing the volume of secondary air pockets. Consequently, uniform flow is not reached and the clearing flow number decreases accordingly; (2) the pipe joints are not perfectly smooth, so that elongated bubbles stick at these imperfections. Therefore, the elongated bubbles require a somewhat larger clearing velocity. The validity of the second argument was confirmed with a video-analysis of the motion of an elongated air pocket at  $F_w = 0.94$  just above the clearing flow number  $F_c$ . Given that Eq. (4.13) was derived for an individual elongated air pocket without continuous air supply, the observed trends match Eq. (4.13) reasonably well for  $\theta \leq 30^\circ$ . A numerical evaluation of Eq. (4.13) versus pipe diameters for  $Eo > 5,000$  ( $0.2 \text{ m} \leq D \leq 0.5 \text{ m}$ ) and a typical range of relative wall roughness  $10^{-4} \leq k_n/D \leq 10^{-3}$  indicates that the flow number variation is less than  $\pm 3\%$  over these ranges considered.

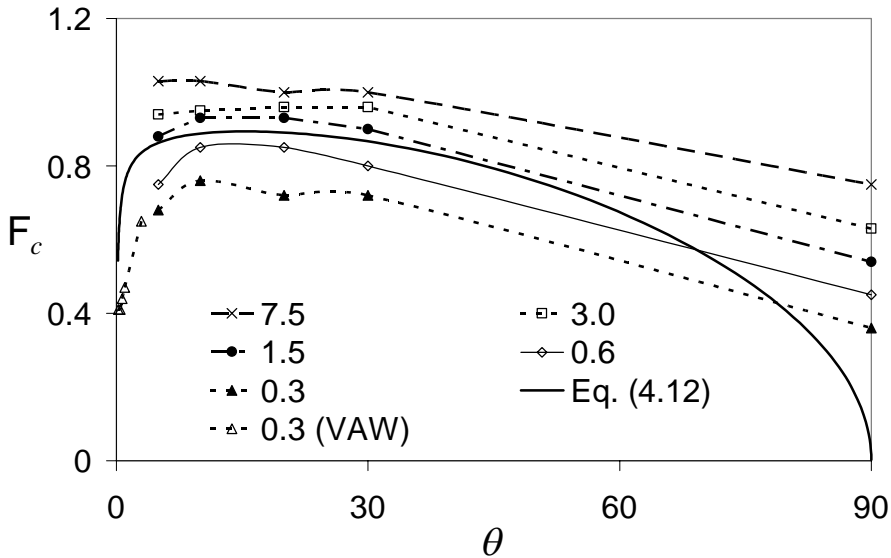


Figure 4.5: Clearing flow number  $F_c$  following Eq. (4.13) and test data of (Lubbers, 2007) and (Wickenhäuser and Kriewitz, 2009). Label numbers denote air flow number  $F_g \times 1,000$

## 4.5 Conclusions

The behaviour of elongated air pockets in downward sloping pipes was investigated to provide suitable water velocity criteria for practical applications with entrapped air pockets. The first velocity criterion derived from energy considerations marks the presence of multiple air pockets in the blow-back flow regime, which implies that the maximum air pocket head loss decreases if the water flow number the criterion value. The second velocity criterion, derived from a momentum balance, defines the clearing velocity, at which the nose of an air pocket just starts moving in downward direction. This criterion was demonstrated to be equivalent with the transition from the blow-back to the plug flow regime, apart from an air-discharge-dependent offset. Furthermore, it was shown that the clearing flow number becomes independent of the pipe diameter, if  $D > 0.19$  m in an air-water system. The derivation of the momentum balance seems applicable to air pocket rise velocities as well, but experimental data are not available at a sufficiently large scale. It is also recommended to determine the maximum pipe slope at which the derived momentum balance is still valid.

## 5 Air transport model

This chapter is extracted from a paper published in International Journal of Multiphase Flow (Pothof and Clemens, 2010a).

<http://dx.doi.org/10.1016/j.ijmultiphaseflow.2010.10.006>

### 5.1 Introduction

Current two-phase flow codes, like MAST (Bonizzi et al., 2009) or OLGAR<sup>®</sup> (De Leebeeck et al., 2008; SPT Group Norway, 2010), have been developed and calibrated for typical applications in which the gas phase drives the liquid phase. The existing two-phase flow codes are not designed to make reliable predictions of the pressure drop and air discharge in applications in which the liquid phase drives the gas phase. Air-water flows in downward sloping pipes with low superficial air velocities ( $v_{sg} \sim 1$  mm/s) and moderate superficial water velocities ( $v_{sw} \sim 1$  m/s) are dominated by water turbulence, bubble drag and buoyancy. Therefore, a novel model will be developed in this section. The model is based on experimental correlations and conservation laws. The main objective of the model is the prediction of the total air discharge as a function of the water discharge, air accumulation and system configuration (i.e. pipe diameter, slope angle, slope length). Such a model computes the air pocket break down and accumulation in time in a downward sloping pipe section.

The condition of uniform water flow, in which gravity and wall friction forces are balanced, will play an important role in the model. The non-dimensional expression of the uniform flow momentum balance is

$$F_w^2 = \frac{v_{s,w}^2}{gD} = \frac{2 \sin \theta}{\lambda} \frac{D_h}{D} \left( \frac{A_n}{A_D} \right)^2 \quad (5.1)$$

where  $A_n$ ,  $A_D$  and  $D_h$  are the water cross-sectional area, pipe cross-sectional area and hydraulic diameter of the water film at normal depth. The geometric relations in circular tubes are summarised in appendix A. The friction factor  $\lambda$  is computed from e.g. the White-Colebrook equation. Experiments in facility 5 show that uniform flow at normal depth is established after approximately 9D. Any significant air accumulation is longer than 9D. Therefore the rate of change of the air accumulation will be based on the uniform flow condition, i.e.

$$Q_{g,in} - Q_g = A_b \frac{dL_g}{dt} = (A_D - A_n) \frac{dL_g}{dt} \quad (5.2)$$

where  $L_g$ ,  $Q_{g,in}$ ,  $Q_g$  and  $A_b$  are the aggregated air pocket length, external air inflow at the top, the net air discharge at the bottom of the downward sloping reach and the maximum bubble cross-sectional area. Equation (5.2) is expressed in a non-dimensional way via division by  $A_D(gD)^{1/2}$ .

$$F_{g,in} - F_g = \frac{(1 - A_n/A_D) dL_g}{\sqrt{gD} dt} \quad (5.3)$$

The gas pocket head loss is derived from the total gas pocket length as

$$\frac{\Delta H_g}{L \sin \theta} = \frac{L_g}{L} \Leftrightarrow \Delta H_g = L_g \sin \theta \quad (5.4)$$

This approximation overestimates the actual gas pocket head loss, as illustrated in Figure 3.13. The remainder of this chapter focuses on the determination of the gas flow number  $F_g$ . At first, the model will be validated with the experimental data at  $Eo > 5000$  (i.e. data from facilities 4, 5, 6 and 7) and pipe angles  $\theta \leq 30^\circ$ . First, the air transport in the plug flow regime is modelled. The influence of air accumulation in the blow back flow regime is modelled as a correction to this plug flow air transport.

## 5.2 Air transport model in plug flow regime

The applicable momentum balance has been derived in chapter 4, equation (4.13), copied in (5.5). This momentum balance predicts when an elongated air pocket remains in a stable position in a downward sloping pipe, assuming the pipe is large enough to neglect the influence of surface tension ( $Eo > 5000$ ).

$$F^2(\theta) = \frac{\sin \theta}{\lambda} \frac{D_h}{D} \left( \frac{A_n}{A_D} \right)^2 + \frac{A_D}{A_b} \frac{\cos \theta}{2\pi} \left[ \frac{2}{3} \sqrt{\frac{2y_n}{R} - \left( \frac{y_n}{R} \right)^2} \left( \frac{y_n}{R} - 3 \right) \left( \frac{y_n}{R} - \frac{1}{2} \right) + \arcsin \left( 1 - \frac{y_n}{R} \right) + \frac{\pi}{2} \right] \quad (5.5)$$

where  $y_n$  and  $R$  are the water film thickness at normal depth and the pipe radius; the other symbols have been explained before. If the water flow number exceeds the criterion value, then a single elongated air pocket cannot sustain itself in the downward sloping reach and will move along the pipe soffit at a certain velocity that can be predicted from a drift flux model. Therefore, the momentum balance in equation (5.5) marks the transition from blow-back to plug flow, apart from an air-discharge-dependent factor (Figure 4.5). Figure 3.14b

suggests that the air transport capacity in the plug flow regime increases exponentially as a function of the water flow number. Figure 5.1 shows the experimental data from Figure 3.14a as a function of  $F_w/F(\theta)$  on a semi-log scale.

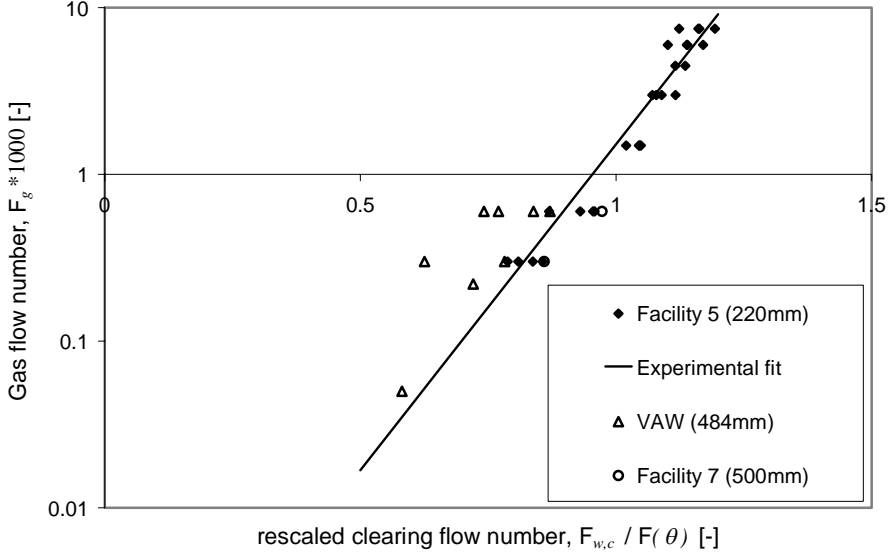


Figure 5.1: Gas transport capacity at the transition to plug flow. Facility 5 points include data at  $5^\circ \leq \theta \leq 30^\circ$ ; Facility 7 data points include data at  $\theta = 10^\circ$ ; VAW data points include data at  $1^\circ \leq \theta \leq 5^\circ$ .

Figure 5.1 confirms the exponential increase of the air discharge. The experimental data are best correlated by equation (5.6) with  $R^2 = 0.93$

$$F_g = 1.87 \cdot 10^{-7} \exp\{9F_w/F(\theta)\} \quad (5.6)$$

Taking into account the experimental result of the influence of surface tension (Figure 3.18), yields

$$F_g = 1.87 \cdot 10^{-7} \exp\left\{9 \frac{F_w}{F(\theta)} \left(\frac{0.072}{\sigma}\right)^{1/2}\right\} \quad (5.7)$$

Equation (5.6) is inverted to obtain an expression for the required water flow number to prevent accumulation of air pockets in a downward sloping pipe (i.e. clearing flow number).

$$F_c = F(\theta) \left(\frac{\sigma}{0.072}\right)^{1/2} \ln \left[ \left(\frac{F_g \cdot 10^7}{1.87}\right)^{1/9} \right] \quad (5.8)$$

The clearing flow number in equation (5.8) is valid for air-water flow in pipes with  $D > 0.190$  m (or  $Eo > 5000$ ). Equation (5.8) provides a more complete description of the clearing flow number than existing correlations from literature (Figure 5.2), because it accounts for the air discharge and surface tension as well. Furthermore, it is concluded that the influence of the pipe angle can be modelled with the derived momentum balance for a single elongated air pocket (eq. (5.5)).

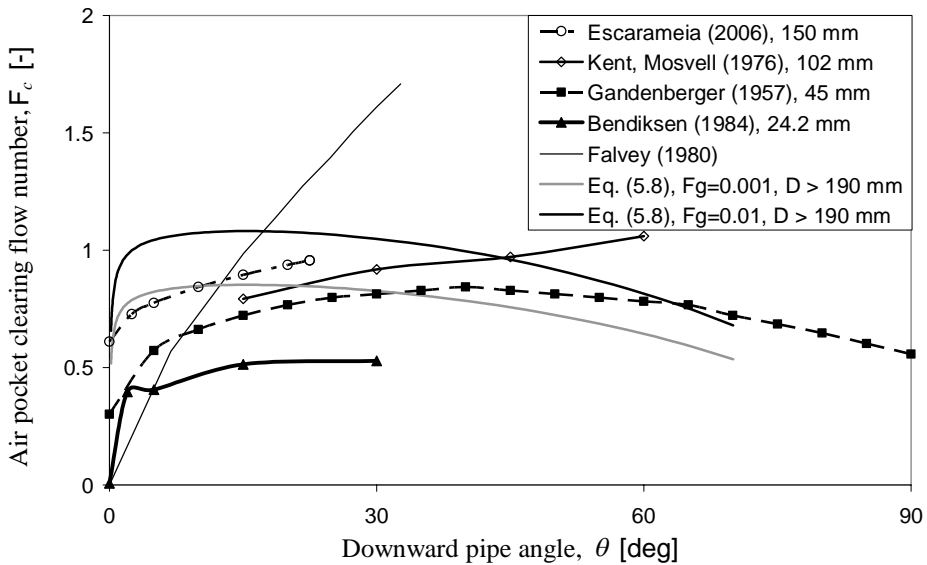


Figure 5.2: Clearing flow numbers from literature and equation (5.8) at two different air flow numbers

### 5.3 Air transport model in blow-back flow regime

The relevance of equation (5.8) in the blow-back flow regime is illustrated with the experimental results from Figure 3.12b. If the water flow number is rescaled by the experimental clearing flow number or equation (5.8), most of the experimental data in Figure 3.12b collapses to a single line (Figure 5.3). Only the data at the smallest air flow number ( $F_g \cdot 1000 = 0.4$ ) differs significantly from this line.

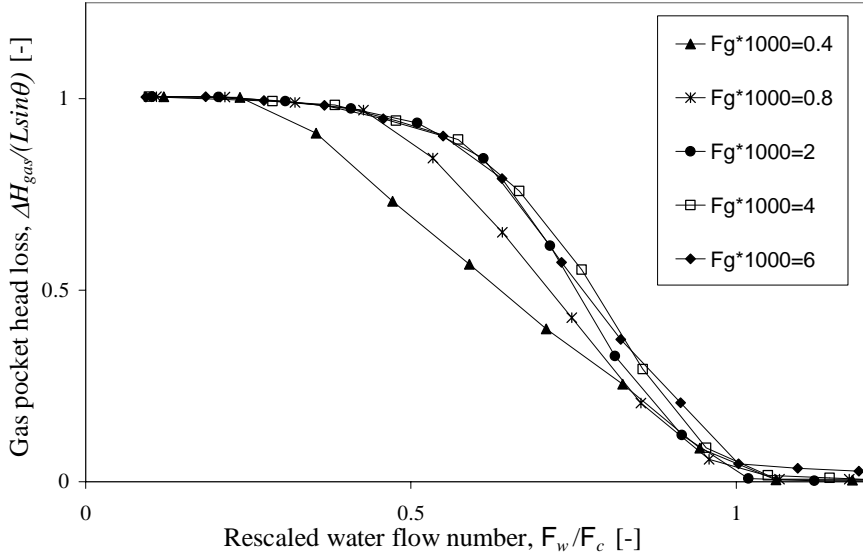


Figure 5.3: Gas pocket head loss as a function of the water flow number ratio  $F_w / F_c$ .

The single line in Figure 5.3 can be approximated with a cumulative beta distribution function  $B(x, \alpha, \beta)$ , that predicts which combinations of gas pocket head loss and water flow number result in the same air discharge. The function  $B(x, \alpha, \beta)$  includes three parameters:  $x$  is the rescaled water flow number and  $\alpha$  and  $\beta$  will be shown to be functions of the inclined section length only.

$$1 - R = B(x, \alpha, \beta) = \frac{\int_0^x t^{\alpha-1} (1-t)^{\beta-1} dt}{\int_0^1 t^{\alpha-1} (1-t)^{\beta-1} dt} \quad (5.9)$$

with

$$\begin{aligned} R &= \Delta H_{gas} / (L \sin \theta) \\ x &= F_w / F_c \\ \alpha &= 9.67 \cdot 10^{-2} (L/D - 10.3)^{0.783}, \quad 20 \leq L/D \leq 210 \\ \beta &= 9.39 \cdot 10^{-3} L/D + 0.439 \end{aligned} \quad (5.10)$$

More information on properties of the beta distribution function is found in (Johnson et al., 1994). The model in eq. (5.9) and (5.10) and Figure 5.3 show that the inverse beta function can be incorporated in eq. (5.6) to model the air transport in the blow-back flow regime



$$F_g = 1.87 \cdot 10^{-7} \exp \left\{ 9 \frac{F_w}{F(\theta)} \left( \frac{0.072}{\sigma} \right)^{1/2} \frac{1}{B^{-1}(1-R, \alpha, \beta)} \right\} \quad (5.11)$$

The model equations combine a physically based momentum balance with a minimum number of empirical parameters to obtain a prediction of the volumetric air transport by flowing liquid at the bottom of a downward sloping reach. The calibration results are shown in Figure 5.4 and Figure 5.5. Figure 5.4 shows an excellent fit for air flow numbers  $F_g \cdot 1000 \geq 0.8$ . Figure 5.5 compares the experimental data and model results at different pipe angles and length of the downward sloping reaches. It shows that the model provides accurate predictions at downward sloping reach lengths  $L/D > 30$ , which are the most relevant in practice. For shorter downward sloping reaches, the assumption in eq. (5.1) is affecting the results significantly.

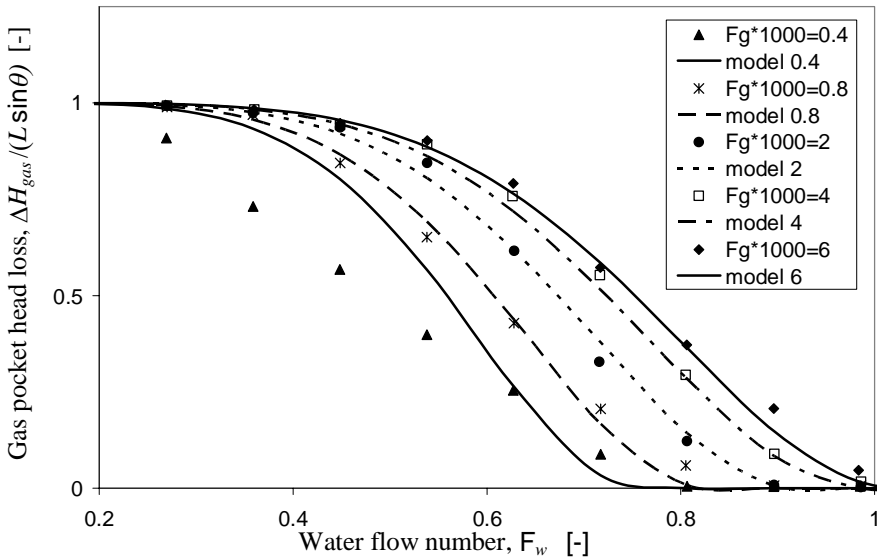


Figure 5.4: Comparison of experimental data points from facility 4 (markers) with model equations (lines).

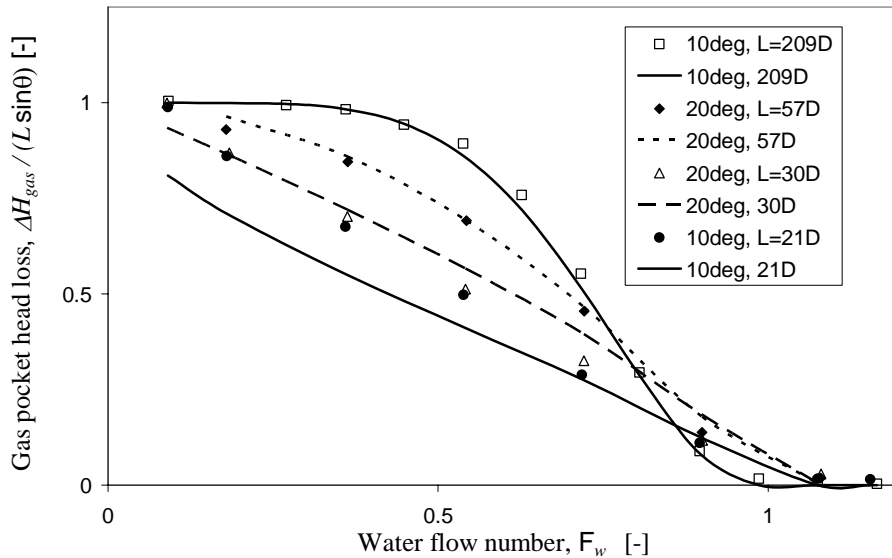


Figure 5.5: Comparison of experimental data points (markers) with model equations (lines) over the range of slope lengths and  $F_g \cdot 1000 = 4.5$ .

#### 5.4 Air transport at $Eo < 5000$

The presented model was developed for air-water flows in pipelines with  $D > 0.19$  m ( $Eo > 5000$ ). At smaller pipe diameters or Eötvös numbers, the non-dimensional total air discharge increases to some extent and the clearing velocity decreases, as illustrated for example in Figure 5.2.

The experimental data from Gandenberger (1957), Kent (1952) and Escarameia (2007), combined in Figure 5.2 suggest that the clearing velocity in small diameter pipes can be predicted from the hydraulic gradient, which combines the flow number and the Reynolds number influence via the friction factor. Figure 4.1 shows that the Deltares data, which was acquired with a single method, follows the same trend as the single pocket clearing velocity data from literature. Therefore, the air transport model is extended with a Reynolds number influence on the clearing velocity. The introduction of the friction clearing flow number  $F_{fc} \equiv F_c \cdot (\lambda)^{1/2}$  translates the clearing velocity into a required hydraulic gradient, as outlined in section 2.2.1. Figure 5.6 shows a nearly constant friction clearing flow number over a wide range of Eötvös numbers from  $Eo = 80$  ( $D = 0.0242$  m) to  $Eo = 6.6 \cdot 10^3$  ( $D = 0.22$  m). The average friction clearing flow numbers equals 0.109, which corresponds with a required hydraulic gradient of 6 metre per kilometre. The friction factor values of the

literature sources have been based on an assumed relative roughness  $k_n/D = 10^{-4}$ , which is reasonably close to the hydraulically smooth wall. Figure 5.6 reveals a weak declining trend in the experimental data, but a trend line explains only 50% of the observed variance. It is concluded from Figure 5.6 that the friction clearing flow number is approximately constant for  $Eo < 5000$  (or  $D < 0.191$  m).

$$F_c \sqrt{\lambda} \approx 0.109 \quad (5.12)$$

Figure 5.6 suggests that the friction flow number, eq. (5.12), can be used to explain the larger air transport and smaller clearing flow numbers at  $Eo < 5000$  (or  $D < 0.191$  m). The friction factor is a function of the Reynolds number and relative wall roughness. Since experimental friction factors follow the hydraulically smooth curve up to a certain Reynolds number, the friction factor influence reduces to a Reynolds number influence over the investigated range of wall roughnesses ( $k_n/D < 10^{-3}$ ) and applicable Reynolds numbers. A reference Reynolds number is defined at  $D = 0.19$  m and  $F_c = 0.9$ , where  $Re_{c,ref} = 1.9 \cdot 10^{+5}$ . Equation (5.12) can be reformulated in terms of the reference Reynolds number using Blasius' correlation, provided that  $Re_c \leq Re_{c,ref}$ .

$$F_c \cdot Re_c^{-1/8} = F_{c,ref} \cdot Re_{c,ref}^{-1/8} \quad (5.13)$$

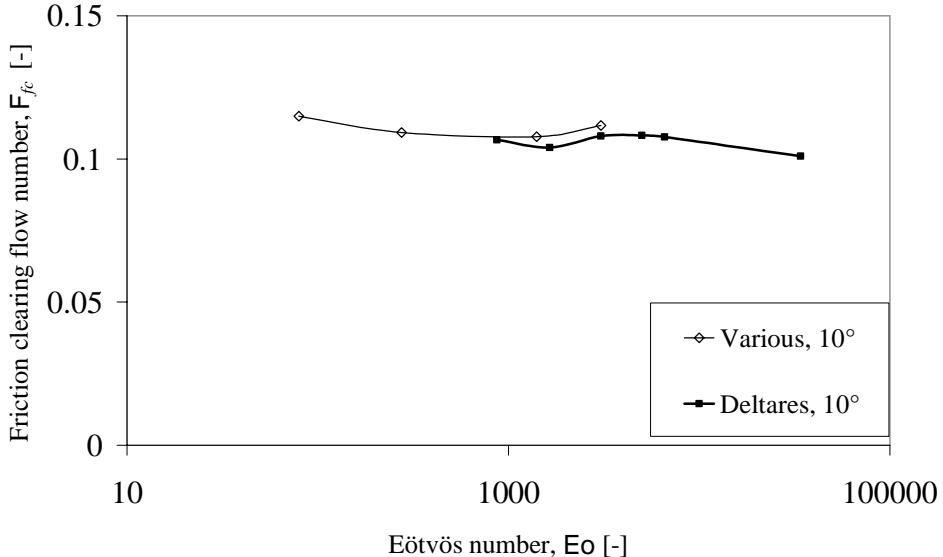


Figure 5.6: Friction clearing flow number from Deltares facilities 1 – 5 and 7 and various investigators (Bendiksen, 1984; Escarameia, 2007; Gandenberger, 1957; Kent, 1952)

Since the velocity is present in both the flow number and Reynolds number, equation (5.13) is algebraically solved for the velocity, so that the Reynolds influence reduces to diameter and viscosity influence, yielding

$$\left( \frac{F_c}{F_{c,ref}} \right) = \left( \frac{\min\{D, 0.19\} 10^{-6}}{0.19} \frac{\nu}{\nu} \right)^{3/14} \quad (5.14)$$

The above clearing velocity correlation is incorporated in the clearing velocity correlation, eq. (5.8), to account for these effects.

$$F_c = F(\theta) \cdot \left( \frac{\sigma}{0.072} \right)^{1/2} \left( \frac{\min\{D, 0.19\} 10^{-6}}{0.19} \frac{\nu}{\nu} \right)^{3/14} \cdot \ln \left[ \left( \frac{F_g \cdot 10^7}{1.87} \right)^{1/9} \right] \quad (5.15)$$

Finally, inversion of equation (5.15) yields the air transport at the transition to the plug flow regime as a function of pipe angle, diameter, surface tension, viscosity and water flow number.

$$F_g = 1.87 \cdot 10^{-7} \exp \left\{ 9 \frac{F_w}{F(\theta)} \left( \frac{0.19}{\min\{D, 0.19\}} \frac{\nu}{10^{-6}} \right)^{3/14} \left( \frac{0.072}{\sigma} \right)^{1/2} \right\} \quad (5.16)$$

The air transport equation in the blow back flow regime can be adjusted accordingly. The validity of the complete clearing velocity equation (5.15) is illustrated in Figure 5.7, showing experimental and numerical gas pocket head loss values in facilities 1, 3 and 5.

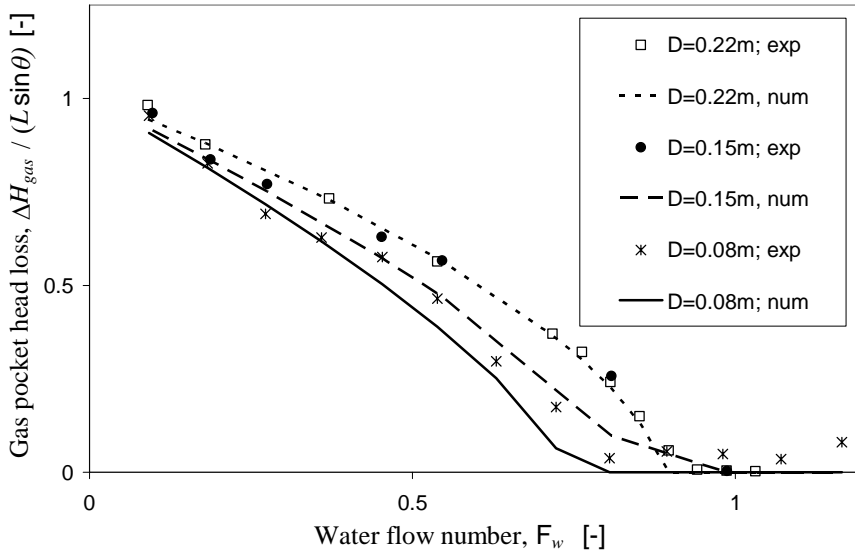


Figure 5.7: Gas pocket head loss measurements (markers) and calculations (lines) as a function of the water flow number at  $F_g \cdot 1000 = 1.5$  in facilities 1, 3 and 5.

## 5.5 Discussion

Surface entrainment was not observed in the experiments in the transparent facilities with pipe diameters up to 220 mm and Reynolds numbers up to 250,000. The experimental data in facility 7 (500 mm, steel) suggest that surface entrainment did not occur in facility 7 either. It remains to be verified whether surface entrainment may enhance the air transport at much larger Reynolds numbers ( $> 10^6$ ).

The model has been validated with data on downward sloping reaches with a maximum length  $L/D = 209$ . Many inverted siphons are longer. Energy considerations, detailed in section 4.3, show that the maximum gas pocket head loss can occur only at  $F_w < 0.58[\cos(\theta)]^{1/2}$ . The experiments in facility 4 ( $L/D = 209$ ) show that the gas pocket head loss remains reasonably close to the maximum value of unity at  $F_w < 0.58[\cos(\theta)]^{1/2}$  at air flow numbers  $F_g > 0.001$  (Figure 5.4). Therefore, a maximum length  $L/D = 209$  seems valid for longer downward sloping reaches.

A small number of measurements at an increased downstream pressure indicates that a large fraction of the air dissolves into the water phase, especially at gas flow numbers  $F_g \leq 0.001$ . These are issues for further investigations.

A strong similarity exists between the behaviour of gas pockets in downward sloping pipes and the elongated bubble drift velocity in inclined pipes. Since bubble drift velocities have not yet been determined in pipelines of sufficient length ( $L/D > 20$ ) and Eötvös number  $Eu > 5000$  (or  $D > 0.19$  m)—despite its relevance for slug flow modelling—it is recommended to determine the bubble drift velocities over a range of upward pipe angles.

The main air transport mechanism in the blow-back flow regime is turbulent bubble transport in the hydraulic jumps. A turbulent diffusion coefficient  $\varepsilon_y$ , based on the energy dissipation in hydraulic jumps (eq. (2.25)), can be included in a 2D advection-diffusion model of the local air bubble concentration. Other processes that would have to be incorporated in such a model include the bubble rise velocity and a certain slip velocity. The following partial differential equation may serve as a starting point for more detailed numerical modelling work:

$$(u - v_r \sin \theta - u_s) \frac{\partial C}{\partial x} + v_r \cos \theta \frac{\partial C}{\partial y} - \varepsilon_y \frac{\partial^2 C}{\partial y^2} = 0 \quad (5.17)$$

where  $u$  is the water velocity,  $v_r$  is the bubble rise velocity,  $u_s$  the slip velocity and  $C$  the bubble concentration. Such an approach would have to be combined with the motion of the elongated air pockets that slowly drift in upstream direction in the blow-back flow regime. A drift flux approach (eq. (2.10)) in combination with the derived momentum balance (eq. (4.13)) could be exploited. A number of parameters in such a detailed numerical model require further experimental investigations:

- 1 the air entrainment in the hydraulic jump in a circular tube with fully developed inflow conditions, which is a boundary condition for an advection-diffusion model;
- 2 the determination and validation of a representative bubble size or bubble size distribution;
- 3 the bubble dynamics – break-up and coalescence – in the hydraulic jump.

## 5.6 Conclusions & recommendations

A large number of co-current air-water flow experiments in downward sloping pipes were performed in similar experimental facilities covering a wide range of pipe diameters (80 – 500 mm, with focus on 220 mm), slope length ( $21D$  to  $209D$ , with focus on  $30D$ ) and pipe angles ( $5^\circ$ ,  $10^\circ$ ,  $20^\circ$ ,  $30^\circ$  and  $90^\circ$ , with focus on  $10^\circ$ ). The experiments show that the air transport by flowing water in downward sloping pipes is a function of the water flow number, pipe angle and air accumulation. The required water velocity to prevent air accumulation scales with the clearing flow number, provided that the Eötvös number

$Eo > 5000$ . In the blow back flow regime, the gas pocket head loss scales with the pipe Weber number.

If the pipe diameter  $D < 0.19$  m or  $Eo < 5000$ , the motion of an individual elongated air pocket is started if the undisturbed hydraulic grade line – i.e. without air pockets – exceeds 0.6% (6 metre per kilometre). This expression has been obtained in pipes with relative wall roughness  $k_r/D < 10^{-3}$  and pipe diameters  $D > 0.08$  m.

An expression for the clearing water flow number has been deduced from the experimental data and physical considerations (eq. (5.15)). This equation is a function of pipe diameter, pipe angle, viscosity, surface tension and the air flow number and provides a more complete description than the available air pocket clearing velocity correlations. Equation (5.15) is derived from air-water experiments in pipes with varying internal diameter and from a limited number of experiments with reduced surface tension. Despite the fact that most experiments were carried out with air and water, equation (5.15) seems applicable to other fluid mixtures, although validation is recommended.

The maximum volumetric air-water discharge ratio without air accumulation is proven to be very small ( $\sim 0.001$ ). The accumulation of air pockets increases the air discharge exponentially, following eq. (5.11). If the water flow number is smaller than the clearing flow number, then the equilibrium gas pocket head loss follows a beta distribution function (eq. (5.9)).

More detailed modelling attempts should focus on the interaction between buoyancy and turbulent bubble transport in the blow-back flow regime with multiple hydraulic jumps as briefly discussed in section 5.5. An interesting challenge is the prediction of the number of consecutive air pockets and hydraulic jumps in a certain configuration.

The air transport model, presented in this paper may serve as validation data to extend the range of applicability of existing two-phase flow codes.

## 6 Detection of gas pockets

This chapter extends a conference paper, presented at the 10<sup>th</sup> International Conference on Pressure Surges in Edinburgh (Pothof and Clemens, 2008a).

### 6.1 Introduction

One of the main causes of a capacity reduction in pressurised wastewater mains is the presence of gas pockets in declining pipe sections. These gas pockets are not easily transported and become an obstruction for the water flow. During normal operation, an operator would like to have practical and simple tools at his/her disposal to determine which processes are causing a certain capacity reduction. Knowledge about the most likely cause of the capacity reduction — gas pockets or pipe wall scaling— supports the decision about the most effective measure to be taken.

This chapter proposes a gas pocket detection method that discriminates gas pockets from other causes of capacity reduction. The proposed detection method computes the first location with a gas pocket and assesses the total gas pocket volume in a dendritic pressurised pipeline system. The detection method takes a number of practical requirements into account.

### 6.2 Literature overview

The application of fluid transients for system or flow characterisation has been investigated since the 1990s. These investigations focus on leak detection in oil transportation lines (Liou, 1993), leak detection in water mains (Brunone, 1999; Ferrante and Brunone, 2003) and distribution networks (Liggett and Chen, 1994), multiphase flow measurement (Gudmundsson, 1999) and the determination of the valve status and identification of pipe blockages (Stephens, 2004).

Stoianov *et al.* (2003) identified a number of practical limitations and concluded that the use of transient and inverse transient analysis (ITA) would be “unlikely to have any value for the water industry”. Covas *et al.* have performed field tests to assess the practical applicability of transient (pressure) signals for the detection of leaks (Covas, 2004). Covas concludes that both time analysis and ITA were successful in the detection and location of



leaks of a ‘reasonable’ size. Stephens et al. have performed field tests to assess the practical applicability for the detection of leaks, air pockets and pipe blockage (Stephens et al., 2004). Stephens *et al.* conclude that ITA was successful in detecting an air pocket and less successful in detecting pipe blockage and leaks. ITA is a powerful tool to tune uncertain system parameters to a measured transient response, but ITA requires quite some specialist knowledge about transient solvers and efficient search strategies to adjust the uncertain parameters.

A pressure transient, induced by a rapid valve closure or pump speed reduction, reflects on the other side of a single pipeline and returns to the source, reflects again and leads to a periodic pressure time series at each location in the pipeline. The period of the oscillation depends on the type of boundary conditions and equals one or two pipe periods ( $P$ ), where the pipe period is defined as (Thorley, 2004):

$$P = \frac{2L}{c} \quad (6.1)$$

where  $L$  and  $c$  are the length of the pipeline the acoustic wave speed. The oscillation period,  $P_o = P$ , if the pipeline boundaries are both open (i.e. tanks or reservoirs) or both closed (i.e. closed valves). The oscillation period  $P_o = 2P$ , if one boundary is open and the other boundary is closed. The oscillation frequency  $f_0 = (P_o)^{-1}$  (in Hz) is the base frequency in the Fourier transform of a pressure time series, because the Fourier transform shows the frequency content of a data array, such as a time signal. Normally, the Fourier transform shows smaller peaks at integer factors of the base frequency – so-called higher harmonics. The literature, exploring ITA, focuses on very fast operations (i.e. manoeuvring time  $\ll$  pipe period), which is impractical or, at least, requires careful preparation.

Lubbers and Clemens (2005) have investigated the potential of transient pressures to detect the location of gas pockets in sewage water mains with a simpler method. Their method is based on an analysis of the Fourier transform of a measured pressure transient. This method predicts the location of a single gas pocket in a single pipeline with sufficient accuracy. The method is briefly summarized in section 3. The method was verified in a 630 m long test pipeline ( $\phi 235$  mm).

### 6.3 Gas pocket detection by frequency analysis

Lubbers (2007) has proposed a gas pocket detection method to determine the location of the first gas pocket in a single pipeline. The detection method is illustrated in Figure 6.1.

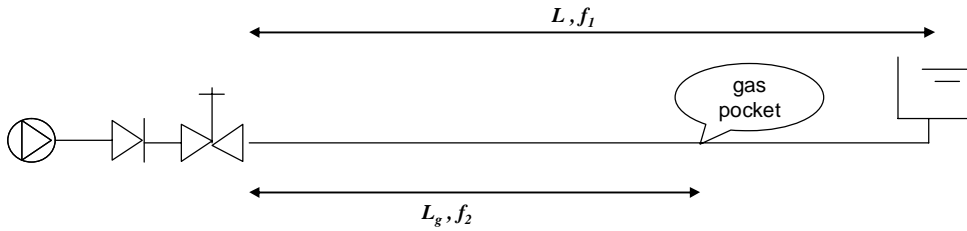


Figure 6.1: Method to determine first gas pocket location from measured frequency content

If a gas pocket is present, somewhere in a single pipeline, then a pressure transient will reflect on the gas pocket, because of the large compressibility of the gas pocket. The early reflection generates a shorter oscillation period and, therefore, a higher frequency  $f_2$  in the frequency domain. Lubbers (2007) has exploited the higher frequency during pump ramp down experiments to estimate the location of a gas pocket. Figure 6.2 shows a typical frequency graph derived from pump ramp down measurements in a 630 m test pipeline with a single gas pocket of known volume, trapped in a vertical stand pipe at different locations from the pump. The pressure traces, from which Figure 6.2 was derived, were measured 520 m from the pump, while the gas pocket was trapped at 394 m from the pump. Figure 6.2 shows two higher harmonics in the Fourier transform of the pressure trace without gas pockets (legend *air column = 0 cm*). The base frequency, without gas, is 0.0232 Hz, which corresponds with an acoustic wave speed of 290 m/s. It is noted that the lowest frequency drops as the gas pocket volume increases; this phenomenon will be exploited in the extended detection method. The higher frequencies around 0.42 Hz are caused by the gas pocket, although the exact location cannot be immediately derived from the measured frequencies, due to the complex influence of the running pump on the higher frequencies.

Therefore, a pump ramp down operation does not yield the most accurate estimate of the gas pocket location, because a running pump affects the frequency spectrum and therefore the gas pocket location estimate. If the pump ramp down leads to check valve closure, then the gas pocket location can be estimated more accurately. The subsystem between the check valve or discharge valve, where the transient is initiated, and the first gas pocket is responsible for generating a higher frequency peak  $f_2$ . The location of the first gas pocket,  $L_g$ , is obtained as:

$$L_g = \frac{c_0}{4f_2} \quad (6.2)$$

It is assumed in equation (6.2) that no free gas is present between the pumping station and the first gas pocket, so that the applicable acoustic wave speed is the reference wave speed without gas in the line,  $c_0$ .

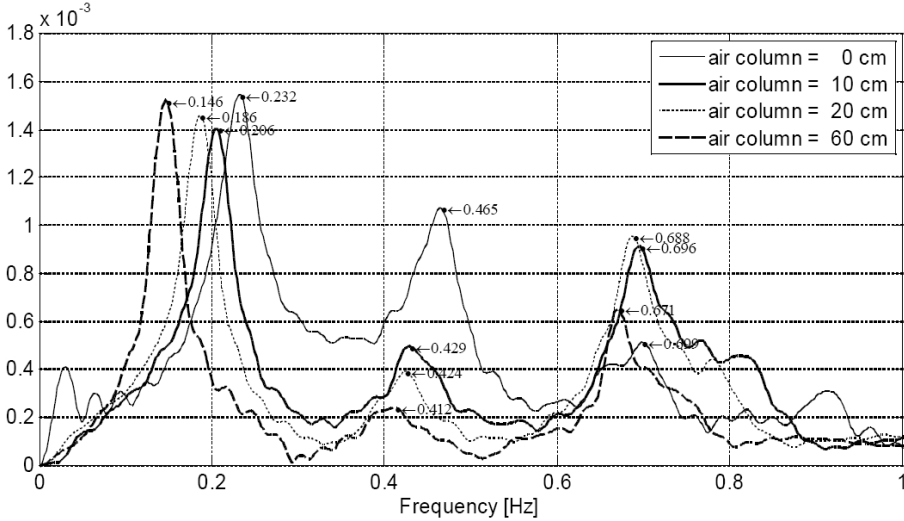


Figure 6.2: Fourier transforms of measured transient pressures in 630 m test pipeline (Lubbers, 2007a)

Lubbers' detection method (Lubbers and Clemens, 2005) is improved and extended to predict the gas pocket location and volume, because knowledge about the gas volume is required to assess the risk of a sudden capacity reduction at increased flow rates. The method is further extended to handle branched systems and systems with multiple gas pockets, because these are more common in practice.

#### 6.4 Gas pocket volume and frequency drop

The frequency drop due to a gas pocket will be fully understood after some properties of the wave speed have been discussed. The wave speed appears in the continuity equation.

$$\frac{\partial v}{\partial s} + \frac{g}{c^2} \frac{\partial H}{\partial t} = 0 \quad (6.3)$$

where

$$\frac{1}{c^2} = \rho \left( \frac{1}{K} + \frac{1}{A} \frac{dA}{dp} + \frac{1}{\Delta s} \frac{d\Delta s}{dp} \right) = \rho \left( \frac{1}{K} + \frac{D}{eE} \right) \quad (6.4)$$

Herein,  $v$ ,  $s$ ,  $H$ ,  $t$ ,  $K$ ,  $p$ ,  $\Delta s$ ,  $e$  and  $E$  are the cross sectional liquid velocity, distance in longitudinal direction, piezometric head relative to a reference plane, time, liquid bulk modulus, pressure, pipe element elongation, wall thickness and the pipe Young's modulus.

The more fundamental expression of the acoustic wave speed in equation (6.4) shows that the wave speed represents all possible internal elastic storage contributions, i.e. elastic storage due to fluid compressibility and radial and axial pipe expansion. The larger the elastic storage, the smaller the acoustic wave speed.

A gas pocket is an extra source of elastic storage that reduces the average wave speed in the pipeline and consequently reduces the base frequency. The larger the gas pocket, the larger the storage and the smaller the base frequency. Hence the reduction of the base frequency potentially is a measure for the gas pocket volume.

Now, a relation is established between the total gas volume in the main line of a dendritic system and the average wave speed in the main line. The main line of a dendritic system comprises the series of pipes from the main pumping station to the downstream boundary condition. The elastic storage is conveniently expressed as a storage area, which is directly derived from the continuity equation:

$$\mathcal{A}_0 = \frac{\Delta V}{\Delta H} = \frac{g \cdot V_L}{c_0^2} \quad (6.5)$$

where  $\mathcal{A}$ ,  $V_L$ ,  $c$  are the elastic storage area, system volume in the main line and average wave speed in the main line. The subscript 0 refers to the reference condition without gas pockets and subscript 1 will refer to a condition including one or more gas pockets in the main line. The storage area, associated with an initial gas pocket of volume  $V_i$ , is derived from the following thermodynamic relation:

$$p \cdot V^k = C \quad (6.6)$$

where  $p$ ,  $V$ ,  $C$ ,  $k$  are the absolute gas pocket pressure, the gas pocket volume, a thermodynamic constant and the polytropic coefficient. In order to derive an expression for the storage area, the absolute pressure is replaced by

$$p = \rho_w \cdot g \cdot h_a \quad (6.7)$$

such that

$$V = \left[ C / (\rho_w \cdot g \cdot h_a) \right]^{1/k} \quad (6.8)$$

A second order Taylor expansion of equation (6.8) around a certain final gas pocket volume  $V_f$  and absolute piezometric head  $h_{a,f}$  yields (Figure 6.3)

$$V - V_f = \frac{-V_f}{k \cdot h_{a,f}} (h_a - h_{a,f}) + \frac{V_f}{(k \cdot h_{a,f})^2} \frac{1+k}{k^2} (h_a - h_{a,f})^2 + o(h_a - h_{a,f})^2 \quad (6.9)$$

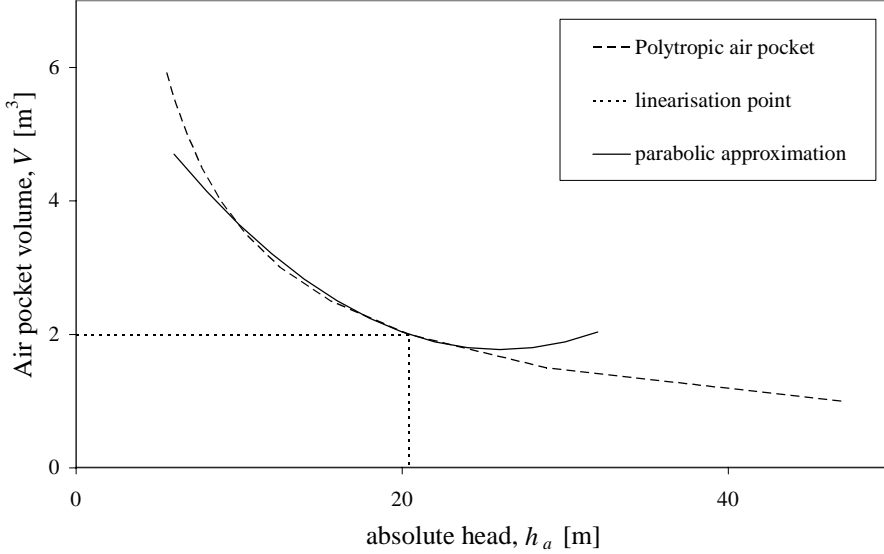


Figure 6.3: Parabolic approximation of the thermodynamic behaviour of a gas pocket

The average internal storage area of the gas pocket  $\mathcal{A}_1$  is found by dividing equation (6.9) by the gas pocket pressure amplitude  $h_{a,max} - h_{a,f}$

$$\mathcal{A}_1 = \frac{-\Delta V}{\Delta h} = \frac{V_f - V}{h_a - h_{a,f}} = \frac{V_f}{k \cdot h_{a,f}} - \frac{V_f}{(k \cdot h_{a,f})^2} \frac{1+k}{k^2} (h_{a,max} - h_{a,f}) \quad (6.10)$$

If the last term is negligible, for example if the gas pocket is large and the air pocket pressure amplitude is small, equation (6.10) reduces to the first order approximation of the gas pocket behaviour. The extra parameter, the gas pocket pressure amplitude, makes a more accurate assessment of the internal storage area  $\mathcal{A}_1$  possible. Since the gas pocket pressure amplitude cannot be assessed a priori, a more accurate gas pocket volume estimate is not readily available. Nevertheless, the 2<sup>nd</sup> order approximation of the storage area  $\mathcal{A}_1$  provides a mechanism to determine the range of possible values of the gas pocket volume. The maximum pressure amplitude at the location of the gas pocket would occur for a (very) small gas pocket volume; this maximum pressure amplitude could be obtained from the simulation without air pockets.

Another remark must be made on the parabolic approximation. The accuracy of the parabola deteriorates strongly beyond the minimum point of the parabola, as illustrated in Figure 6.3. The minimum of the parabola leads to a requirement on the maximum gas pocket pressure amplitude:

$$h_{a,\max} - h_{a,f} < \frac{k \cdot h_a}{2(1+k)} \quad (6.11)$$

Having made these remarks, the total elastic storage area in the system with gas pockets is simply the sum of all elastic storage areas, yielding an average wave speed,  $c_1$ , in the main line, which obeys the following expression:

$$\frac{1}{c_1^2} = \frac{1}{c_0^2} + \frac{\mathcal{A}_1}{g \cdot V_L} \quad (6.12)$$

The average wave speed in equation (6.12) corresponds to a certain base frequency in the frequency domain. The base frequency of the main line is determined from the length of the main line, the average wave speed and the boundary type, as discussed above:

$$\text{Different boundaries} \quad f_1 = \frac{c_1}{4L} \quad (6.13)$$

$$\text{Similar boundaries} \quad f_1 = \frac{c_1}{2L} \quad (6.14)$$

Literature has shown that different boundaries yield better predictions of the gas pocket location. Therefore, the remainder of this chapter focuses on base frequencies with different boundary conditions, following equation (6.13). The total gas pocket volume is computed from a certain frequency reduction by combining equations (6.10), (6.12) and (6.13).

$$\text{First order estimate} \quad \frac{V_f}{V_L} = \frac{g}{16L^2} \left( \frac{1}{f_1^2} - \frac{1}{f_0^2} \right) k \cdot h_{a,f} \quad (6.15)$$

$$\text{2}^{\text{nd}} \text{ order estimate} \quad \frac{V_f}{V_L} = \frac{g}{16L^2} \left( \frac{1}{f_1^2} - \frac{1}{f_0^2} \right) \left[ \frac{(k \cdot h_{a,f})^2}{k \cdot h_{a,f} - (1+k)(h_{a,\max} - h_{a,f})} \right] \quad (6.16)$$

Equation (6.15) or (6.16) couples the base frequencies with and without air pockets, so that the observed frequency reduction determines the total gas pocket volume in the pipeline, irrespective of the number of individual gas pockets. The presence of the branches and the branch flows are reflected in the base frequency of the reference transient,  $f_0$ . The higher frequency response will still predict the location of the first gas pocket. If gas is distributed along the pipeline, then the higher frequency peak will be absent, which will be demonstrated in a numerical example in section 6.6.3. Section 6.5 will first detail the

extended gas pocket detection method and discuss practical aspects of the detection method.

## 6.5 Extended detection method

### 6.5.1 Detection procedure

The extended detection method is summarised in the following steps:

- 1 Build a simulation model of the pressurised dendritic wastewater system, and include sufficient information for transient simulations. This model is preferably validated against field data without gas pockets in the system in order to verify that the simulation model captures the reference frequency correctly, which mainly requires correct information on the system lengths and pipe materials.
- 2 If the transient is initiated from a pumping station, then all anti-surge devices must be disabled in the model – and later in the field as well. The impact of the transient event without anti-surge devices must be verified to prevent damage to the system.
- 3 The transient must be generated by an upstream valve closure or pump trip with check valve closure. The transient is preferably initiated from the largest upstream pumping station. Determine in the simulation model which maximum initial flow rate and which transient can be imposed on the system (e.g. pump trip or discharge valve closure) without violating the incidental pressure criteria. Cavitation should be prevented, because cavities generate similar reflections as gas pockets<sup>\*)</sup>. This is the reference case.
- 4 Install a pressure transducer in the main line at an accessible location, where pressure oscillations will occur during the transient, which can be verified in the reference case. Generally, the only above-ground piping is in the pumping station. In this case, the pumping station's check valves must close or the discharge valve must close and the pressure must be recorded downstream of these valves. Otherwise the transducer will record the suction level shortly after the beginning of the transient event.
- 5 Initiate the transient event in the real system and record the transient pressure. The sample frequency must be greater than 10 times the base frequency of the simulated system.

---

<sup>\*)</sup> *The transient event must be balanced between two competing criteria. On one hand, the transient must be as strong as possible to maximise the information content in the pressure signal. On the other hand, the transient event should not cause cavitation, de-aëration or pipe damage. Rapid de-aëration in water starts at about 5 metres above vapour pressure.*

- 6 Extend the time series to the next integer power of 2 values with the average value of the complete time series. One reason for this step is to benefit from the most efficient implementation of the Fast-Fourier-Transform (FFT). A second reason is to improve the accuracy of the peak frequency; if the array is doubled in length, then the frequency resolution becomes twice as small. A third argument is that some tools, like Microsoft Excel, only support FFT arrays with this length requirement, because they only have implemented the most efficient FFT algorithm. The second argument is the most relevant, because the base frequency is relatively low and drops further if gas pockets are present. Some guidance is provided by the fact that the frequency resolution,  $\Delta f$ , equals  $1/T$ , where  $T$  is the covered time of the extended time series.
- 7 Remove the trend, if present, from the measured and calculated pressure signals in order to obtain an optimal resolution at the smallest frequencies.
- 8 Determine the FFT of the measured pressure signal and the simulated pressure signal at the same location. The FFT routine is widely available in, for example, the default Data analysis Add-in from Microsoft Excel, in Matlab and in practically all other time series analysis packages. The FFT is a series of complex numbers with resolution  $\Delta f$ , from which the absolute values are further processed.
- 9 Plot the FFT arrays and determine the largest frequency in each array. Furthermore determine the second largest frequency in the measured array. The two frequencies should differ less than 1 order of magnitude. The largest frequency in the reference FFT is  $f_0$ , the largest and second largest measured frequency are  $f_1$  and  $f_2$ , as illustrated in Figure 6.1.
- 10 Apply equation (6.2) to estimate the location of the first gas pocket.
- 11 Determine the absolute final pressure,  $p_f$ , at this location from the reference simulation.
- 12 Apply equation (6.15) or (6.16) to obtain a range of estimates of the total gas volume. After all parameters have been set, the result is the total gas volume, from which a fraction is present around location  $L_g$ .

It is assumed that the main line is easily identified in a dendritic wastewater transportation system. One or more branches link onto the main line. The dendritic system has a base frequency, depending on the properties of the main line and the branches in a complicated way. This base frequency cannot be accurately assessed from analytical calculations, but is easily obtained from a numerical simulation of a reference case without gas pockets during a suitable harmless transient. The simulated reference transient must be harmless, because the same transient must be induced in the real system in order to detect the presence of gas pockets. The preferred initial situation for this detection method in a dendritic wastewater system is the situation without flow from the pumping stations, except for the pumping station where the reference transient is initiated. Such an initial state can be created



(automatically) during the night, if no severe rainfall is expected. The simulated and measured signals are Fourier transformed, using the Fast Fourier Transform (FFT), to determine the frequency content of the signals.

### 6.5.2 Parameters for gas pocket volume estimate

Before equation (6.15) or (6.16) can be applied to compute the total gas pocket volume, the parameters must be estimated, which is not trivial in a dendritic system. These parameters – the polytropic coefficient  $k$ , characteristic system volume  $V_L$  and length  $L$  and final piezometric gas pressure  $h_{a,f}$  – will be discussed hereafter.

The polytropic coefficient,  $k$ , is in fact not a real constant, but this parameter depends on transient heat fluxes to and from the gas pocket and the gas pocket composition, which is hardly predictable in practice. Gas pockets may include methane, carbon dioxide, nitrogen and hydrogen sulfide in varying concentrations. A polytropic coefficient of 1.0 corresponds with isothermal gas pocket behaviour, a value of 1.4 corresponds with adiabatic behaviour, if the gas pocket composition is similar with air. If the gas pockets have a large methane or carbon dioxide content, then the maximum value reduces to 1.35 or 1.28 respectively. A reasonable estimate of the polytropic coefficient is 1.2 for a fast manoeuvre and 1.0 for a slow manoeuvre. A sensitivity analysis over the range of possible values of the polytropic coefficient provides insight in its impact on the gas pocket volume prediction.

The characteristic system length  $L$  is the length from the main pumping station to the downstream boundary condition. The characteristic system volume  $V_L$  is the pipeline volume from the main pumping station to the downstream boundary condition. The length and volume of the side branches are thus neglected.

The piezometric head parameter,  $h_{a,f}$ , represents the absolute final piezometric head in the gas pocket(s) at the end of the reference scenario. The numerical reference scenario provides detailed information on all final pressures along the main line. If the system includes considerable elevation differences, then the final pressures may differ significantly along the line.

The second frequency peak of the measured pressure can be used to locate the gas pocket and to set the head parameter  $h_{a,f}$ . The determination of the gas pocket location is independent of the pressure parameter.

## 6.6 Feasibility of the extended detection method

As a first test of the practical applicability of the detection method, the method is applied to the single pipe system ( $L = 2960$  m,  $c = 1021$  m/s, with a single gas pocket at 2035 m) in a numerical experiment with gas pockets of different sizes. All transient simulations have been performed with WANDA, version 3.60 (Deltares, 1993 - 2008). The detection method systematically underestimates the actual location and gas pocket volume (Figure 6.4), if the volume estimate is based on the first order gas pocket volume estimate. The second order gas pocket volume estimate in Figure 6.4 is based on an assumed gas pocket head amplitude of 30% of the observed head amplitude in the pumping station. The second order approach provides a mechanism to obtain a reasonable range of gas pocket volumes. The predicted location varies from 75% to 99% of the real location. The predicted volume varied between 51% and 104% of the real volume. These results are considered practically relevant.

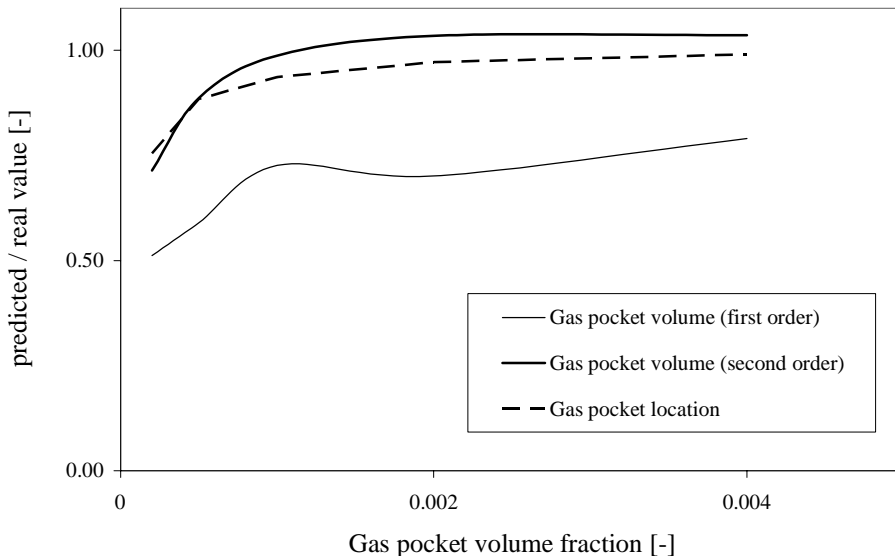


Figure 6.4: Prediction performance of the extended detection method in a single pipeline; the second order volume estimate is based on an estimated gas pocket head amplitude of 30% of the observed head amplitude in the pumping station. The polytropic coefficient was set to  $k = 1.2$ .

The feasibility of the described detection method is further verified in a system with one side branch. The ‘measurements’ are generated numerically with one, two and many gas pockets at unknown locations in the main line.

### 6.6.1 Reference transients and gas pocket transients

The key properties of the test system are listed in Table 6.1 and on the lay-out in Figure 6.5.

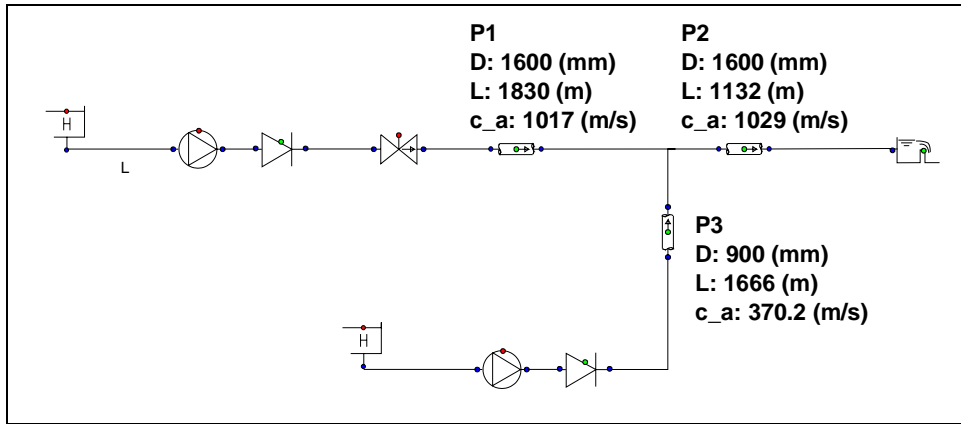


Figure 6.5: Lay-out of test system and relevant pipe properties (diameter, length, wavespeed)

Table 6.1: Overview of test system pipe properties

Pipe	Diameter [mm]	Length [m]	Volume [m <sup>3</sup> ]	Wave speed [m/s]	Pipeline period [s]
P1	1600	1830	3679	1017	3.6
P2	1600	1132	2276	1029	2.2
Total main	1600	2962	5955	1022	5.8
P3 (branch)	900	1666	1060	370	9.0

The operational conditions of the reference transients consist of the closure of the discharge valve from a suitable, harmless, steady state flow. The valve closure can be rapid (effective closure in 3 s) or slow (effective closure in 10 s); the pipeline period is 6.6 s. The initial velocity for the 3 s valve closure scenario is about 10% of the design velocity. The flow from the side branch is set to the design flow rate or to zero. These parameter combinations yield 4 different reference transients, which are summarized in Table 6.2 below.

Table 6.2: Overview of operational conditions of reference transients in test system

Reference cases	Initial velocity main [m/s]	Closure time [s]	Initial velocity side [m/s]
3s branch flow	0.18	3	1.7
3s no branch flow	0.18	3	0
10s branch flow	0.36	10	1.7
10s no branch flow	0.36	10	0

The simulated transient pressures, downstream of the discharge valve, in two reference cases are depicted in Figure 6.6 hereafter. Figure 6.6 clearly illustrates that a branch in operation dampens the transient signal considerably. The damping will be stronger in practice, because unsteady friction has not been included in these simulations. It is anticipated that pressure damping due to unsteady friction does not affect the frequency analysis discussed in this paper. The frequency contents of the four reference transients are shown in Figure 6.7 hereafter, showing more pronounced peaks if the branch is switched off. The frequency peaks are listed in Table 6.3.

Table 6.3: Frequency peaks of the reference scenarios

Scenario	Low frequency peak [Hz]	2 <sup>nd</sup> peak [Hz]
3s branch flow	0.076	0.120
3s no branch flow	0.044	0.093
10s branch flow	0.076	0.120
10s no branch flow	0.044	0.093

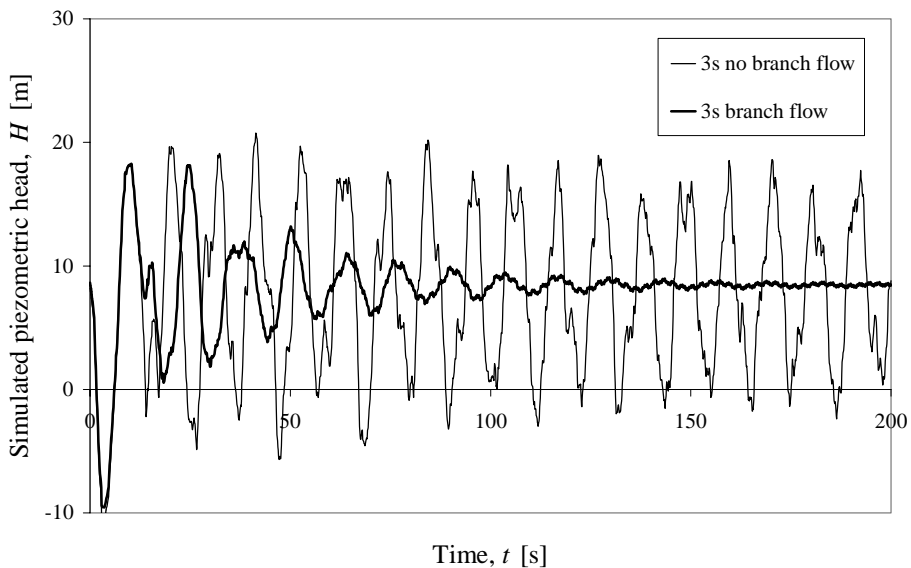


Figure 6.6: Transient pressures of 3 s valve closures (reference cases)

Inspection of Figure 6.7 immediately shows that the peak frequencies do not depend on the rate of the valve closure; even a 20 s valve closure shows the same frequency peaks. The frequency plot of the reference transients with the branch pumping station in operation shows two distinct peaks at 0.076 Hz and 0.12 Hz. If the branch pumping station is

switched off, then the frequency plot shows the two largest peaks at 0.044 Hz and 0.093 Hz; these plots contain some other smaller peaks at 0.16 Hz, 0.24 Hz and 0.31 Hz.

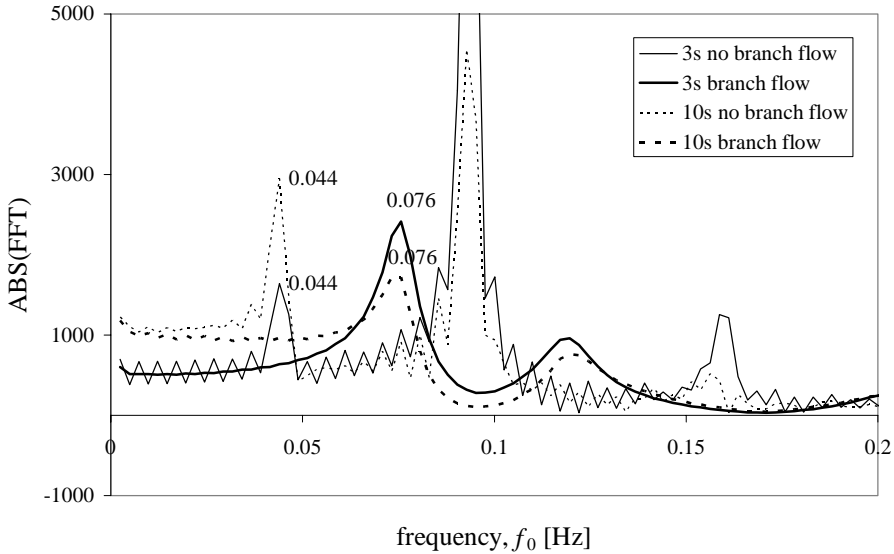


Figure 6.7: Frequency content of the reference transients (lowest frequencies)

### 6.6.2 Gas pocket transients

The transient pressure ‘measurements’ with gas pockets in the system have been generated numerically. The total gas pocket volume is  $6 \text{ m}^3$  for all scenarios, which corresponds with 0.1% of the volume of the main pipeline. Gas pocket transients have been generated with a single gas pocket, two smaller gas pockets or gas distributed along the main line. The detailed specifications of the gas pocket volume and location(s) are listed in Table 6.4. The individual gas pockets were modelled in WANDA with equation (6.6) that models the expansion and compression of the gas pockets correctly. The distributed gas was modelled as an initial gas fraction, modelled according to equation (6.6) at almost every internal calculation node along the pipeline.

Table 6.4: Specification of gas pockets

Scenario	# gas pockets [-]	volume [ $\text{m}^3$ ]	location [m]	Notes
1gas	1	6	2035	location is 205 m after junction
2gas	2	3 3	1625 2035	locations are 205 m before and after the junction
distr.gas	distributed	6	distributed	equally distributed

Three different gas pocket specifications and four operational conditions yield a total of twelve cases with gas pockets. Furthermore, one case has been included with reduced main diameter and increased wall roughness, in order to verify a clear distinction between gas pockets and other causes of capacity reduction. The wall roughness was increased by a factor 5 (to 1 mm) and the internal diameter was decreased by 5% (to 1520 mm). The operational condition was a 3 s valve closure with side flow. The roughness increase and diameter reduction caused a 50% increase of the hydraulic grade line and a marginal reduction of the flow rate of about 1%. The capacity reduction is marginal, because the discharge valve dominates the total head drop in the main line and the flow velocity in the common pipe after the junction is relatively small, because the main pumping station is running at 10% of its capacity only during these transients.

### 6.6.3 Gas pocket predictions

As an example, the FFTs of all valve closure scenarios are shown in Figure 6.8. The scenarios with gas in the main line clearly show lower base frequencies, while the scenario with wall scaling (label friction, no gas) shows the same base frequency as the reference scenario, which correctly indicates that the total gas volume is zero for the scenario with wall scaling, following equation (6.15). Furthermore, the frequency of the second peak of the scenario with two gas pockets at 0.18 Hz is greater than the frequency of the second peak of the one gas pocket scenario at 0.14 Hz, which is at least qualitatively consistent with the scenario parameters, because the first gas pocket is located more closely to the pumping station. Finally, the second peak of the distributed gas scenario is about one order of magnitude smaller than the first and occurs at the double frequency of the first peak, which indicates that this scenario has no clearly located gas pocket and therefore the gas must be distributed. Table 6.5 summarizes the quantitative results.

The following conclusions on the gas pocket location are drawn from Table 6.5. If the gas is concentrated in one pocket, then the predicted location is within 140 metres of the correct location (2035 m). If the gas is distributed in two gas pockets, then the location is underestimated by 200 metres. If the gas is distributed along the main line, then a second frequency peak is hardly visible; only the second harmonic frequency could be interpreted as such. In the latter case, the predicted location exceeds the pipe main length considerably (by more than 30% of the pipe main length). Hence, if a second frequency peak is not visible or the predicted length exceeds the total length and the predicted volume is non-zero, then the gas must be distributed along the main line.

Table 6.5: Predicted gas pocket location and volume; volume is based on first order estimate in eq. (6.15)

Scenario	Low frequency peak [Hz]	2 <sup>nd</sup> peak [Hz]	Predicted location [m] (actually at 1625 m and/or 2035 m)	Predicted volume [m <sup>3</sup> ] (actually 6 m <sup>3</sup> )	Remarks
Branch flow, 3 s valve stroking time					
One gas pocket	0.0439	0.1318	1940	3.5	
Two gas pockets	0.0391	0.1782	1430	4.8	
Distributed gas	0.0366	N/A	N/A	5.8	
Friction, no gas	0.0757	0.1196	2140	0	
Branch flow, 10 s valve stroking time					
One gas pocket	0.0439	0.1318	1940	3.4	
Two gas pockets	0.0391	0.1782	1430	4.8	two other peaks present
Distributed gas	0.0342	0.0708	N/A	5.7	
No branch flow , 3 s valve stroking time					
One gas pocket	0.0350	0.1343	1900	3.0	
Two gas pockets	0.0342	0.1782	1430	3.3	
Distributed gas	0.0317	0.0635	4020	4.7	2 <sup>nd</sup> peak is 2 <sup>nd</sup> harmonic
No branch flow , 10 s valve stroking time					
One gas pocket	0.0342	0.1343	1900	3.3	
Two gas pockets	0.0317	0.1782	1430	4.6	
Distributed gas	0.0293	0.0610	4190	6.3	

If the manoeuvre is faster than the pipe period, then the second frequency peak, caused by the reflection on the gas pocket, is the largest peak in the FFT. This observation is illustrated in Figure 6.8, where the scenarios (3 s, branch flow, 1 gas pocket) and (3 s, branch flow, 2 gas pockets) have their maximum magnitudes at the second frequency peak. If, however, the manoeuvre is slower than the pipe period, then the maximum FFT values occur at the base frequency peak.

The following conclusions on the gas pocket volume are drawn from Table 6.5. The scenario, in which the capacity reduction was caused by a diameter reduction and pipe roughness increase, correctly shows a total gas volume of 0 m<sup>3</sup>, because the base frequency equals the base frequency of the reference scenario. The total gas volume is more accurately predicted, if the gas volume is more distributed along the line. The predicted gas

volume error is about 50%, if there is only one gas pocket in the pipeline, and better than 20% if the gas is distributed along the line. Hence the order of magnitude of the total gas pocket volume is predicted reasonably well. The prediction results are not significantly better for the scenarios with a stationary flow from the branch as was anticipated in section 6.6.1. The predictions of the fast closure scenarios are as good as the predictions of the slow closure scenarios.

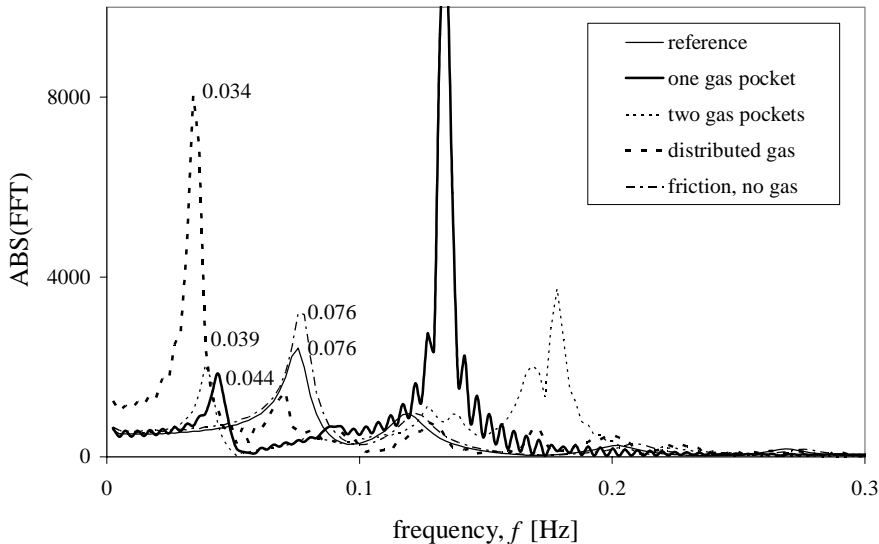


Figure 6.8: Frequency content of 3 s valve closure transients with branch flow

## 6.7 Field measurement

On August 20<sup>th</sup> 2008, a one day field measurement was carried out near Ochten, Netherlands, to verify the practical feasibility and accuracy of the detection method.

### 6.7.1 System description

The pressurised wastewater transportation system IJzendoorn – De Heuning – Ochten is located between two of the major rivers in the Netherlands: the Rhine and the Waal (Figure 6.9). The system is owned and operated by waterboard ‘Rivierenland’. The sewerage system in De Heuning is a separated system, the system in IJzendoorn is a combined sewerage system. The system scheme is depicted in Figure 6.10. The design flow rates from De Heuning and IJzendoorn are 75 m<sup>3</sup>/h and 30 m<sup>3</sup>/h, yielding a maximum discharge of 105 m<sup>3</sup>/h in the main line to Ochten. De Heuning pumping station ties into the main line with a short 25 m connecting pipe.



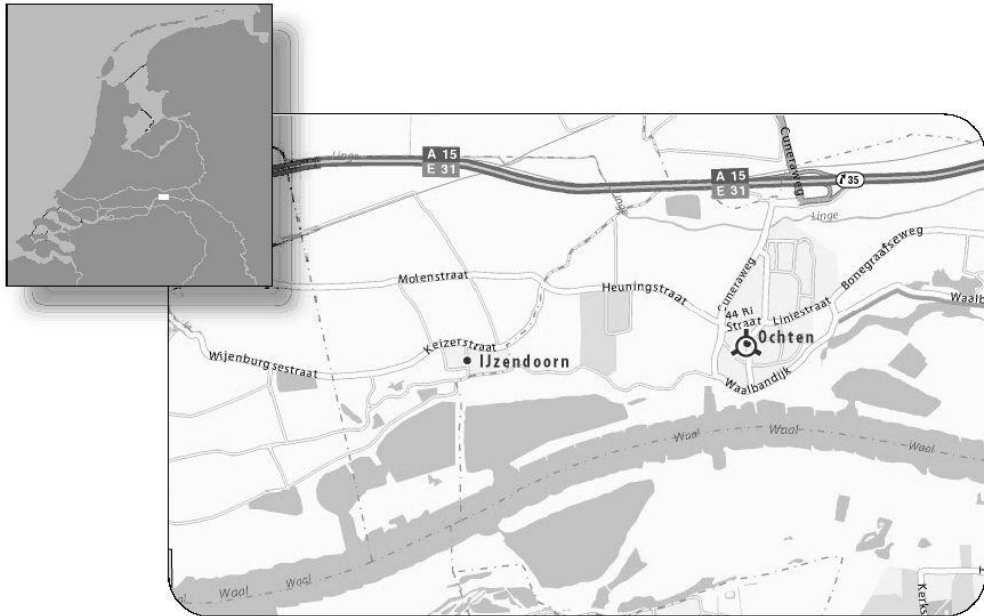


Figure 6.9: Map of IJzendoorn-Ochten area

The pipeline from IJzendoorn to De Heuning ( $L = 1330$  m,  $D = 0.116$  m) contains 9 small inverted siphons with elevation differences from 0.5 m to 1.3 m. The pipeline from De Heuning to Ochten ( $L = 2940$  m) is mostly constructed from PVC ( $D = 0.235$  m) and from HPE ( $D = 0.220$  m) for the 5 inverted siphons, having elevation differences from 2 m to 4 m. The design discharge corresponds with a maximum design Flow number of 0.52 in the HPE inverted siphons, which implies that the pipeline is susceptible for air accumulations. The pipeline profile and steady state head profile are depicted in Figure 6.11. Two isolation valves, which are normally open, are present near the connection point. Both pumping stations are equipped with a local flow control system. The downstream boundary condition is a free-falling jet into the Ochten sewerage system.

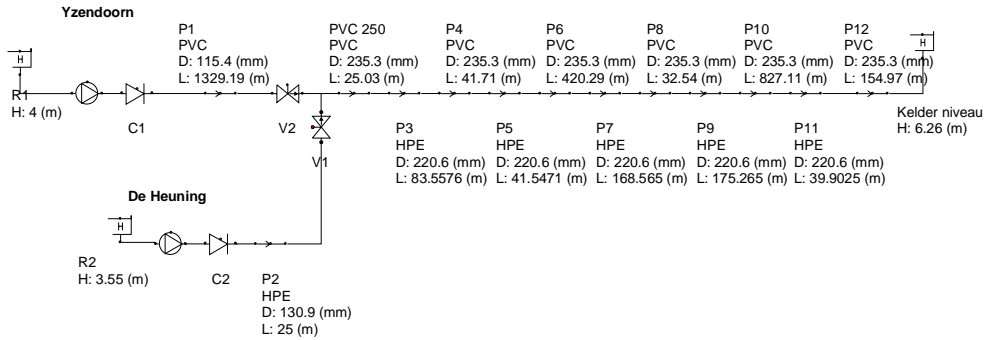


Figure 6.10: Overview of system for detection method field verification.

This system was selected, because experiments in a single pipe system and a simple branched system could be performed by closing or opening valve V2 at the connection point.

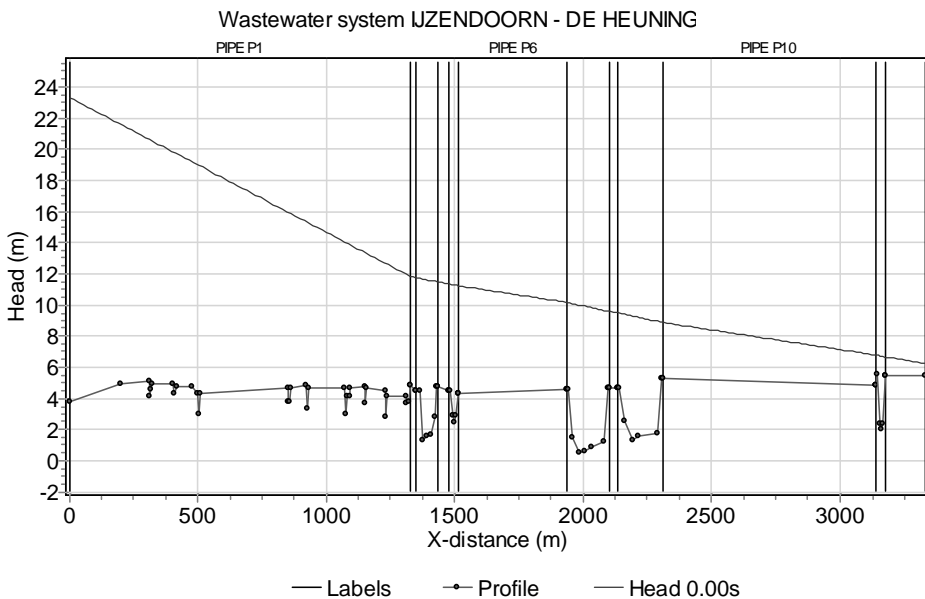


Figure 6.11: Pipeline and head profile at design flow rates from IJzendoorn and De Heuning ties in after 1330 m.

### 6.7.2 Preparations for transient measurements

The verification of the transient detection method requires a pressure transient with a pronounced frequency. WANDA was used to determine the most appropriate manoeuvre. A pump trip proved infeasible, because the pump and system inertia would keep the check valve open for a significant period of time. The manoeuvre had to be initiated by closing isolation valve V1 (in PS De Heuning). The pressure sensor should be connected downstream of this isolation valve.

The maximum discharge from De Heuning was determined without transient cavitation after the closure of valve V1. If valve V2 is shut (single pipe), the maximum allowable discharge from De Heuning is 60 m<sup>3</sup>/h, otherwise the maximum allowable discharge is 30 m<sup>3</sup>/h only. The reason for the lower discharge limit is the negative reflection on the closed discharge valve in IJzendoorn.

A full stroke of the manually operated valve V1 requires 12.5 revolutions. The valve was set at 3.5 revolutions open to obtain a sufficiently fast closure within 10 s, while limiting the valve resistance.

### 6.7.3 Data acquisition

Absolute pressure transducers (range 0 – 3 bara) were installed at known elevations at the beginning of the discharge line in the pumping station. The simultaneous acquisition of the discharge signal proved infeasible, because the splitting of the electronic signal disturbed the PLC, so that the pump stopped after 60 s. Therefore, the steady state discharges were manually logged from the PLC display. The steady state discharge is essential for the safe execution of the detection method. The target discharge was set by the operator, after which the PLC adjusted the pump speed to the discharge. Each transient measurement, recorded at 100 Hz, is preceded by a steady state measurement, recorded at 2 Hz during at least 5 minutes, to verify that a proper steady state was reached (Figure 6.12).

After the problem with the automatic discharge logging had been solved by switching to manual logging of the discharge, the following experiments were carried out:

- 1 Steady state measurements at 30 m<sup>3</sup>/h (Tiel002), 40 m<sup>3</sup>/h (Tiel007), 60 m<sup>3</sup>/h (Tiel004) and 70 m<sup>3</sup>/h (Tiel009), prior to the transient measurements.
- 2 Transient pressure measurement with isolation valve V2 closed (Tiel003) and (Tiel005).
- 3 Transient pressure measurement with isolation valve V2 open (Tiel008) and (Tiel010)

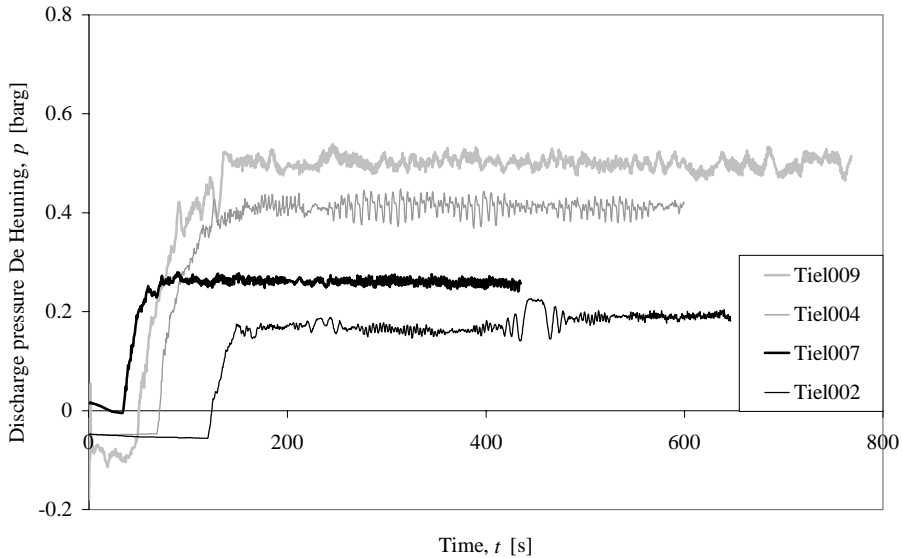


Figure 6.12: Pressure evolution to the steady states, filtered to a 5 s moving average.

The steady measurements were compared with a head loss calculation, showing a 30% greater pump head than expected, which is an indication for the presence of capacity reducing gas pockets. The first transient measurement revealed the presence of a large air pocket, so that further measurements could be carried out at larger discharges.

#### 6.7.4 Analysis of transient pressure measurements

The transient pressure measurements are presented in Figure 6.13 (500 s) and Figure 6.14 (first 30 s). The largest period in the pressure signal is in the order of 100 s; measurement *Tiel010* was stopped only after 1000 s, but the oscillation was too weak to clearly identify the lowest frequency. Figure 6.14 shows that the noise immediately disappears after the valve is closed and the pump is stopped. The Fourier transform is applied to the pressure measurement between 6 s and 30 s, after detrending the pressure signals in this time window. The high frequency peak determines the location of the first gas pocket.

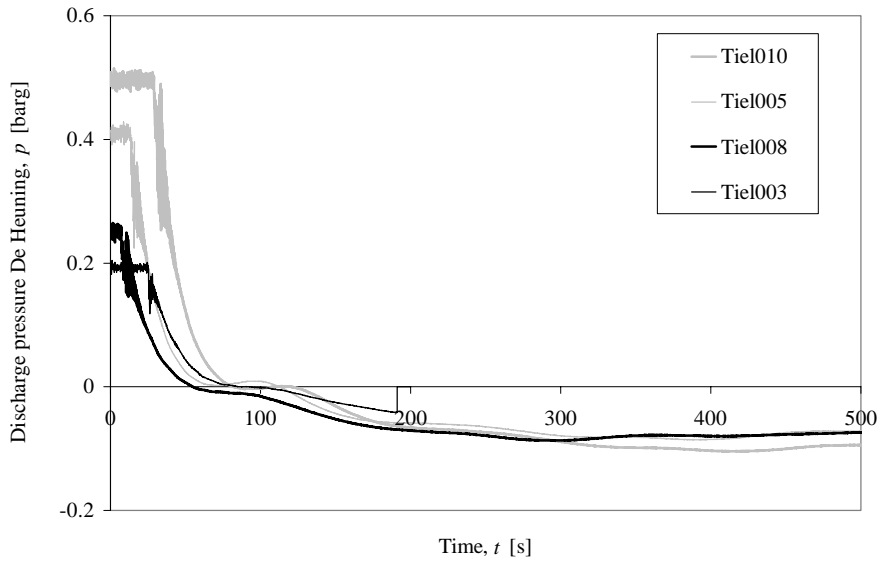


Figure 6.13: Transient pressure measurements in pumping station De Heuning

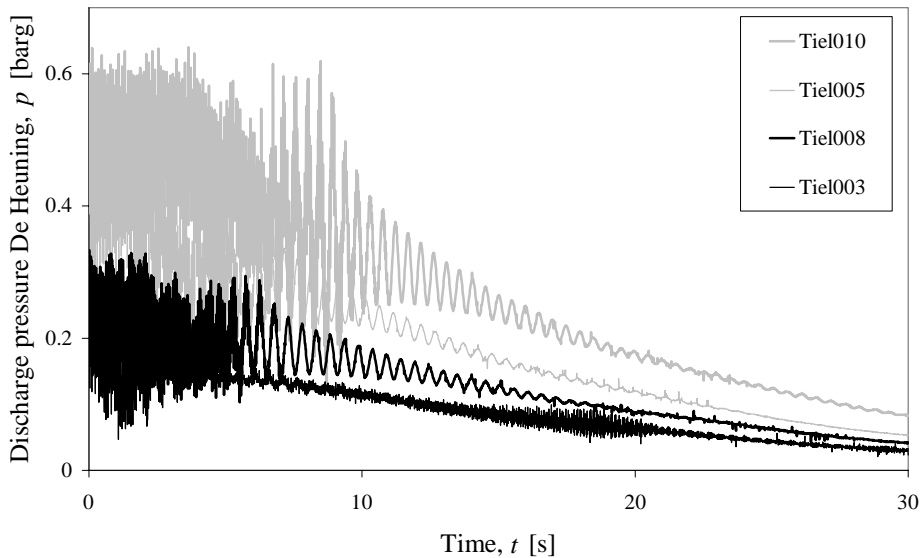


Figure 6.14: First 30 s of the pressure transients in pumping station De Heuning

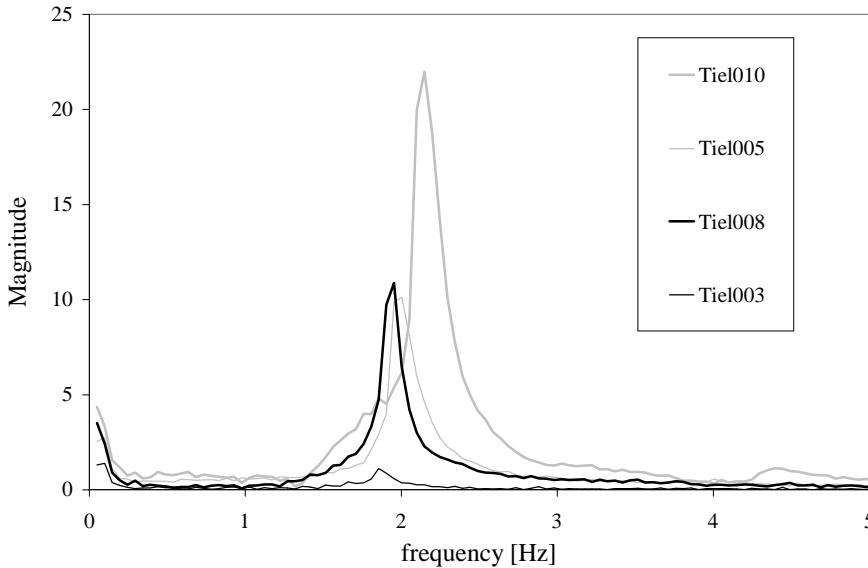


Figure 6.15 : Frequency spectrum of the de-trended pressure transients

The dominant frequency in Figure 6.15 is 2 Hz, which corresponds with a distance of 38 m to the first gas pocket;  $L = c / (4 * f)$ ,  $c = 300$  m/s in the PVC pipe. The first inverted siphon was indeed located after 38 m with a downward pipe angle of  $10^\circ$  and an elevation difference of 3.2 m.

Visual inspection of the complete time series reveals a period of approximately 115 s. the corresponding frequency of 0.0087 Hz is too small to be discriminated by the Fourier transform. Application of equation (6.15) yields a total gas pocket volume of  $2.2 \text{ m}^3$ . This volume exceeds the aggregated volume of all 5 downward sloping sections in the main line between De Heuning and Ochten, which seems feasible with the low flow numbers at which the pipeline is operated. The presence of air pockets in the inverted siphons was confirmed by the operators from a pigging procedure, performed after the field measurement.

## 6.8 Conclusions and recommendations

A relatively simple gas pocket detection method, compared to ITA, has been described and its feasibility has been addressed. The detection method investigates the frequency content of a measured or computed reference transient pressure signal without gas pockets and compares this frequency content with the frequency content of the measured transient pressure signal from the system, which may contain one or more gas pockets. The proposed

method predicts both location and total gas volume in the main line. The feasibility of the method has been verified numerically in a test system with one large branch. The feasibility investigation has shown that the location can be predicted with an error smaller than 200 m, while the length of the wastewater main is about 3000 m. The total volume prediction differs less than 50% of the actual gas volume, with a tendency to underestimate the volume, if a first order volume estimate is used.

A second order volume estimate makes the assessment possible of a range of gas pocket volumes. It is concluded from this limited investigation that the proposed detection method has the potential to estimate the location of the first gas pocket and the total gas volume with sufficient accuracy for practical applications.

If the transient scenarios are developed in such a way that the valves in the main pumping station close, then the transient pressure can be measured simply in the main pumping station downstream of the closing (check) valve, which is generally a location with easy access.

Despite the fact that more energy is dissipated, if the branch is switched on, the frequency plot with the branch in operation contains sufficient information for the detection method. Hence, the branch pumping stations can be operated normally during a transient detection test, initiated from the main pumping station. This investigation does not conclude that certain operational conditions for the branch pumping stations are recommended or required.

The duration of the transient event is not critical for the quality of the predictions. The 3 s operations and 10 s (or 20 s) operations yield similar results, while the pipeline period without gas pockets is 6.6 s. Hence, extremely fast operations are not required. It is only recommended not to change the operation in the branches during the evolution of the transient event.

The extended detection method has been successfully applied in a field test. The field test showed the presence of large gas pockets in the pressurised sewerage main, which was qualitatively confirmed by the steady state measurements and a pigging operation. The field test furthermore showed that the gas pocket location estimate is not negatively affected by the status of valve V2, which confirms that the detection method is applicable in dendritic sewerage mains.

It is emphasised that the transient event should include a valve closure, because of the simple reflection behaviour of a closed valve, which is essential for accurate estimates of the gas pocket location and aggregated volume. More complex boundary conditions deteriorate the accuracy of the detection method.

### 6.8.1 Recommendations

The Fourier transform should be applied to that part of the de-trended transient measurement with minimum noise for optimum results.

Once the first gas pocket has been detected, a number of additional simulations can be performed with the estimated gas pocket volume on the first location. The simulated pressure time series can be directly compared with the measured pressure, which may provide more detailed information on the possibility that the gas is distributed over several smaller gas pockets. The predicted gas pocket volume and location may feed an ITA solver as an initial 'educated guess', if more accurate predictions would be required.

Finally, it is recommended to perform a sensitivity analysis with the uncertain parameters, such as the polytropic coefficient, the final gas pocket pressure and the measured frequencies, in order to assess the uncertainty of the predictions.





## 7 Practical applications

This chapter presents two practical applications of the developed theory:

- Priming of a gravity-driven pipeline in Kootwijkerbroek.
- Pipeline redesign with an inverted siphon to cross a new railroad.

### 7.1 Priming of a gravity-driven transportation pipeline

The gravity-driven transportation pipeline transports wastewater and storm water from an inlet pit in Kootwijkerbroek to the sewerage system of Barneveld at the Nijkerkerweg. The key design data of the gravity line are summarised in Table 7.1. The as-built pipeline profile and the hydraulic grade line (HGL) at 240 m<sup>3</sup>/h are shown in Figure 7.2. A pump in Kootwijkerbroek lifts the water into an inflow structure at the beginning of the gravity pipeline. The width of the inflow structure (1.25 m) decreases gradually to the internal diameter of the pipeline. The downstream boundary condition is a free outflow into the local sewerage system under Dry-Weather-Flow (DWF) conditions. Hence, the gravity line drains completely during DWF conditions. During storm water events, the downstream head may rise up to the local street level at 8.4 m NAP and requires pressurised flow in the entire gravity line to meet the discharge and upstream water level criteria.

Table 7.1: Key design data of Kootwijkerbroek transport pipeline

Parameter	Value	Unit	Parameter	Value	Unit
Pipe material	PVC		Length	7.3	[km]
Internal diameter	376.6	[mm]	Upstream pipe elevation	15.2	[m NAP]
Wall roughness	< 0.4	[mm]	Upstream street level	16.75	[m NAP]
Design capacity	240	[m <sup>3</sup> /h]	Downstream pipe elevation	6.9	[m NAP]
Flow number	0.3	[-]	Downstream street level	8.4	[m NAP]
Friction factor	0.0204	[-]			
Hydraulic gradient with pressurised flow at design capacity	0.10	[%]			

Reported problem: the pump discharge suddenly drops from about 270 m<sup>3</sup>/h to 200 m<sup>3</sup>/h after 3 hours of continuous pumping, which typically occurs after a rainfall event.

The following data was recorded from the SCADA system (Figure 7.1) after the pumping station had been switched off for one night, simulating the situation after a rainfall event.

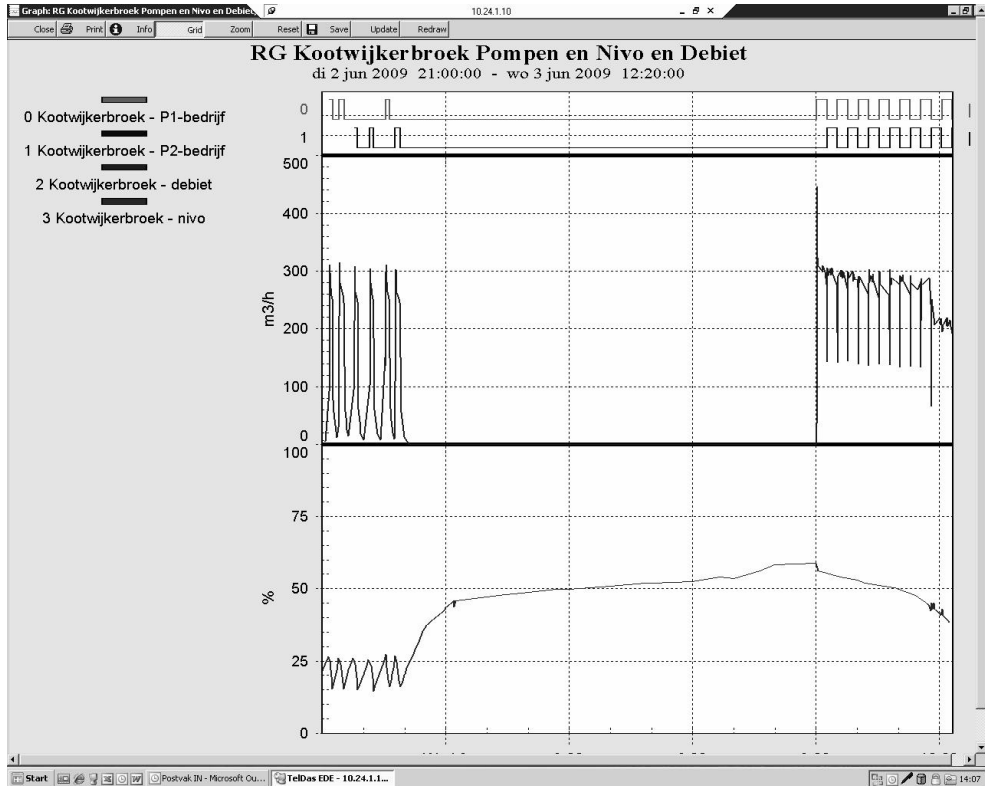


Figure 7.1: SCADA system recording showing pump status, discharge and dimensionless pit level in pumping station Kootwijkerbroek. The vertical grid lines indicate 3 hour intervals.

The pumping station discharge suddenly drops from 270 m<sup>3</sup>/h to slightly above 200 m<sup>3</sup>/h at 12:00 o'clock on June 3<sup>rd</sup> 2009, after nearly 3 hours of continuous operation.

It is essential for proper operation of the pipeline during rainfall events that the gravity pipeline is well vented, so that air pockets cannot get entrapped. However, this gravity line was not equipped with stand pipes or air relief valves at appropriate locations. It was assumed that air would be transported in downstream direction due to the mild pipe slopes in the gravity line.

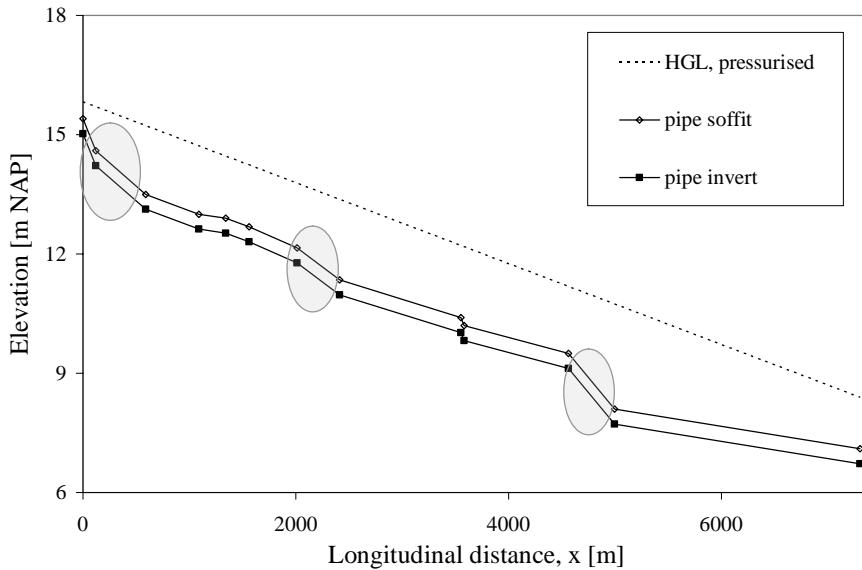


Figure 7.2: Profile of gravity line Kootwijkerbroek

The pipeline contains three sections, indicated by the grey ellipses in Figure 7.2, where the pipe gradient is steeper than the hydraulic gradient at  $240 \text{ m}^3/\text{h}$  and  $270 \text{ m}^3/\text{h}$ . Free-surface flow will only occur in the indicated sections. In the intermediate sections, pressurized flow will occur during priming of the pipeline. The smooth inflow structure will allow the air to escape in upstream direction from the first steeper pipe section, but air will remain entrapped in the two other steep pipe sections after 2km and 4.5km. The air pocket length will hardly decrease in the first three hours, because the local Froude number at normal depth in the steeper sections (with slopes of 0.2% and 0.32%) is still less than unity, which implies that air entraining hydraulic jumps are absent at these pipe sections. Furthermore, the water flow number during priming of the gravity line is  $F_w = 0.34$ , which is insufficient to move an air pocket in downstream direction. The water flow number should exceed 0.6 ( $F_w > 0.6$ ) in near-horizontal pipes to move elongated air pockets in downstream direction, as explained in section 4.4 and Figure 4.5. Therefore, the air pocket length is assumed to be approximately equal to the length of these sections, resulting in the maximum gas pocket head loss. The maximum gas pocket head loss is equal to the elevation difference minus the friction head loss.

Table 7.2: Steep slope data at the design discharge

Start of slope [m]	Length [m]	Slope [%]	Elevation Difference [m]	Gas pocket head loss [m]	Normal depth $y_n$ [m]	Froude number at $y_n$ [-]
2010	400	0.2	0.8	0.4	0.24	0.65
4560	435	0.32	1.4	0.96	0.20	0.88

The filling time of the drained gravity line is 3 hours at 270 m<sup>3</sup>/h. When the filling front has reached the 5km point, the second air pocket gets entrapped. And the system pressure gradually rises as the filling front progresses further into the final section. Due to the increasing pressure, the free surface flow condition in the first 0.5 km will transform into a pressurised flow condition. The air in the first 0.5 km will be relieved at the upstream end of the pipeline, because the flow number is well below the critical flow number of  $F_w = 0.58$ . Once the air has been relieved from the first location, the inflow structure will be filled quickly in a couple of minutes up to the street level at 16.75 m NAP.

It is concluded from the preceding analysis and Table 7.2 that the upstream head increases from 15.3 m NAP to 16.7 m NAP. Such a head increase forces the pump to a duty point with approximately 220 m<sup>3</sup>/h, which is reasonably close to the measured discharge. The original assessment that air would be transported in downstream direction due to the mild pipe slopes in the gravity line is shown to be incorrect. The theory and experiments in this thesis have shown that the net air transport is negligible during priming of this gravity line. Furthermore, the flow number is insufficient to move the elongated air pockets in downstream direction. Proper venting devices are recommended to prevent overflow of the intake structure.

## 7.2 Pipeline redesign – railroad inverted siphon

Water board ‘Rivierenland’ had to redesign a wastewater pressure main from Est to Meteren for the construction of a mayor railroad, connecting the Port of Rotterdam with the German hinterland: the Betuweroute. Inverted siphons have to cross railroads at least 12 metres below the surface level. The existing inverted siphon with a two metre elevation difference to cross a ditch had to be replaced by a thirteen metre deep inverted siphon underneath the Betuweroute (Figure 7.3). The key data of the Est-Meteren wastewater pipeline are summarised in Table 7.3.

With the old, 2.3 m deep inverted siphon, the operators experienced no problems with this wastewater pipeline. However after the installation of the new inverted siphon, the capacity gradually decreased from 40 m<sup>3</sup>/h to approximately 20 m<sup>3</sup>/h in a period of two months.

Table 7.3: Key data of Est-Meteren wastewater pipeline

Parameter	Value	Unit	Parameter	Value	Unit
Pipe material	PVC		Guaranteed capacity	36	[m <sup>3</sup> /h]
Internal diameter	150.6	[mm]	Design capacity	42	[m <sup>3</sup> /h]
Length	2.7	[km]	Static head	2.0	[m]
Wall roughness	< 0.1	[mm]	Friction head at design point	12.2	[m]

Old inverted siphon (PVC)			New inverted siphon (HPE)		
Length	12	[m]	Length	70	[m]
pipe angle	11	[°]	pipe angle	11	[°]
Vertical distance	2.3	[m]	Vertical distance	13.1	[m]
Diameter	150.6	[mm]	Diameter	131	[mm]
Design velocity	0.65	[m/s]	Design velocity	0.87	[m/s]
Flow number	0.54	[-]	Flow number	0.76	[-]

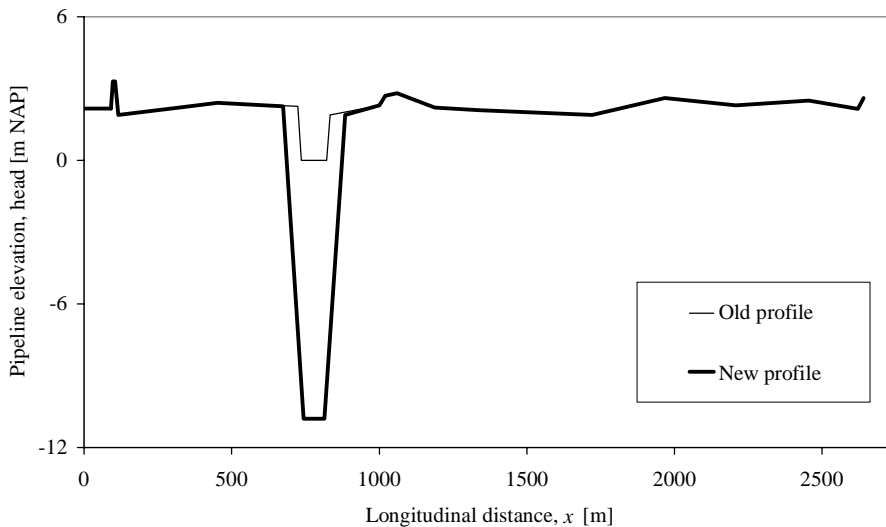


Figure 7.3: Est-Meteren pipeline profile

The pumping station includes two identical fixed speed, wet well pumps and a winding gutter (“slingergoot” in Dutch) for the transport of sediment and the detrainment of air bubbles from the impinging jet from the sewerage pipe. Hence, air entrainment, one of the major causes of capacity reducing gas pockets, does probably not occur in this pumping station.

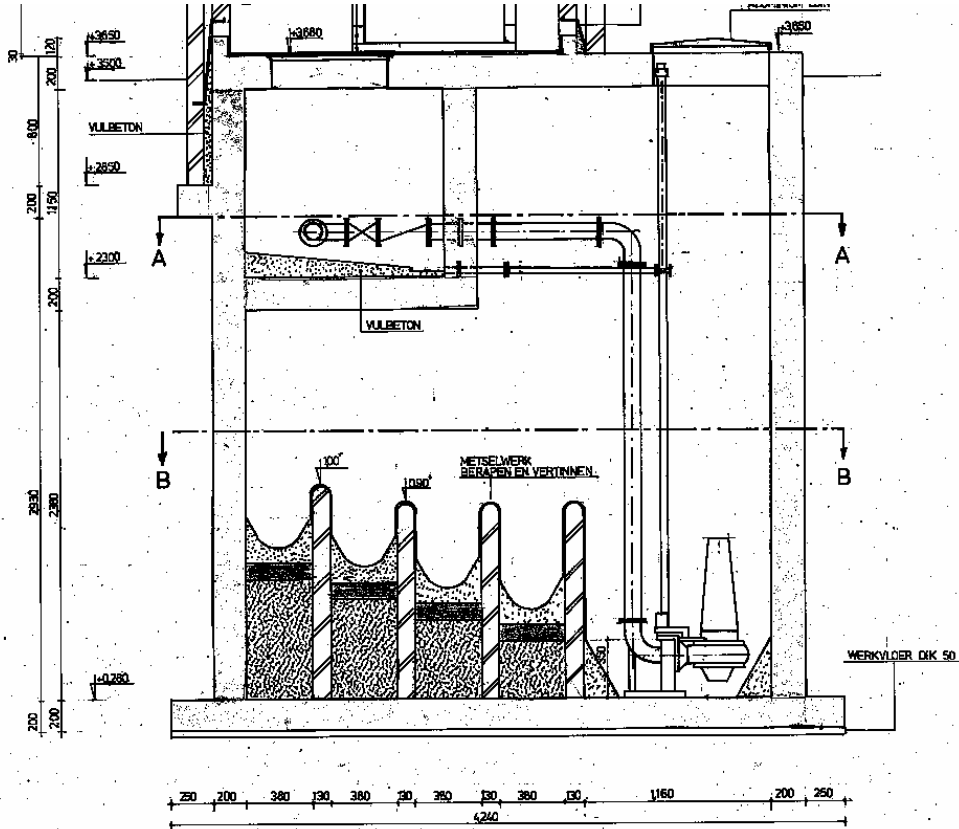


Figure 7.4: Geometry of pump pit in Est

Other causes of air admission in the pumping station include (Kranendonk, 2007):

- 1 Air entraining vortices due to low submergence and poor approach flow towards the pumps.
- 2 the inadvertent air inflow through a one-way air relief valve after a pump stop. Such an air valve is not present in this pumping station.
- 3 The inertia of the pump and the water in the pipeline may lower the water level in the pump pit to the suction bell mouth after a pump stop, so that air enters the vertical pipework. When the pump pit refills, the pumps get submerged and the air gets

entrapped. This phenomenon is a very likely cause of air inflow in this particular case for a number of reasons:

- a The pumps are fixed speed pumps and the normal stop procedure includes a 45 s soft-stop when the shut-off level has been reached.
  - b An anti-surge provision is absent and not necessary for the structural integrity of the pipeline.
  - c The static head is small, so that a relatively large water volume is delivered during the pump run down.
- 4 Intentional air admission via air valves.

It was motivated in chapter 2 that biochemical gas production does not significantly contribute to gas pockets in wastewater mains. The second cause of air admission can be prevented by an appropriate choice of the shut-off level, which is a result of a surge analysis. The shut-off level was 0.61 m NAP. A transient simulation without air in the pipeline shows that the pump pit level drops 8 cm after a pump trip and even 16 cm (!) after the 45 s soft-stop, so that air most likely enters the system (Figure 7.5).

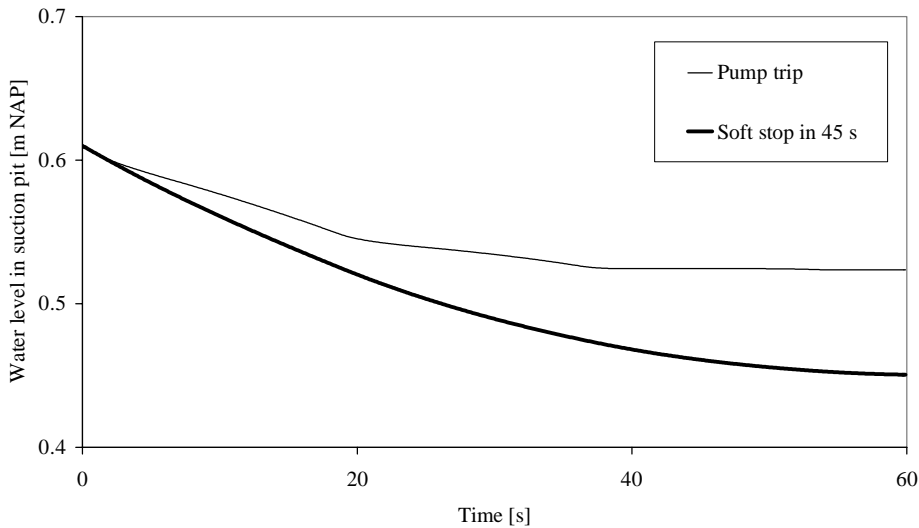


Figure 7.5: Water level drop in time after pump trip or a soft stop in 45 s.

Assuming that the vertical pipework drains completely after a pump stop, an air volume of 30 atmospheric litres enters the system. The time-averaged air discharge is estimated from the average running time per pump cycle. The average pump cycle time is approximately 3 minutes on days with Dry-Weather-Flow (DWF). Hence, the average air flow is 10



litre/min (atmospheric). The system pressure at the inverted siphon is approximately 2 bar.a, which implies that the volumetric air discharge is approximately 5 l/min, which corresponds to a dimensionless gas flow number of 0.004 in the old inverted siphon and 0.006 in the new inverted siphon (due to the smaller diameter in the new HPE inverted siphon).

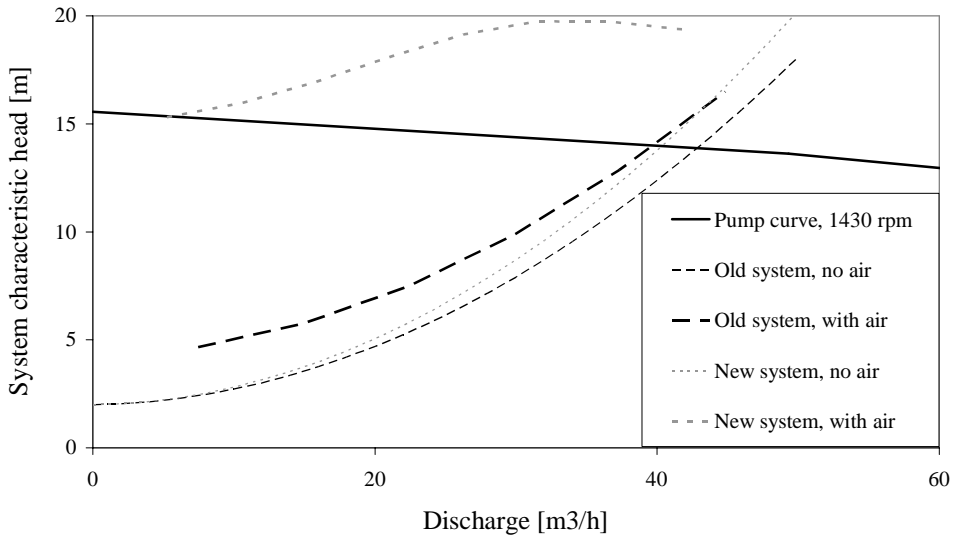


Figure 7.6: System characteristic curves and pump curve, showing the pump duty points in different circumstances

Application of equations (5.15) and (5.9) to the old situation results in a gas pocket head loss of 1.7 m at the design discharge, which is 74% of the maximum gas pocket head loss. This gas pocket head loss results in a discharge reduction from 43 m<sup>3</sup>/h to 40 m<sup>3</sup>/h, which was not perceived as a problematic capacity reduction. The developed model computes the system characteristic including accumulated air pockets in the existing and new system (Figure 7.6). Application of the model to the new inverted siphon results in a highly distorted system characteristic as illustrated in Figure 7.6. Such a gas pocket head loss would reduce the pump discharge to approximately 7 m<sup>3</sup>/h, if air would be admitted until the equilibrium state has been reached. The air pocket almost completely fills the downward sloping section. The stabilization process is a very slow process; it may take quite some time until the equilibrium discharge of 7 m<sup>3</sup>/h is reached. A sensitivity analysis on the entrained air volume per pump stop shows that the equilibrium discharge is not very sensitive for the air discharge: a 4 times smaller air discharge still results in a similar equilibrium air discharge. This analysis confirms the observed capacity reduction.

The operators have increased the shut-off level with 0.1 m, to increase the submergence and minimize the risk of air inflow during the pump run down. This simple has proven to be very effective, because the system capacity has increased to more than 34 m<sup>3</sup>/h and manual venting has shown that large air volumes are not present anymore at the upstream end of the deep inverted siphon.

One issue has not been discussed yet. This is the pump running time per cycle. Pothof *et al.* (2010) have shown that a typical plug velocity is only 40% of the average cross-sectional velocity at typical air-water discharge ratios. With a pump running time of 3 minutes at 40 m<sup>3</sup>/h (or 4 minutes at 30 m<sup>3</sup>/h), the bubbles travel a typical distance of 70 m, which is less than the length of the downward sloping reach. If this is the case, air will further accumulate in the downward sloping reach and the predicted gas pocket head loss must be considered the minimum gas pocket head loss. The equilibrium gas pocket head loss prediction can be improved by the following iteration:

- 1 the equilibrium discharge reduces to a certain value,
- 2 the pump running time increases to a longer period,
- 3 the time average air inflow following pump trip decreases; this is a positive effect, but this effect vanishes completely due to the exponential reduction of the air transport capacity of the flowing water.
- 4 A new system characteristic is determined from the expected air inflow at the reduced water discharge, so that a new equilibrium discharge is derived from the intersection of pump curve and system curve.

This iteration proceeds until the air discharge and water discharge are converged.

### 7.3 Conclusions

Two examples have shown that the developed theory is directly applicable to analyze and solve capacity problems due to air accumulations in water pipelines. The proposed model has been applied to a pressurized wastewater main and a gravity-driven pipeline. The numerical model computes the required water volume to transport air pockets of a certain length to the bottom of an inverted siphon. Finally, several practical issues, related to transients and air accumulation time scales, were emphasized in this chapter.



## 8 Conclusions and recommendations

The main research question, addressed in this thesis is the development and validation of a total air transport model by flowing water, including the influence of pipe angle, length of sloping section, pipe diameter, surface tension, absolute pressure and viscosity. Furthermore, the air transport and gas pocket head loss in wastewater have been compared with those in clean water. In order to validate the model new measurements have been performed in laboratory facilities with internal pipe diameters of 0.08 m and 0.15 m and in a large-scale facility at a wastewater treatment plant ( $D = 0.192$  m ;  $L/D = 209$ ). The key elements of the experimental facilities and the concept of the gas pocket head loss are illustrated in the definition sketch (Figure 8.1).

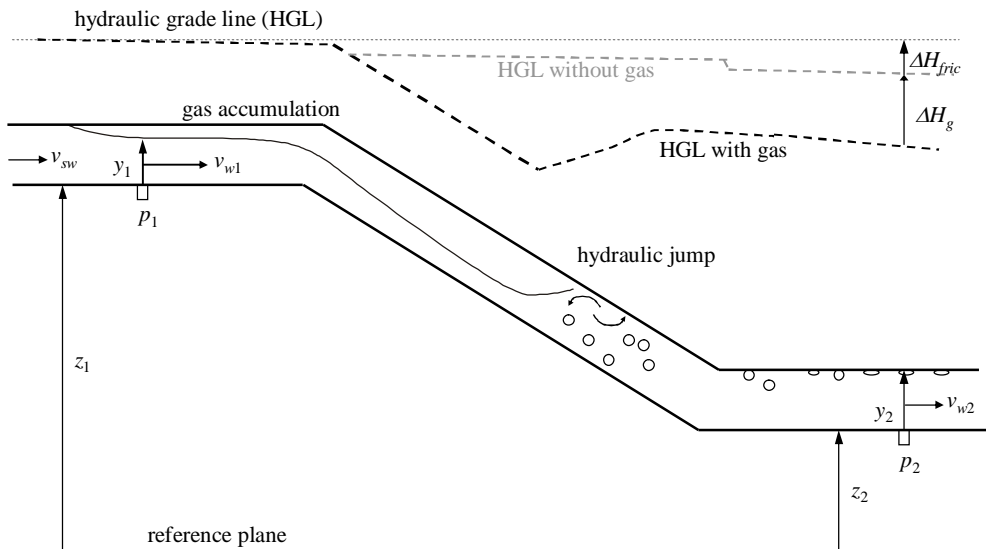


Figure 8.1: Definition sketch for gas pocket head loss measurements in experimental facilities

### 8.1 Conclusions

The following main conclusions are drawn from this thesis:

- 1 A physically based predictive model has been developed for the net air discharge by flowing water in downward sloping pipes. The model parameters include the length of the downward sloping reach and total length of the air pockets, pipe angle, pipe

- diameter, water (or liquid) discharge, viscosity, surface tension and pipe friction factor.
- 2 The model has been calibrated to a unique dataset of co-current air-water flows in downward sloping pipes.
  - 3 The composition of wastewater, i.e. lower surface tension and solids content, does not enhance the air transport in comparison with the air transport in clean water.
  - 4 A new velocity criterion for the occurrence of multiple air pockets in a downward sloping reach has been developed (Figure 8.2). This criterion defines whether the maximum gas pocket head loss may occur in practice.
  - 5 A new momentum balance for elongated air pockets in downward sloping pipes has been developed. This momentum balance defines the clearing flow number (Figure 8.2). It is useful in practice to predict the direction and velocity of an elongated air pocket in a downward sloping pipe. The momentum balance and velocity criterion support the design of storm water storage tunnels and bottom outlets of hydropower stations for the proper venting of pipes and tunnels and for the prevention of severe blow-back events.
  - 6 The required water velocity to start the transport of an elongated gas pocket to the bottom of a downward sloping pipe reach is  $v_{sw} = 0.9 \cdot (gD)^{1/2}$  (or  $F_w = 0.9$ ) over a wide range of pipe angles ( $5^\circ - 20^\circ$ ). This statement has been substantiated with experimental data at  $D > 0.19$  m and the derived momentum balance.
  - 7 A gas pocket detection method for the prediction of a gas pocket location and total gas volume has been extended and tested in field experiments.

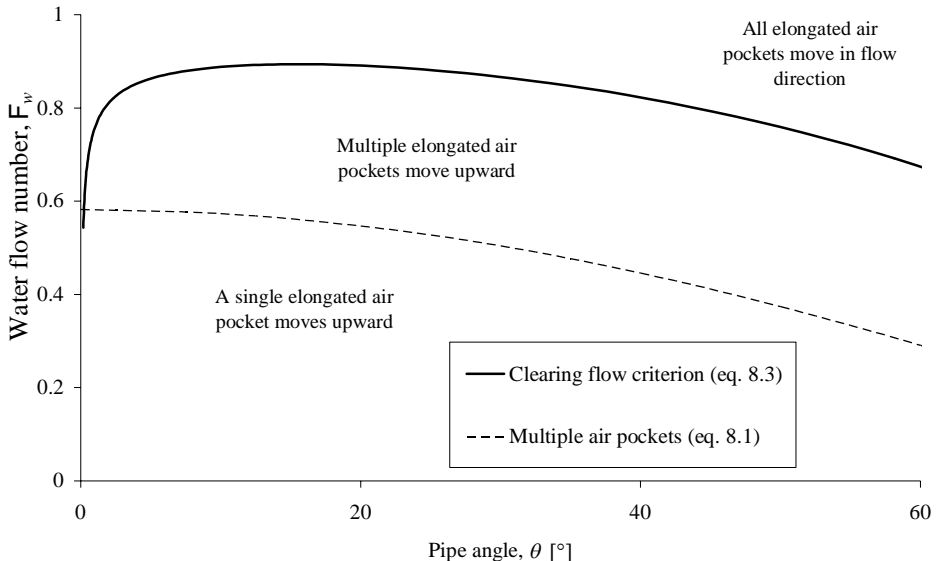


Figure 8.2: Overview of criteria and elongated air pocket motion in downward sloping pipes

The main conclusions will be further detailed in the following paragraphs.

The possible flow regimes of co-current air-water flow in downward sloping pipe reaches have been described in more detail than previously available in literature. The observed flow regimes are stratified, blow-back, plug and dispersed flow. The blow-back flow regime with multiple air pockets is illustrated in Figure 8.3. The flow regime transitions depend on the pipe angle, water flow number, friction factor and air flow number and to a lesser extent on the saturation level of the gas components in the water. In the blow-back flow regime, a series of multiple nearly stable air pockets is present in the downward sloping section, if the water flow number satisfies equation (8.1).

$$F_w > 0.5818[\cos \theta]^{1/2} \quad (8.1)$$

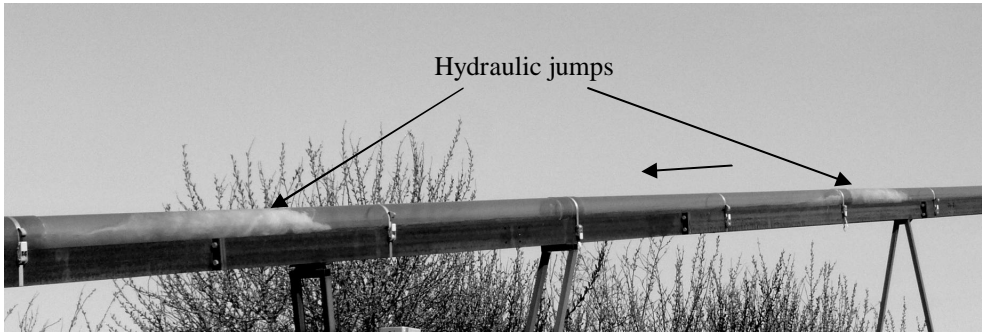


Figure 8.3: Subsequent hydraulic jumps in facility 4 ( $D = 192$  mm,  $L/D = 209$ ,  $\theta = 10^\circ$ ). Water is flowing from right to left.

The gas pocket head loss diminishes at the flow regime transition from blow-back to plug flow. This transition characterises the maximum air transport capacity of the system without accumulation of air. The dimensionless required water velocity (or clearing flow number  $F_c$ ) at this transition is described by

$$F_c = F(\theta) \cdot \left( \frac{\sigma}{0.072} \right)^{1/2} \left( \frac{\min\{D, 0.19\} 10^{-6}}{0.19} \frac{10^{-6}}{\nu} \right)^{3/14} \cdot \ln \left[ \left( \frac{F_g \cdot 10^7}{1.87} \right)^{1/9} \right] \quad (8.2)$$

where  $F(\theta)$  is the water flow number, derived from the momentum balance on a stabilised elongated air pocket in a pipe with  $D > 0.19$  m (or  $Eu > 5000$ )

$$F^2(\theta) = \frac{\sin \theta}{\lambda} \frac{D_h}{D} \left( \frac{A_n}{A_D} \right)^2 + \frac{A_D}{A_b} \frac{\cos \theta}{2\pi} \left[ \frac{2}{3} \sqrt{\frac{2y_n}{R} - \left( \frac{y_n}{R} \right)^2} \left( \frac{y_n}{R} - 3 \right) \left( \frac{y_n}{R} - \frac{1}{2} \right) + \arcsin \left( 1 - \frac{y_n}{R} \right) + \frac{\pi}{2} \right] \quad (8.3)$$

The clearing flow number equation is a function of pipe diameter, pipe angle, viscosity, surface tension and the air flow number and provides a more complete description than the available air pocket clearing velocity correlations. Despite the fact that most experiments were carried out with an air-water mixture, equation (8.2) seems applicable to other fluid mixtures, although validation is recommended. The numerical model is a combination of a momentum balance and experimental correlations. The correlations may be replaced with physically-based relations in the future, if sufficient new knowledge on a number of detailed processes comes available. Recommendations for further research are detailed below.

The underlying momentum balance, eq. (8.3) and Figure 8.2, predicts the flow direction of elongated air pockets in large diameter downward sloping pipes. If the water flow number exceeds  $F(\theta)$ , an elongated air pocket will move in flow direction, otherwise it will move upward along the pipe soffit. Figure 8.2 shows that the water flow number should exceed 0.6 at near horizontal pipe angles in order to drag elongated air pockets in flow direction. Figure 8.2 also supports the design of storm water storage tunnels and bottom outlets of hydropower stations for the proper venting of pipes and tunnels and for the prevention of severe blow-back events.

For air-water flows in downward sloping pipes at pipe angles  $5^\circ < \theta < 20^\circ$ ,  $F(\theta) \approx 0.9$ . The clearing velocity can be approximated as

$$F_c = 0.9 \cdot \left( \frac{\min\{D; 0.19\}}{0.19} \right)^{3/14} \cdot \ln \left[ \left( \frac{F_g \cdot 10^7}{1.87} \right)^{1/9} \right] \quad (8.4)$$

If the water flow number is smaller than the clearing flow number, then air accumulates in the downward sloping section until the gas pocket head loss has reached an equilibrium. The equilibrium gas pocket head loss follows a beta distribution function in the water flow number and the length of the reach

$$1 - R = B(x, \alpha, \beta) = \frac{\int_0^x t^{\alpha-1} (1-t)^{\beta-1} dt}{\int_0^1 t^{\alpha-1} (1-t)^{\beta-1} dt} \quad (8.5)$$

with

$$\begin{aligned} R &= \Delta H_{gas} / (L \sin \theta) \\ x &= F_w / F_c \\ \alpha &= 9.67 \cdot 10^{-2} (L/D - 10.3)^{0.783}, \quad 20 \leq L/D \leq 210 \\ \beta &= 9.39 \cdot 10^{-3} L/D + 0.439 \end{aligned} \quad (8.6)$$

The experimental data show that the air discharge increases exponentially in the water flow number at a given air pocket head loss. The air discharge in the blow-back flow regime is accurately described by

$$F_g = 1.87 \cdot 10^{-7} \exp \left\{ 9 \frac{F_w}{F(\theta)} \left( \frac{0.072}{\sigma} \right)^{1/2} \frac{1}{B^{-1}(1-R, \alpha, \beta)} \right\} \quad (8.7)$$

The increased air discharge is possible at the cost of an air accumulation and the associated gas pocket head loss. The dimensionless gas pocket head loss,  $\Delta H_g / (L \sin \theta)$ , is approximately equal to the aggregated air pocket length ratio  $L_g / L$ .

A novel air pocket detection method has been developed and validated both numerically and in a field test. The prediction of the air pocket volume and location is based on the frequency spectrum of a pressure transient. The transient event should include a valve closure for optimum accuracy of the detection method. The initiating transient event does not have to be a fast operation. A manoeuvring time of one to three pipe periods yield similar results in terms of air pocket volume and location.

## 8.2 Recommendations for practical applications

The required water velocity to start the transport of an elongated gas pocket to the bottom of a downward sloping pipe reach is  $v_{sw} = 0.9 \cdot (gD)^{1/2}$  (or  $F_w = 0.9$ ) over a wide range of pipe angles ( $5^\circ - 20^\circ$ ). This statement has been substantiated with experimental data at  $D > 0.19$  m and the derived momentum balance.



At  $D < 0.19$  m, an individual elongated air pocket starts to move if the undisturbed hydraulic grade line – i.e. without air pockets – exceeds 0.6% (6 metre per kilometre). This result has been obtained in pipes with relative wall roughness  $k_w/D < 10^{-3}$  and pipe diameters  $0.08 \text{ m} \leq D \leq 0.192 \text{ m}$ .

The CAPWAT research project (2004 – 2010) has led to a much better understanding of the accumulation, breakdown and transport of gas pockets in downward sloping sections of pipelines. The research project has led to many practical recommendations for the hydraulic design, commissioning, safe operation and maintenance of pressurised wastewater mains, which are available in an electronic handbook (Deltares, 2010).

### 8.3 Recommendations for future research

The developed numerical model for the air discharge contains experimental correlations for the influence of the air accumulation on the air discharge in the blow-back flow regime. Physically, the air discharge in this flow regime is governed by the entrainment and detrainment of air and the motion of elongated air pockets, resulting in a steady state situation with a series of elongated air pockets in hydraulic jumps. Hydraulic jumps in circular tubes are 3D jumps due to the side wall curvature and therefore different from hydraulic jumps in rectangular channels. Furthermore, the air entrainment and detrainment are affected by the pipe angle. Most of the involved processes are still poorly understood. The following investigations are recommended:

- Properties of hydraulic jumps in inclined circular conduits with fully developed inflow conditions. The properties include water and bubble velocity profiles, air bubble concentration and size distribution, water turbulence profiles in the cross-section and in longitudinal direction.
- Verification of elongated air pocket velocities and net air discharge in the blow-back flow regime.
- A physically based 2D advection diffusion model in combination with a drift flux model for the elongated air pockets should aim at correct predictions of the stationary number of hydraulic jumps in the blow-back flow regime in addition to the gas pocket head loss and air discharge.
- Furthermore, the interface area and the turbulence in the hydraulic jumps are helpful parameters for the modelling of the air mass transfer into the water phase, which may be a dominant process in this flow regime.

A video analysis of plug motion and plug size in the plug flow regime results in the determination of many plug flow properties, such as plug frequency, plug size, plug velocity and plug drag coefficient (Pothof et al., 2010). These video analyses should be carried out for a range of pipe angles to obtain a more complete description of the plug flow regime.

In order to assess the validity of the numerical model for other fluid mixtures, the influence of surface tension, viscosity and pipe diameter on the gas pocket head loss and clearing velocity should be verified.

The air transport model, presented in this thesis may serve as validation data to extend the range of applicability of existing two-phase flow codes. A strong similarity exists between the behaviour of elongated gas pockets in downward sloping pipes and the elongated bubble drift velocity in inclined pipes. Since bubble drift velocities have not yet been determined in pipelines of sufficient length ( $L/D > 20$ ) and Eötvös number  $Eo > 5000$  (or  $D > 0.19$  m)—despite its relevance for slug flow modelling— it is recommended to determine the bubble drift velocities over a range of upward pipe angles.

Surface entrainment was not observed in the experiments in the transparent facilities with pipe diameters up to 0.22 m and Reynolds numbers up to 250,000. The experimental data in facility 7 (0.5 m, steel) suggest that surface entrainment neither occurred in facility 7. It remains to be verified whether surface entrainment may enhance the air transport at much larger Reynolds numbers ( $> 10^6$ ).



---

## References

- Al-Safran, E., 2008. Slug frequency in gas/liquid horizontal flow, 6th North American Conference on Multiphase Technology BHR Group, Banff, Canada.
- ANSI/ISA-75.02, 1996. Control valve capacity test procedures.
- Bendiksen, K.H., 1984. Experimental investigation of the motion of long bubbles in inclined tubes. *International Journal of Multiphase Flow* 10(4), 467-483.
- Benjamin, T.B., 1968. Gravity currents and related phenomena. *Journal of Fluid Mechanics* 31, 209-248.
- Bliss, P.H., 1942. The removal of air from pipelines by flowing water, Iowa institute of hydraulic research, Iowa.
- Bonizzi, M., Andreussi, P. and Banerjee, S., 2009. Flow regime independent, high resolution multi-field modelling of near-horizontal gas-liquid flows in pipelines. *International Journal of Multiphase Flow* 35(1), 34-46.
- Brocchini, M. and Peregrine, D.H., 2001. The dynamics of strong turbulence at free surfaces. Part 1. Description. *Journal of Fluid Mechanics* 449, 225-254.
- Brunone, B., 1999. Transient test-based technique for leak detection in outfall pipes. *Journal of Water Resources Planning and Management* 125(5), 302-306.
- Butler, D. and Davies, J., 2009. *Urban Drainage*. SPON, New York, 543 pp.
- Capart, H., Sillen, X. and Zech, Y., 1997. Numerical and experimental water transients in sewer pipes. *J. Hydr. Res.* 35(5), 659-672.
- Chanson, H., 1995. Air-water gas transfer at hydraulic jump with partially developed inflow. *Water Research* 29(10), 2247-2254.
- Chanson, H., 1996. Air bubble entrainment in free-surface turbulent shear flows Academic Press, San Diego, 348 pp.
- Chanson, H., 1997. Air-water flows in partially-filled conduits. *Journal of Hydraulic Research* 35(5), 591-601.
- Chanson, H., 2004. *Environmental hydraulics of open channel flows*. Elsevier Butterworth-Heinemann, Amsterdam, 430 pp.
- Chanson, H., 2009. Turbulent air-water flows in hydraulic structures: Dynamic similarity and scale effects. *Environmental Fluid Mechanics* 9(2), 125-142.
- Chanson, H. and Brattberg, T., 2000. Experimental study of the air-water shear flow in a hydraulic jump. *International Journal of Multiphase Flow* 26(4), 583-607.
- Covas, D., Ramos, H., Brunone, B., Young, A., 2004. Leak detection in water trunk mains using transient pressure signals: field tests in Scottish Water, The practical application of surge analysis for design and operation. BHR Group Ltd., Chester.
- Davies, J.T., 1972. *Turbulence phenomena*. Academic Press, New York.
- De Leebeeck, A., Nydal, O.J., Johnson, G.W., Monsen, J.I. and Goldszal, A., 2008. Comparison of two-phase pipe flow experiments with a roll wave model and a commercial simulator, 6th North American Conference on Multiphase Technology. BHR Group, Banff.
- Deltares, 1993 - 2008. WANDA, pipeline simulation software, Delft Hydraulics Software. Deltares | Delft Hydraulics.

- 
- Deltares, 2010. Wiki - Hydraulics handbook for pressurised wastewater mains (in Dutch). Deltares, Delft, pp. <http://capwat.deltares.nl>.
- Escaramela, M., 2007. Investigating hydraulic removal of air from water pipelines. Proceedings of the Institution of Civil Engineers: Water Management 160(1), 25-34.
- Falvey, H.T., 1980. Air-water flow in hydraulic structures, Water and Power Resources Service, Denver, Colorado.
- Ferrante, M. and Brunone, B., 2003. Pipe system diagnosis and leak detection by unsteady-state tests. 1. Harmonic analysis. Advances in Water Resources 26(1), 95-105.
- Fox, R.W., McDonald, A.T., 1985. Introduction to fluid mechanics. John Wiley & Sons, New York.
- Gandenberger, W., 1957. Über die wirtschaftliche und betriebssichere Gestaltung von Fernwasserleitungen. R. Oldenbourg Verlag, München.
- Gualtieri, C. and Chanson, H., 2007. Experimental analysis of Froude number effect on air entrainment in the hydraulic jump. Environmental Fluid Mechanics 7(3), 217-238.
- Gudmundsson, J.S.a.C., H.K., 1999. Gas-Liquid Metering Using Pressure-Pulse Technology, Annual Technical Conference and Exhibition. Society of Petroleum Engineers, Houston.
- Hager, W.H., 1993. Energy dissipators and hydraulic jump. Water science and technology library, 8. Kluwer, Dordrecht, 288 pp.
- Hager, W.H., 1999. Cavity outflow from a nearly horizontal pipe. International Journal of Multiphase Flow 25(2), 349-364.
- Hager, W.H. and Bremen, R., 1989. Classical hydraulic jump: sequent depths. Journal of Hydraulic Research 27(5), 565-585.
- Hinze, J.O., 1955. Fundamentals of the hydrodynamic mechanism of splitting in dispersion processes. AIChE Journal 1(3), 289-295.
- Hurlburt, E.T. and Hanratty, T.J., 2002. Prediction of the transition from stratified to slug and plug flow for long pipes. International Journal of Multiphase Flow 28(5), 707-729.
- Johnson, Kotz and Balakrishnan, 1994. Continuous Univariate Distributions, Vol. 1 and 2. John Wiley and Sons, New York.
- Kalinske, A.A. and Bliss, P.H., 1943. Removal of air from pipe lines by flowing water. Proceedings of the American Society of Civil Engineers (ASCE) 13(10), 3.
- Kalinske, A.A., Robertson, J.M., 1943. Closed Conduit Flow. Transactions of the American Society of Civil Engineers (ASCE) 108, 1435-1447.
- Kamma, P.S., Witter, V. and Zijl, v.F.P., 1995. Ontwerppraktijk van persleidingen (Design practice of pipelines). H2o(8), (in Dutch).
- Kent, J.C., 1952. The entrainment of air by water flowing in circular conduits with downgrade slope, University of Berkeley, Berkeley, California.
- Korving, H., Clemens, F.H.L.R. and van Noortwijk, J.M., 2006. Statistical modeling of the serviceability of sewage pumps. Journal of Hydraulic Engineering 132(10), 1076-1085.
- Kranendonk, M., Pothof, I.W.M., 2007. Preventie van luchtinname door rioolgemalen (Prevention of air intake in wastewater pumping stations). H4230.41, Deltares | Delft Hydraulics, Delft.
- Kucukali, S. and Chanson, H., 2008. Turbulence measurements in the bubbly flow region of hydraulic jumps. Experimental Thermal and Fluid Science 33(1), 41-53.

- Lauchlan, C.S., Escameia, M., May, R.W.P., Burrows, R., Gahan, C. , 2005. Air in Pipelines, a literature review. SR 649 rev 2.0, HR Wallingford.
- Lemmens, R.P.M., 1996. Themamiddag: problemen met gasbellen in persleidingen, hoezo? (Workshop: problems with gas pockets in pressurised pipelines, why?), Delft Hydraulics, Delft.
- Liggett, J.A. and Chen, L.-C., 1994. Inverse transient analysis in pipe networks. *Journal of Hydraulic Engineering* 120(8), 934-955.
- Liou, J.C.P., 1993. Pipeline variable uncertainties and their effects on leak detectability, American Petroleum Institute.
- Lubbers, C.L., 2007. On gas pockets in wastewater pressure mains and their effect on hydraulic performance, Delft University of Technology, Delft, 290 pp.
- Lubbers, C.L. and Clemens, F.H.L.R., 2005. On detecting gas pockets in pressurised wastewater mains, 10th Int. Conf. on Urban Drainage, Copenhagen.
- Lubbers, C.L. and Clemens, F.H.L.R., 2007. Scale effects on gas transport by hydraulic jumps in inclined pipes; comparison based on head loss and breakdown rate, 6th Int. Conference on Multiphase Flow (ICMF), Leipzig.
- Montes, J.S., 1997. Transition to a Free-surface flow at end of a horizontal conduit. *Journal of Hydraulic Research* 35(2), 225-240.
- Mosvell, G., 1976. Luft I utslippsledning (Air in outfalls), Norwegian Water Institute (NIVA), Oslo.
- Murzyn, F. and Chanson, H., 2008. Experimental investigation of bubbly flow and turbulence in hydraulic jumps. *Environmental Fluid Mechanics*, 1-17.
- Nezu, I., Nakagawa, H., 1993. Turbulence in open-channel flows. IAHR Monograph series. A.A. Balkema, Rotterdam, 281 pp.
- Nicklin, D.J., Wilkes, D.O. and Davidson, J.F., 1962. Two-phase flow in vertical tubes. *Transactions of the Institute of Chemical Engineers* 40, 61-68.
- Pothof, I. and Clemens, F., 2009. On the modelling of gas diffusion by turbulence in hydraulic jumps, 33rd IAHR Congress: Water Engineering for a Sustainable Environment. Int. Ass. of Hydraulic Engineering & Research (IAHR), Vancouver.
- Pothof, I.W.M. and Clemens, F.H.L.R., 2008a. Detection of gas pockets in dendritic wastewater mains. In: S. Hunt (Editor), 10th Int. Pressure Surges Conference. Surge Analysis – system design, simulation, monitoring and control. BHR Group Ltd, Edinburgh, UK, pp. 271-285.
- Pothof, I.W.M. and Clemens, F.H.L.R., 2008b. On gas transport in downward slopes of sewerage mains, 11th Int. Conf. on Urban Drainage, Edinburgh.
- Pothof, I.W.M. and Clemens, F.H.L.R., 2010a. Experimental study of air-water flow in downward sloping pipes. *Int. J. of Multiphase Flow* (in press).
- Pothof, I.W.M. and Clemens, F.H.L.R., 2010b. On elongated air pockets in downward sloping pipes. *Journal of Hydraulic Research* 48(4), 499 - 503.
- Pothof, I.W.M., Kooij, C., Clemens, F.H.L.R. and Schuit, A.D., 2009. Gasbellen in persleiding: beter voorkomen dan genezen (Gas pockets in pressurised pipes: prevention is better than recovery). *Land + Water*(6/7), 30-31 (in Dutch).
- Pothof, I.W.M., Kuipers, H., Reitsma, G. and Clemens, F.H.L.R., 2010. Interface drag on plugs in downward sloping pipes, 7th Int. Conf. on Multiphase Flow. University of Florida, Tampa (FL).
- Rajaratnam, N., 1967. Hydraulic Jumps, *Advances in Hydrosience*. Academic Press, Inc., San Diego, California, pp. 197 - 280.

- 
- Rein, M., 1998. Turbulent open-channel flows: Drop-generation and self-aeration. *Journal of Hydraulic Engineering* 124(1), 98-101.
- Resch, F.J. and Leutheusser, H.J., 1972. Reynolds Stress Measurements in Hydraulic Jumps. *Journal of Hydraulic Research* 10(4), 409-430.
- Resch, F.J., Leutheusser, H.J. and Alemu, S., 1974. BUBBLY TWO-PHASE FLOW IN HYDRAULIC JUMP. *ASCE J Hydraul Div* 100(HY1), 137-149.
- Resch, F.J., Leutheusser, H.J. and Coantic, M., 1976. Study of Kinetmatic and Dynamic Structure of the Hydraulic Jump. *ETUDE DE LA STRUCTURE CINEMATIQUE ET DYNAMIQUE DU RESSAUT HYDRAULIQUE*. 14(4), 293-319.
- Rouse, H., Siao, T.T. and Nagaratnam, S., 1959. Turbulence characteristics of the hydraulic jump. *Trans. ASME* 124, 926-966.
- Ruder, Z. and Hanratty, T.J., 1990. A definition of gas-liquid plug flow in horizontal pipes. *International Journal of Multiphase Flow* 16(2), 233-242.
- Smit, A., 2007. Air entrainment with plugging jets. Msc Thesis, Delft University of Technology, Delft, 84 pp.
- SPT Group Norway, S.A., 2010. OLGA multiphase flow simulator, pp. <http://www.sptgroup.com/en/Products/olga/>
- Stephens, M., Lambert, M., Simpson, A., Vitkovsky, J. and Nixon, J., 2004. Field tests for leakage, air pocket, and discrete blockage detection using inverse transient analysis in water distribution pipes, *Proceedings of the 2004 World Water and Environmental Resources Congress: Critical Transitions in Water and Environmental Resources Management*, pp. 4779-4788.
- Stephens, M., Vitkovsky, J., Lambert, M., Simpson, A., Karney, B., Nixon, J., 2004. Transient analysis to assess valve status and topology in pipe networks, *The practical application of surge analysis for design and operation*. BHR Group Ltd., Chester.
- Stoianov, I., Maksimovic, C., Graham, N. and Dellow, D. , 2003. Field validation of the application of hydraulic transients for leak detection in transmission pipelines, *International Conference on Computing and Control for the Water Industry*, London.
- Svendsen, I.B.A., Veeramony, J., Bakunin, J. and Kirby, J.T., 2000. The flow in weak turbulent hydraulic jumps. *Journal of Fluid Mechanics* 418, 25-57.
- Thorley, A.R.D., 2004. *Fluid Transients in Pipeline Systems, A Guide to the Control and Suppression of Fluid Transients in Liquids in Closed Conduits*. Professional Engineering Publishing Ltd., London, 279 pp.
- Vasconcelos, J.G. and Wright, S.J., 2009. Investigation of rapid filling of poorly ventilated stormwater storage tunnels. *Journal of Hydraulic Research* 47(5), 547 - 558.
- Veronese, A., 1937. Sul motto delle bolle d'aria nelle condotto d'acqua (Italian). *Estrato dal fascicolo X XIV, XV*.
- Volkart, P.U., 1982. Self-aerated flow in steep, partially filled pipes. *Journal of Hydraulics Division ASCE* 108(HY9), 1029-1046.
- Wickenhäuser, M. and Kriewitz, C.R., 2009. Air-Water Flow in Downward Inclined Large Pipes, 33rd IAHR Congress: Water Engineering for a Sustainable Environment. IAHR, Vancouver.
- Wisner, P., Mohsen, F.N. and Kouwen, N., 1975. Removal of air from water lines by hydraulic means. *ASCE J Hydraul Div* 101(HY2), 243-257.

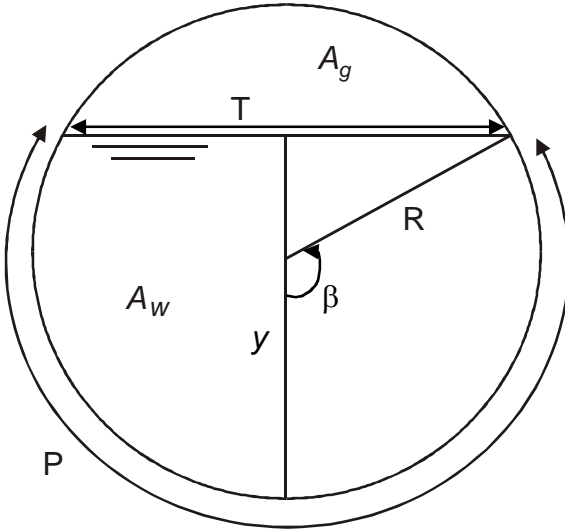
- Wood, I.R., 1983. Uniform region of self-aerated flow. *Journal of Hydraulic Engineering* 109(3), 447-461.
- Wood, I.R., 1991. Air entrainment in free-surface flows. *Hydraulic structures design manual*, 4. A.A. Balkema, Rotterdam.
- Zukoski, E.E., 1966. Influence of viscosity, surface tension, and inclination angle on motion of long bubbles. *Journal of Fluid Mechanics* 25(4), 821-837.





## A Free surface flows in downward sloping circular pipes

### A.1 Geometric relations



$$\sin \beta = \frac{T}{2R} ; \cos \beta = 1 - \frac{y}{R} \quad (\text{A.1})$$

Surface width  $T$ :

$$T(y) = 2R \sqrt{\frac{2y}{R} - \left(\frac{y}{R}\right)^2} \quad (\text{A.2})$$

Wet cross sectional area  $A_w$ :

$$A_w = \beta R^2 - \frac{y}{2}(R - y) = R^2 \left[ \arccos\left(1 - \frac{y}{R}\right) - \left(1 - \frac{y}{R}\right) \sqrt{\frac{2y}{R} - \left(\frac{y}{R}\right)^2} \right] \quad (\text{A.3})$$

Wet perimeter  $P$ :

$$P = 2\beta R = 2R \arccos\left(1 - \frac{y}{R}\right) \quad (\text{A.4})$$

Hydraulic radius  $R_h$ :

$$R_h = \frac{A_w}{P} = \frac{R}{2} - \frac{T}{4\beta} \left( 1 - \frac{y}{R} \right) \quad (\text{A.5})$$

Hydraulic depth  $y_h$ :

$$y_h = \frac{A_w}{T} = \frac{\beta}{T} R^2 - \frac{R}{2} \left( 1 - \frac{y}{R} \right) \quad (\text{A.6})$$

The wet cross section, perimeter and hydraulic radius are scaled to the values for pressurised flow (subscript p) and shown in Figure A.1.

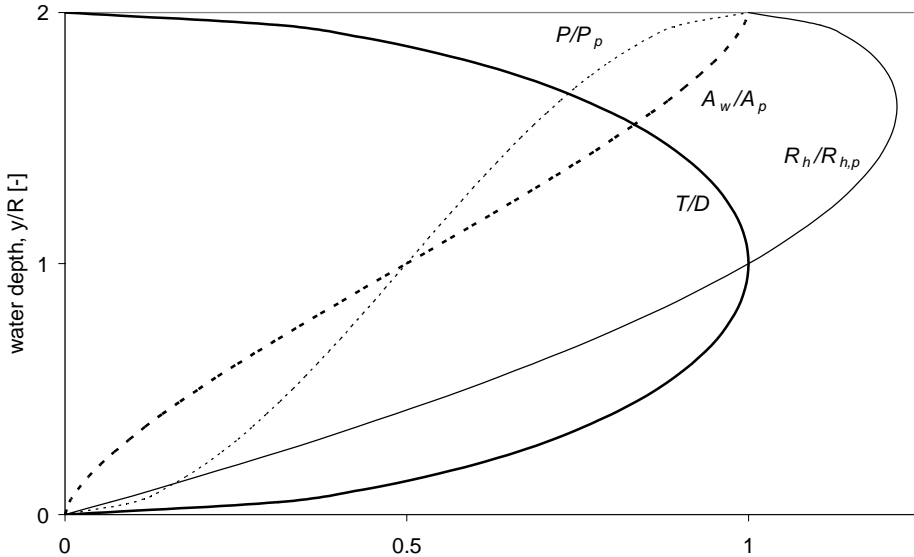


Figure A.1: geometric relations for free surface flows in circular conduits

## A.2 Free surface flow at normal depth

The free surface flow in a downward sloping reach accelerates until the friction force balances the axial component of gravity. If this is the case, then the free surface flow has reached uniform flow, also known as normal flow. The momentum equation at the normal flow conditions is:

$$\rho \cdot g \cdot A_n \sin \theta = \tau_{w,n} P_n \quad (\text{A.7})$$

where the subscript  $n$  refers to the water phase at normal depth. The wall shear stress is based on the White-Colebrook friction factor correlation for open channel flow at normal depth (Fox, 1985):

$$\tau_{w,n} = \lambda \cdot \rho \frac{v_n^2}{8} \quad (\text{A.8})$$

$$\frac{1}{\lambda^{0.5}} = -2 \log \left( \frac{k}{3.7 D_{h,n}} + \frac{2.51}{\text{Re} \cdot \lambda^{0.5}} \right)$$

where the Reynolds number is based on the hydraulic diameter,  $D_{h,n}$ :

$$\text{Re}_n = \frac{v_n D_{h,n}}{v_w} \quad (\text{A.9})$$

Equation (A.7) can be normalized in terms of the flow number or in terms of the local Froude number, yielding:

$$\text{Flow number} \quad \mathbf{F}_w^2 = \frac{v_{s,w}^2}{gD} = \frac{2 \sin \theta}{\lambda} \frac{D_h}{D} \left( \frac{A_n}{A_D} \right)^2 \quad (\text{A.10})$$

$$\text{Froude number} \quad \mathbf{Fr}_n^2 = \frac{v_n^2}{g y_{h,n}} = \frac{v_n^2}{g R_{h,n}} \cdot \frac{R_{h,n}}{g y_{h,n}} = \frac{8 \sin \theta}{\lambda} \frac{T_n}{P_n} \quad (\text{A.11})$$

Finally, the Froude number at the normal flow condition can be expressed as a function of the water flow number, resulting in:

$$\mathbf{Fr}_n^2 = \frac{4}{\pi} \mathbf{F}_w^2 \left( \frac{T_n}{D} \right) \left/ \left( \frac{A_n}{A_D} \right)^3 \right. \quad (\text{A.12})$$

A plot of equation (A.12) shows the surprising result that the Froude number at the normal flow condition is nearly constant over a wide range of practically relevant water flow numbers. Since most investigators have proposed to model the air entrainment rate ( $Q_a/Q_w$ ) as a function of the Froude number only, this observation would imply that the air entrainment rate is constant over a wide range of water flow numbers.

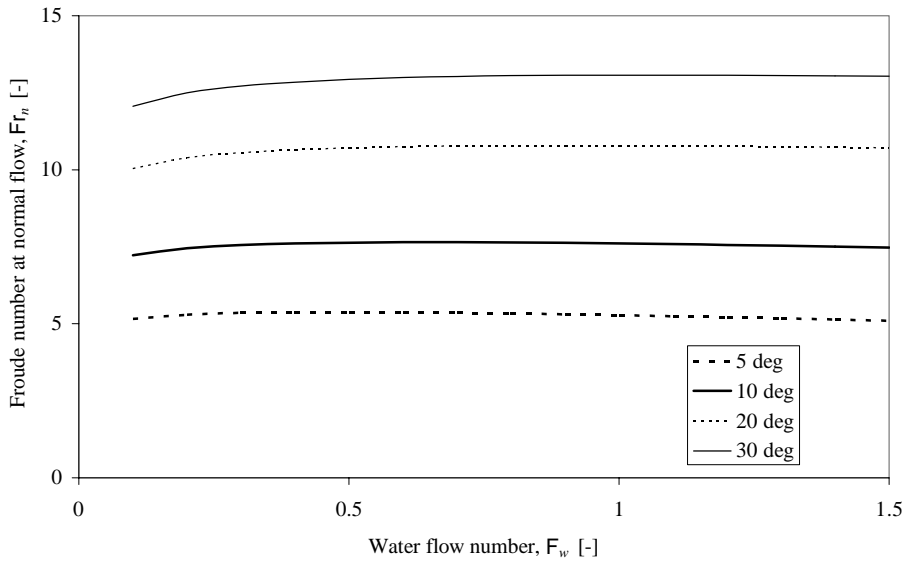


Figure A.2: Froude number at normal flow condition as a function of the water flow number in a circular pipe with diameter  $D = 0.2$  m, wall roughness  $k_n = 0.1$  mm and kinematic viscosity  $\nu = 1.2E-6$ .

## B Experimental results

This appendix lists the experimental results on the gas pocket head loss data. The plotted data points are average values of all stable data points. The total number of stable data points is included in the caption of the graphs in this appendix. The experimental data are archived at Deltares and available via the author of this thesis.

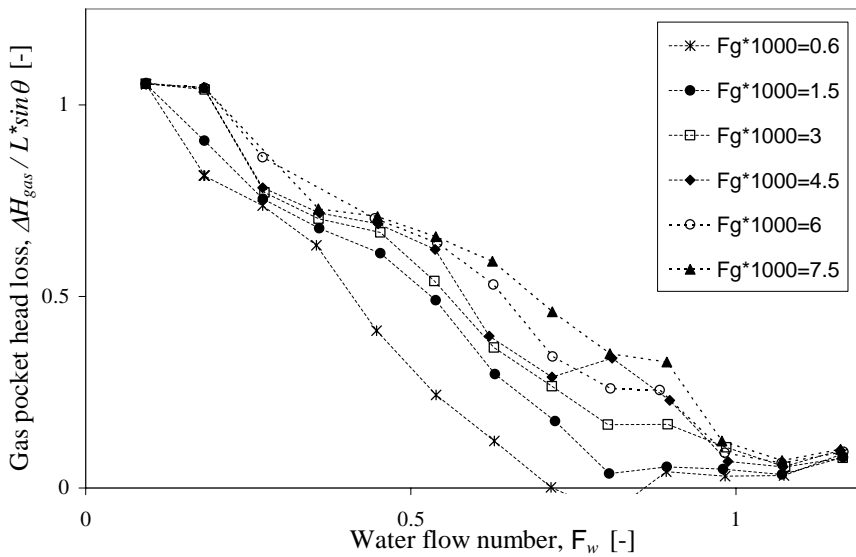


Figure B.1: Gas pocket head loss in facility 1 with  $\theta = 12.5^\circ$ ,  $D = 0.08$  m,  $L/D = 30$ , 77 different air-water discharge combinations and 91 data points

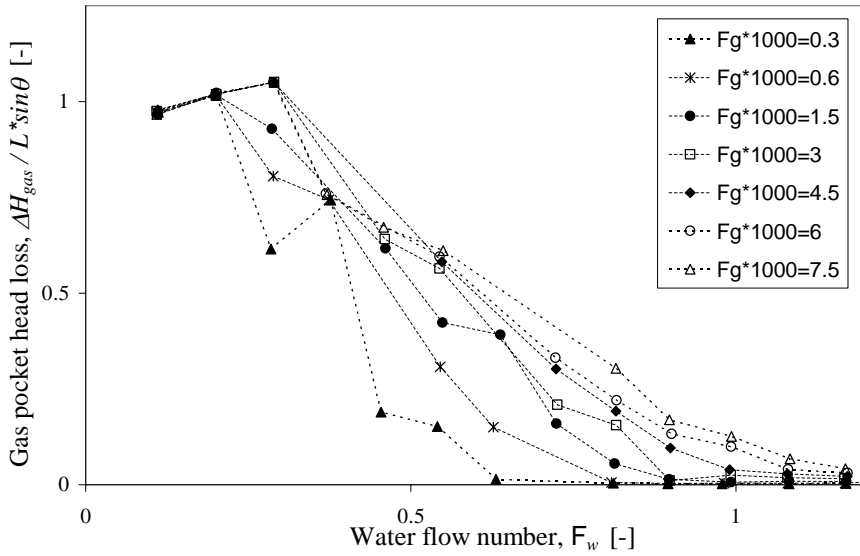


Figure B.2: Gas pocket head loss in facility 2 with  $\theta = 10^\circ$ ,  $D = 0.11$  m,  $L/D = 27$ , 78 different air-water discharge combinations and 313 data points

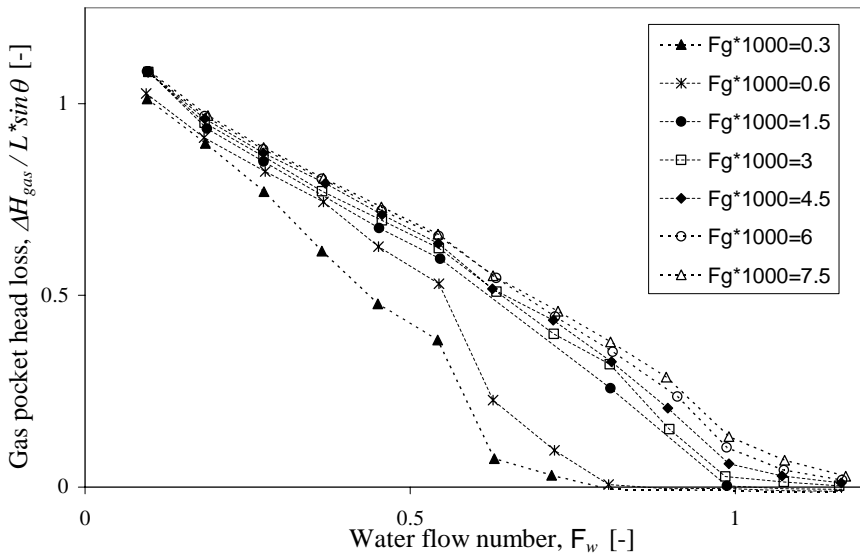


Figure B.3: Gas pocket head loss in facility 3 with  $\theta = 10^\circ$ ,  $D = 0.15$  m,  $L/D = 30$ , 90 different air-water discharge combinations and 106 data points

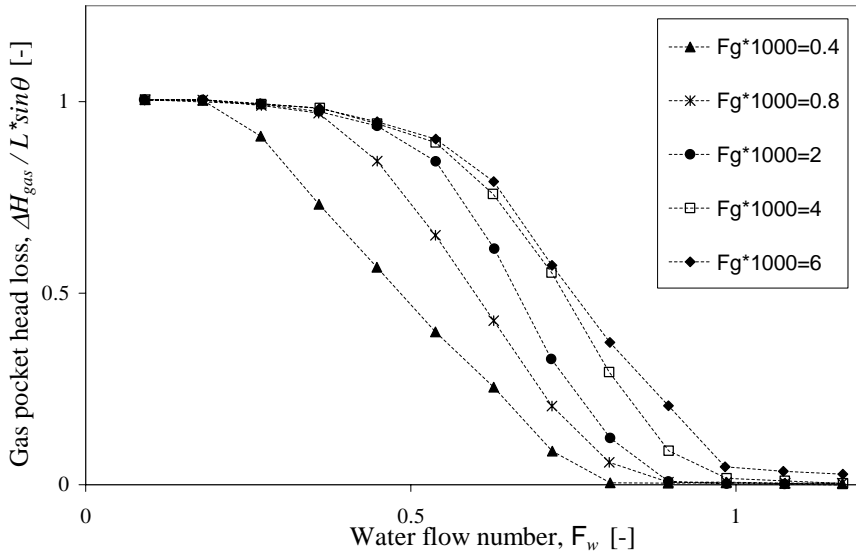


Figure B.4 Gas pocket head loss in facility 4 with  $\theta = 10^\circ$ ,  $D = 0.192$  m,  $L/D = 209$ , 65 different air-water discharge combinations with tap water and 992 data points

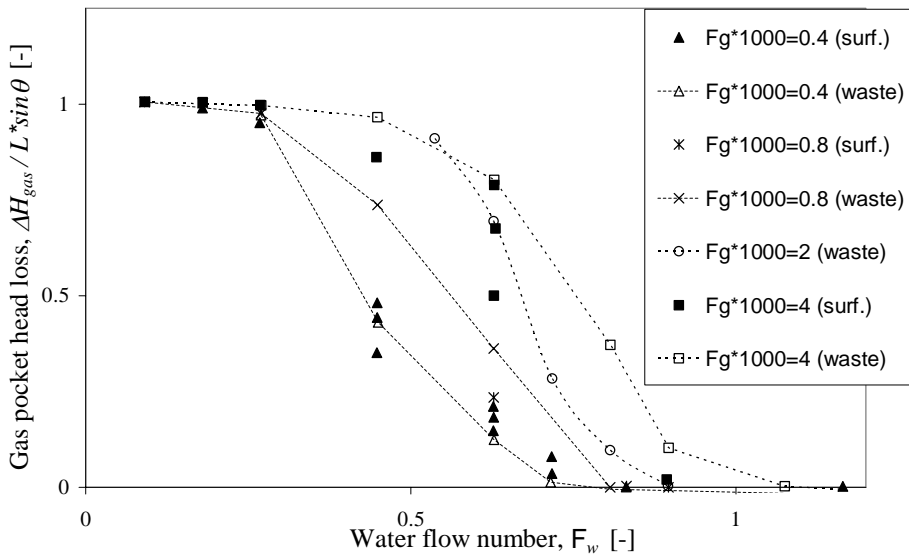


Figure B.5: Gas pocket head loss in facility 4 with  $\theta = 10^\circ$ ,  $D = 0.192$  m,  $L/D = 209$ , 27 different air-water discharge combinations with surfactant-added water and 38 with raw wastewater and 1036 data points



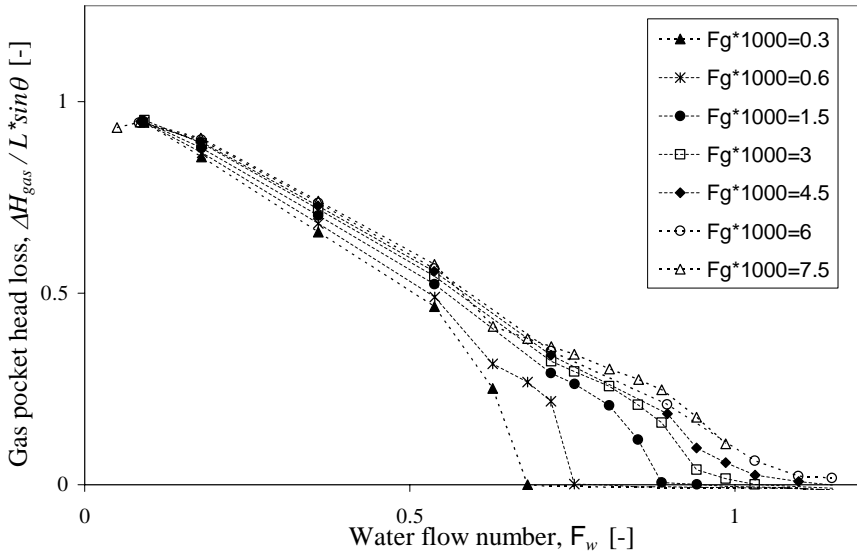


Figure B.6: Gas pocket head loss in facility 5 with  $\theta = 5^\circ$ ,  $D = 0.22$  m,  $L/D = 30$ , 90 different air-water discharge combinations and 295 data points

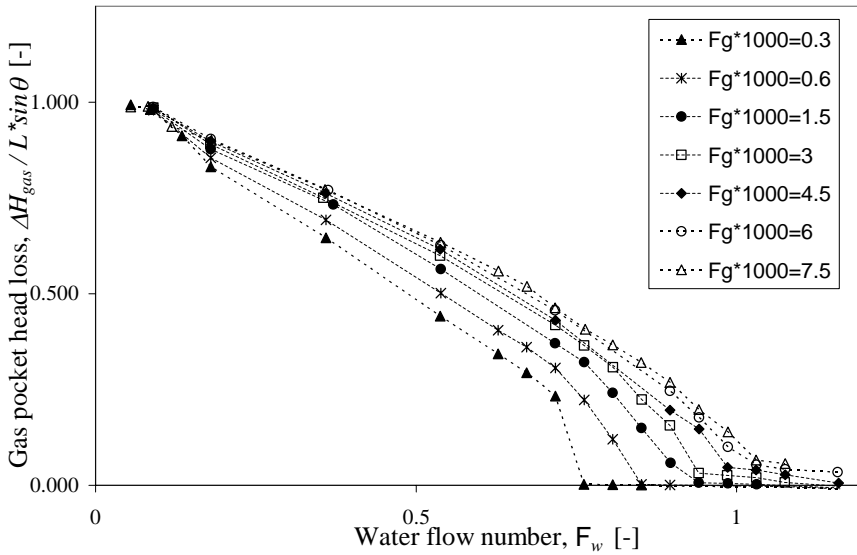


Figure B.7: Gas pocket head loss in facility 5 with  $\theta = 10^\circ$ ,  $D = 0.22$  m,  $L/D = 30$ , 95 different air-water discharge combinations and 324 data points

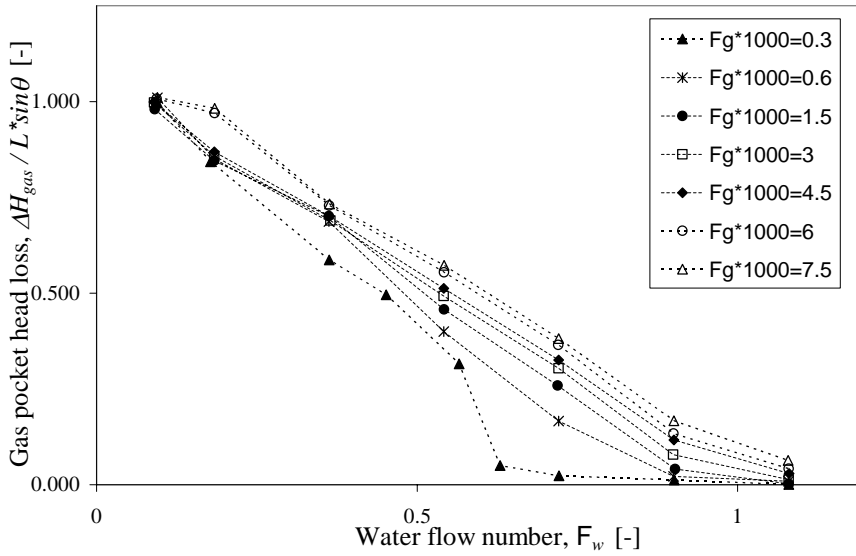


Figure B.8: Gas pocket head loss in facility 5 with  $\theta = 20^\circ$ ,  $D = 0.22$  m,  $L/D = 30$ , 51 different air-water discharge combinations and 198 data points

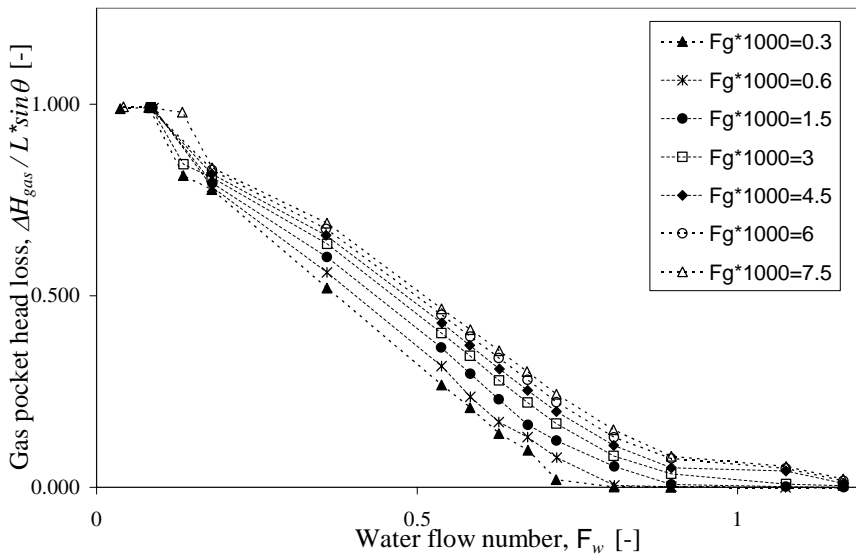


Figure B.9: Gas pocket head loss in facility 5 with  $\theta = 30^\circ$ ,  $D = 0.22$  m,  $L/D = 30$ , 83 different air-water discharge combinations and 291 data points

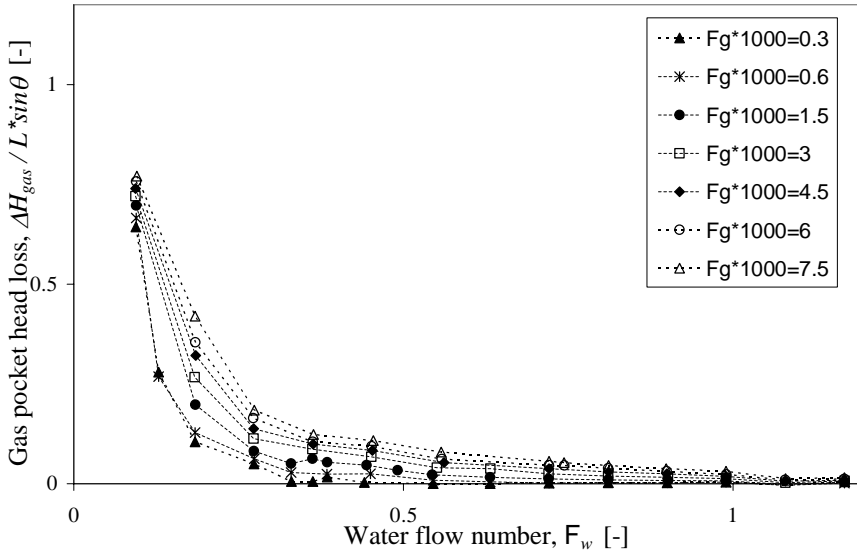


Figure B.10: Gas pocket head loss in facility 5 with  $\theta = 90^\circ$ ,  $D = 0.22$  m,  $LD = 10$ , 98 different air-water discharge combinations and 298 data points

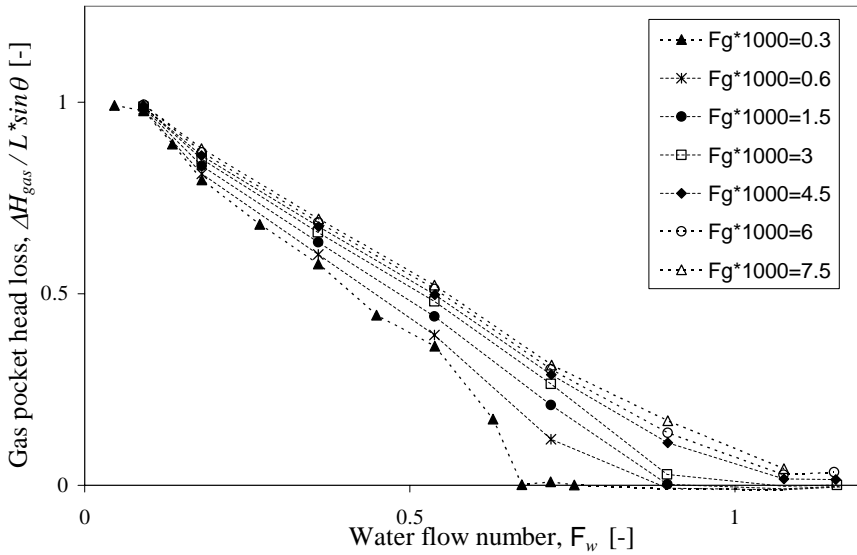


Figure B.11: Gas pocket head loss in facility 6 with  $\theta = 10^\circ$ ,  $D = 0.22$  m,  $LD = 21$ , 61 different air-water discharge combinations and 231 data points

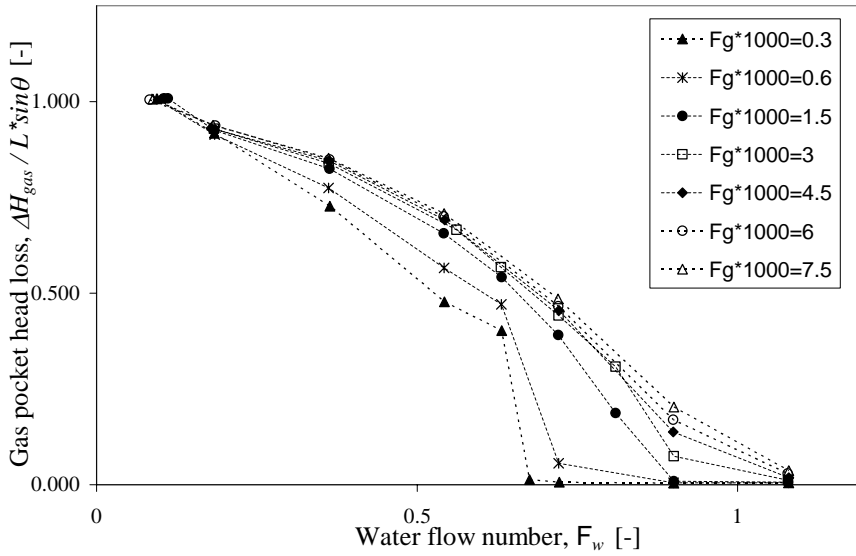


Figure B.12: Gas pocket head loss in facility 6 with  $\theta = 20^\circ$ ,  $D = 0.22$  m,  $L/D = 57$ , 55 different air-water discharge combinations and 241 data points

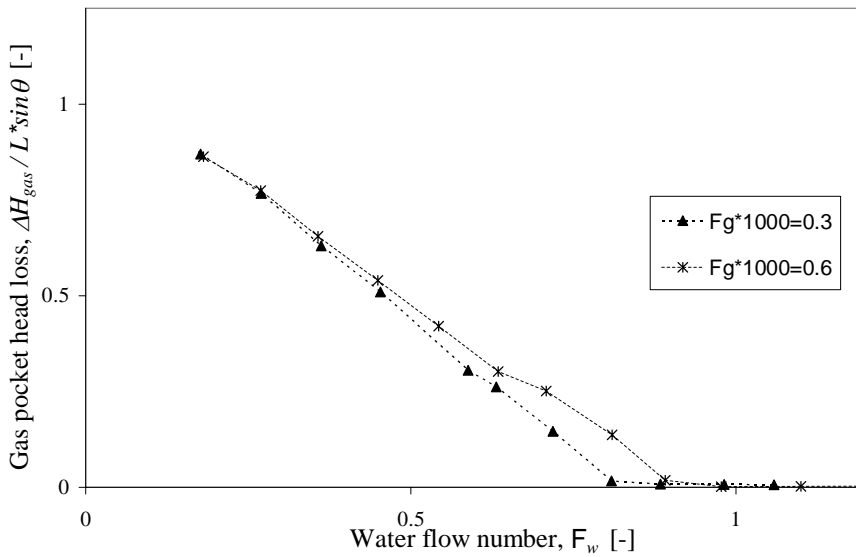


Figure B.13: Gas pocket head loss in facility 7 with  $\theta = 10^\circ$ ,  $D = 0.50$  m,  $L/D = 25$ , 23 different air-water discharge combinations and 72 data points



## Dankwoord

Ten eerste wil ik alle participanten danken voor hun bijdrage aan het CAPWAT project gedurende de afgelopen zes jaar. De participanten hebben niet alleen het project financieel mogelijk gemaakt, maar ook actief meegedacht in de sturing van het onderzoek. Bovendien hebben enkele participanten deelgenomen in de redactie van het nieuwe *Handboek voor hydraulisch ontwerp en beheer van afvalwaterpersleidingen*. Alle praktische consequenties, die voortvloeien uit dit onderzoek zijn hierdoor aangescherpt en beter verwoord. Een speciaal dankwoord gaat uit naar Peter Kamma van Hoogheemraadschap Brabantse Delta, die aan de wieg van het eerste CAPWAT onderzoeksproject heeft gestaan.

Mijn voorganger in het CAPWAT onderzoek Christof Lubbers heeft enorm veel meetdata in een groot aantal lab-opstellingen verzameld, waar ik dankbaar gebruik van kon maken voor de ontwikkeling van het rekenmodel. Gelukkig hebben de metingen aan het ruwe afvalwater de labmetingen nog waardevoller gemaakt. Michiel Tukker en Kees Kooij wil ik bedanken voor de perfecte samenwerking. Kees, je houdt iedereen inhoudelijk op scherp en had alle organisatorische zaken rond de handboek-redactie, de vergaderingen en het seminar weer prima geregeld.

Uiteraard wil ik mijn afdelingshoofd Ruud Lemmens en unit-manager Wiel Tilmans bedanken voor de kans die ze mij hebben gegeven om een promotie-onderzoek vrijwel geheel in werktijd te kunnen uitvoeren binnen het CAPWAT project. Het CAPWAT project mag dan, administratief gezien, een “gewoon” contract onderzoek zijn, ik beschouw het toch als een voorrecht om drie-en-een-half jaar lang een flink deel van mijn tijd vrijgesteld te zijn geweest van veel andere taken. Wiel en Ruud hebben mij alle vrijheid gegeven om prioriteit te leggen bij het CAPWAT onderzoek. Uiteraard bedank ik ook mijn directe collega's, vooral Ruud Lemmens, Anton Heinsbroek en Kees Kooij, die veel van mijn reguliere taken hebben overgenomen.

Mijn promotor Francois Clemens heeft mij vooral geïnspireerd met zijn onorthodoxe mening en onafhankelijke houding ten aanzien van de wereld. Het belang en de meerwaarde van metingen zijn ook in dit onderzoek weer duidelijk aangetoond. Marie-Claire, Jozanneke en Remy, bedankt voor de nuttige en leuke gesprekken over de rioleringswereld en vakantiebestemmingen.

Wim van Bergen Bravenboer en Aad de Brabander van RWZI Nieuwe Waterweg in Hoek van Holland wil ik bedanken voor alle medewerking die we hebben gekregen voor de

---

tijdelijke opstelling op de zuivering. Ook dank ik mijn collega's Wim Taal, Frans de Vreede en Theo Ammerlaan voor hun ondersteuning bij de instrumentatie in deze opstelling.

Dit proefschrift had niet in drie-en-een-half jaar geschreven kunnen worden zonder de inzet van vijf goede en enthousiaste stagiaires en afstudeerders. Marcel Kranendonk heeft metingen verricht aan een prototype pompkelder, waar hele concrete aanbevelingen uit zijn voortgekomen, die volop in de praktijk worden gebruikt. Michiel Tukker heeft water-lucht-metingen verricht aan twee kleinere opstellingen, waardoor de schaal-effecten gekwantificeerd konden worden; dat heeft hij zo goed gedaan dat hij mocht blijven. Bram Stegeman heeft zich uitgeleefd in de opstelling in Hoek van Holland en een perfecte, goed gedocumenteerde dataset opgeleverd; je moet soms drie uur in het zonnetje wachten totdat de meting stabiel is, maar dan heb je ook wat. Tonny Schuit heeft de nodige chemische kennis en ervaring in Hoek van Holland ingezet om de metingen met toegevoegde zepen en ruw afvalwater tot een succes te maken. Hij heeft bovendien een bijdrage geleverd aan ons cursusmateriaal over implosie en vervorming van PVC leidingen. Mitja Huttunen heeft vergelijkbare metingen uitgevoerd als Bram Stegeman, maar dan met ruw afvalwater en in oktober bij buitentemperaturen rond de 10 graden; maar goed, een echte Fin kan daar wel tegen. Allen bedankt voor het goede werk en de inzet. De aandachtige lezer krijgt wellicht de indruk dat de auteur van dit proefschrift zelf helemaal geen metingen heeft verricht, maar de auteur heeft ook de nodige keren, ook bij mindere weersomstandigheden, metingen uitgevoerd en afwijkende acties uitgevoerd (vullen, ledigen, "site-acceptance-test").

Tenslotte is het gebruikelijk om vrouw en kinderen te bedanken in dit dankwoord. Vaak valt daar een ondertoon uit af te leiden dat het afronden van het proefschrift niet altijd even makkelijk is gegaan. Dat is in dit geval erg meegevallen. Ellen en de kinderen hebben mij voortdurend herinnerd aan alle leuke gezamenlijke en minder leuke huishoudelijke activiteiten, zodat ik niet weg kon zakken in het mentale moeras van de onderzoeksdetails met al haar doodlopende paden. Ellen, vooral bedankt voor jouw steun en scherpte om zakelijk en privé zoveel mogelijk gescheiden te houden.

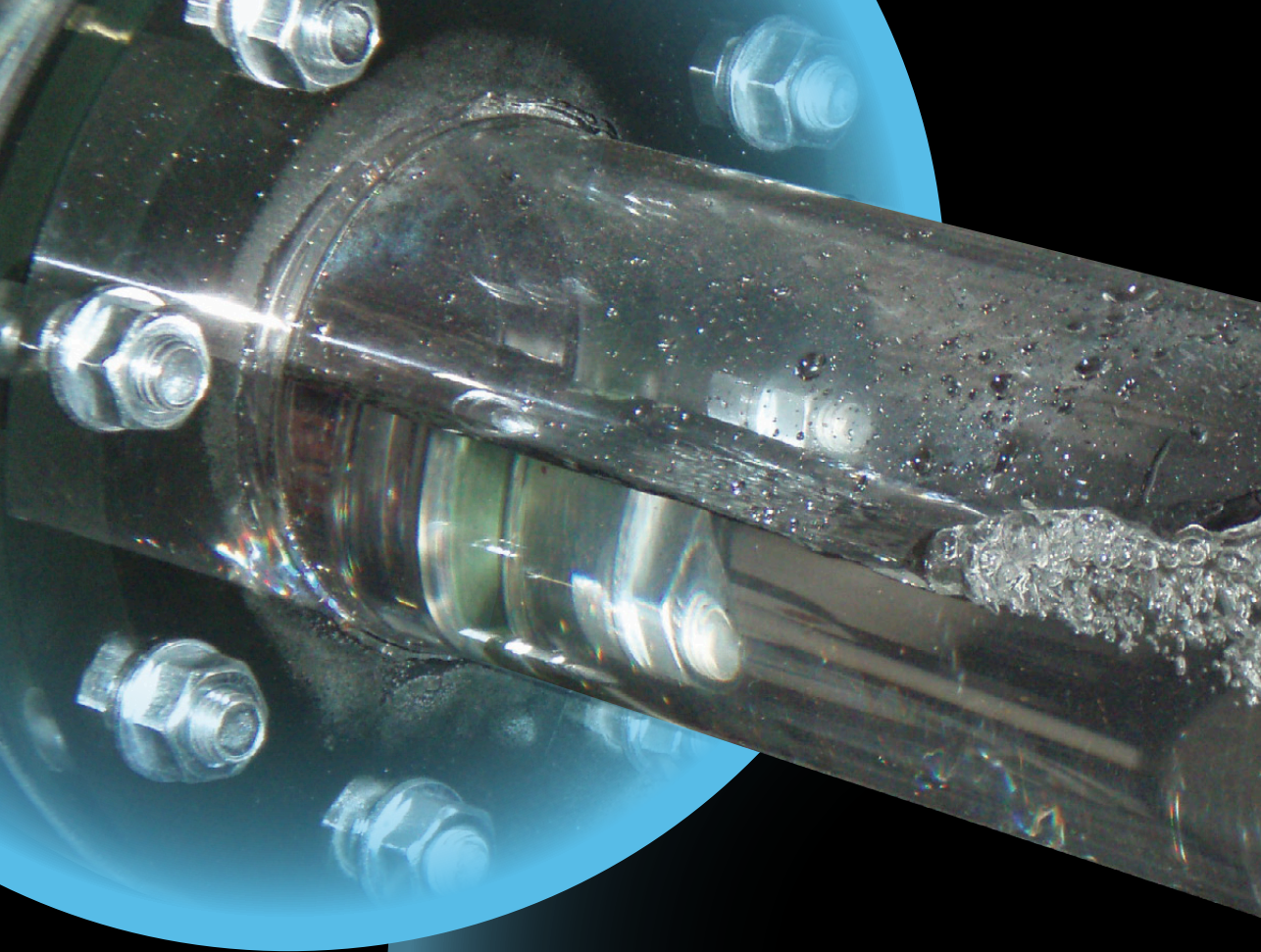
## Curriculum Vitae

Ivo Pothof was born on May 21<sup>st</sup> 1972 in Rhenen, Netherlands. He followed his secondary education at the Corderius College in Amersfoort (1984 – 1985) and at the R.K.S.G. Marianum in Groenlo (1985 – 1990), where he received his VWO diploma. Ivo Pothof studied Applied Mathematics at Twente University (1990 – 1995). His mathematical specialisation is Systems and Control Theory and the application courses focus on fluid dynamics, heat transfer and environmental flow modelling. Ivo Pothof completed a minor on Safety and Environmental Risk. He graduated on optimal positioning of pressure sensors in a drinking water distribution network and won the KIVI-NIRIA award for best MSc-thesis on Systems and Control Technology in 1995.

Ivo Pothof started his professional career at Infram in 1995, where he developed decision support models for integrated regional developments and for long-term maintenance planning of hydraulic structures owned by Rijkswaterstaat. He joined the Industrial Flow Technology department of WL | Delft Hydraulics in 1997. WL | Delft Hydraulics merged into Deltares in 2009. Ivo Pothof has specialized on fluid transients and optimal control of pipeline systems. He has worked on innovative solutions for the water industry in the Netherlands and abroad, like the application of booster pumping stations in the urban drainage system of Amsterdam. He has experience with development of numerical algorithms for fluid transients (WANDA software), commissioning fire fighting systems, transient field measurements, troubleshooting and training courses on fluid dynamics in pipeline systems. He has written guidelines on fluid transients in Dutch standard NEN 3650 – 2006: *Requirements for pipeline systems*. Ivo Pothof was project leader of the CAPWAT research project on capacity losses in pressurised wastewater mains since 2007 and conducted this PhD project as part of the CAPWAT research project at Deltares in close co-operation with Delft University of Technology. He co-authored the new *Handbook for hydraulic design and operation of pressurised wastewater mains* (2010, in Dutch), which was one of the main objectives of the CAPWAT research project. Currently, Ivo Pothof is responsible for Deltares' strategic research on sustainable energy and energy-efficiency.

Mr. Pothof is a member of Dutch professional unions *Waternetwerk*, *Warmtenetwerk* (Thermal Energy association) and the *International Association for Hydro-Environment Engineering and Research* (IAHR). He is a member of the Technical Committee of the Pressure Surges Conference Series since 2004 and affiliated with Delft University of Technology, department of Sanitary Engineering. He has published three peer-reviewed journal papers and numerous conference papers.





The photographs on the cover show air-entraining hydraulic jumps at four different scales in pipes with an internal diameter of 50 mm, 80 mm, 150 mm and 220 mm.